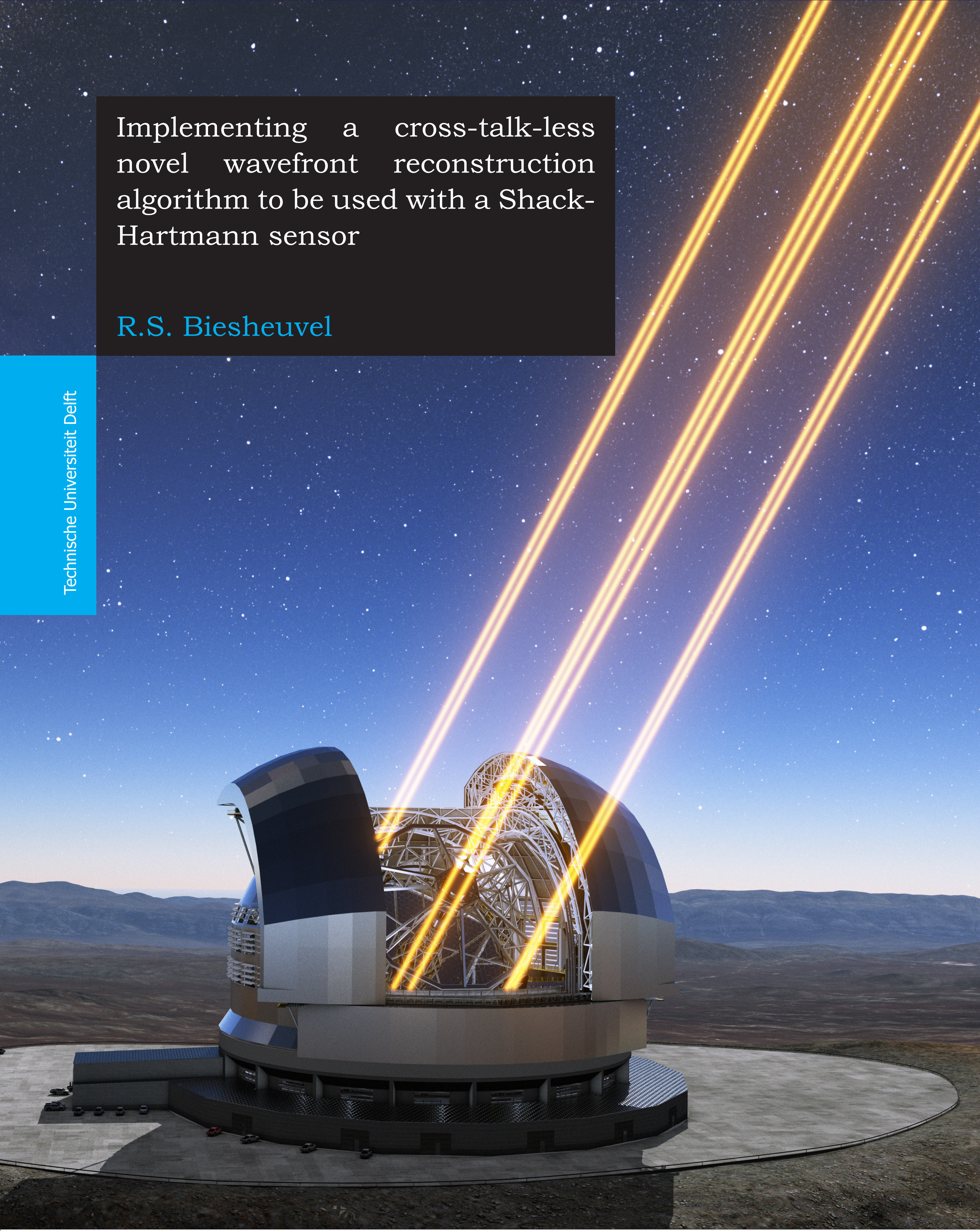

Implementing a cross-talk-less novel wavefront reconstruction algorithm to be used with a Shack-Hartmann sensor

R.S. Biesheuvel

Technische Universiteit Delft

Delft University of Technology

Challenge the future

Front cover:
Artist's impression of the European Extremely Large Telescope
Credit: ESO/L. Calçada,
used under Creative Commons Attribution 4.0 Unported License

Implementing a cross-talk-less novel wavefront reconstruction algorithm to be used with a Shack-Hartmann sensor

by

R. S. Biesheuvel

in partial fulfillment of the requirements for the degree of

Master of Science
in Applied Physics

at the Delft University of Technology,
to be defended publicly on Thursday December 7, 2017 at 15:30.

Thesis committee:	Dr. S.F. Pereira (Supervisor),	TU Delft, Optics (AS)
	Dr. P. Pozzi (Daily Supervisor),	TU Delft, DCSC (3mE)
	Prof. dr. G. Vdovin,	TU Delft, DCSC (3mE)
	Prof. dr. ir. M. Verhaegen,	TU Delft, DCSC (3mE)

An electronic version of this thesis is available at
`https://repository.tudelft.nl/`

Dedicated to my parents,
for their unyielding support

Abstract

For wavefront reconstruction, often the combination of a Shack-Hartmann sensor and a reconstruction method utilizing the Cartesian derivatives of Zernike polynomials (the least-squares method) is used, which is known to introduce cross-talk. In Janssen (2014) a new wavefront reconstruction algorithm is introduced to be used with the Shack-Hartmann sensor that does not present cross-talk. To our knowledge, this method has never been demonstrated. In the current research, Janssen's method and the conventional least-squares method are compared on a modified Michelson interferometer setup with a spatial light modulator to first remove the aberrations of the complete system, and subsequently introduce specific aberrations for which the Zernike coefficients are reconstructed using both reconstruction methods.

It is found that both methods work equally well with optimal fitting powers. When fitting fewer than the optimal amount of fitting powers, it was found that Janssen's method accurately recovered Zernike coefficient a_n^m when $n + 1$ powers are fit, while the conventional method achieves the same accuracy only at $n + 2$ fitting powers, especially when aberrations introducing cross-talk are present. When more than the optimal amount Zernike powers are used, it is seen that Janssen's method presents aliasing at lower fitting powers. At the optimal fitting power, the RMS landscape for both methods is shown to be similar, and therefore they are equally susceptible to errors due to mis-estimation of the center position and radius of the beam on the Shack-Hartmann sensor. Lastly, it is shown that theoretically, Janssen's method is at least 3.5 times slower than the conventional least-squares method due to the use of complex valued Zernike polynomials.

Contents

1 Introduction

When looking at the stars with a telescope, Newton noted that the image of the stars was quivering. These tremors made it very difficult to accurately measure the position of the stars, and made it more difficult to look at them in general. What he discovered was that the wavefront of the light of the star traveling through the atmosphere gets aberrated, and the image that is formed is degraded.

The biggest telescopes on earth around the world now contain active elements to counteract these tremors caused by the atmosphere. These active elements need an input on the conditions of air, not necessarily in terms of weather, but in which way it distorts the wavefront. Once this information is known, the tremors can be reduced using active elements.

To measure the distortion of the wavefront, often a Shack-Hartmann sensor is used. This sensor is not only used in telescopes, but also in microscopes and in metrology instruments. Using the sensor, the wavefront shape can be measured, and it is usually expressed using coefficients of a polynomial basis.

In most practical applications, when a Shack-Hartmann sensor is used to reconstruct the wavefront in coefficient of a polynomial basis, the least-squares method is used. An often-used polynomial basis are the Zernike polynomials. However, already since the 1980s it is known that there is a fundamental flaw in the combination of the least-squares method and Zernike polynomials. The fact is that the method presents cross-talk of coefficients, meaning that different coefficients are measured than the ones that are present.

To solve this, in 2014 Janssen introduced an algorithm that uses a different relation between the data of the Shack-Hartmann sensor and the final measured coefficients(Janssen, 2014). This relation theoretically solves the cross-coupling problem that is present in the least-squares method. Up to now, only the mathematical framework for the reconstruction method has been formulated, and there have been no reported implementations yet.

This research is aimed at implementing Janssens method and comparing it experimentally to the commonly used least-squares method. The two reconstruction methods are compared on five aspects.

First, the accuracy in optimal conditions are compared between the two methods. Secondly, the accuracy under conditions where cross-talk could occur is tested in order to verify that in Janssens method cross-talk is not present. This occurs when too little information is extracted from the Shack-Hartmann sensor. Afterwards, the effect on both algorithms is studied when too much information is extracted from the sensor, and the aliasing effect occurs. Furthermore, the effect of change of input parameters on the accuracy of reconstruction is researched. Lastly, the theoretical computational cost of both algorithms is compared.

In order to compare the two methods, the necessary theory is introduced in Section 2. In Section 3, the experimental setup is explained. How the experimental setup has been used is described in Section 4. The actual measurements are presented and discussed in Section 5, and the conclusions from these measurements are presented in Section 6. Lastly, Section 7 gives an outlook on cases that can be considered further to go give a better view on which wavefront reconstruction algorithm would be the most suitable one in specific use-cases.

2 Theory

The comparison between the different wavefront reconstruction techniques is based upon the theory discussed in this Section. Firstly, Zernike polynomials are discussed and used as a basis to describe the wavefronts. Afterwards, the workings of the Shack-Hartmann sensor are discussed. After this, the working principles of both the least-squares and Janssen's algorithm are discussed, as well as the differences between them. Last but not least, it is presented where these differences can manifest themselves most prominently.

2.1 Zernike polynomials can be used to describe aberrations in the wavefront

In systems where aberrations are desired to be known, such as microscopes and telescopes, usually a circular aperture is present. In order to describe these aberrations, circular polynomials are a powerful tool. Zernike polynomials are such a set of circular polynomials. In the case of aberration testing, Zernike polynomials are useful because the polynomials directly relate to aberrations that are often measured in these systems. This way, the coefficients of these polynomials can directly say something about the size and influence on the optical systems (Goodwin and Wyant, 2006). A table with polynomials and their contributions to the classical Seidel aberrations is shown in Table 2.1. The single number ordering presented in Table 2.1 is explained in Section 2.1.2.

Table 2.1: The first three powers of Zernike polynomials Z_n^m, their corresponding single Zernike number (explained in Section 2.1.2) and their relation to common Seidel aberrations

(n, m)	j	Contributions to the Seidel aberrations
Z_0^0	Z_1	piston
Z_1^{-1}	Z_2	y-tilt
Z_1^1	Z_3	x-tilt
Z_2^{-2}	Z_4	astigmatism 45°, defocus
Z_2^0	Z_5	defocus, piston
Z_2^2	Z_6	astigmatism 0°, defocus
Z_3^{-3}	Z_7	trefoil
Z_3^{-1}	Z_8	coma, y-tilt
Z_3^1	Z_9	coma, x-tilt
Z_3^3	Z_{10}	trefoil

This subsection will discuss what Zernike polynomials are, how they can more easily be used in computations and how the presence of aberrations will degrade the image quality.

2.1.1 Zernike polynomials form an orthogonal set on the unit disc

In this research, the American National Standards Institute (ANSI) definition for Zernike polynomials is used. As defined in Thibos et al. (2002), the polynomial is defined in polar coordinates (ρ, θ) as

$$Z_n^m(\rho,\theta) = N_n^m R_n^{|m|}(\rho)\Theta_m(\theta), \tag{2.1}$$

where

$$N_n^m = \sqrt{(2-\delta_{m0})(n+1)} \tag{2.2}$$

$$R_n^{|m|}(\rho) = \sum_{s=0}^{\frac{n-|m|}{2}} \frac{(-1)^s(n-s)!}{s!\left(\frac{n-|m|}{2}-s\right)!\left(\frac{n+|m|}{2}-s\right)!}\rho^{n-2s} \tag{2.3}$$

$$\Theta_m(\theta) = \begin{cases} \cos(m\theta), & \text{if } m \geq 0 \\ -\sin(m\theta), & \text{if } m < 0, \end{cases} \tag{2.4}$$

such that $Z_n^m(\rho,\theta)$ is a real valued, orthonormal (on the unit disc) expression for Zernike polynomials. In these expressions, n is the power of the Zernike polynomial, and m the azimuthal order, which are subject to

$$n \geq 0, \tag{2.5}$$

$$n - |m| \text{ is even}, \tag{2.6}$$

$$|m| \leq n, \tag{2.7}$$

and $\rho \leq 1$ the radius on the unit disc, and $\delta_{nn'}$ the Krönecker delta function.

As mentioned above, these polynomials are orthonormal on the unit disc. In formula, this implies

$$\int_0^1 \int_0^{2\pi} Z_n^m(\rho,\theta) Z_{n'}^{m'}(\rho,\theta)\rho \mathrm{d}\theta \mathrm{d}\rho = \pi\delta_{nn'}\delta_{mm'}. \tag{2.8}$$

With this definition, any real-valued wavefront function (defined on the unit disc) can be described as a linear combination of the Zernike polynomials given by

$$W(\rho,\theta) = \sum_{m=-\infty}^{\infty} \sum_{n\in\eta_m} a_n^m Z_n^m(\rho,\theta), \tag{2.9}$$

where η_m is the set of allowed n values dependent on m, namely $\eta_m = \{|m|, |m|+2, |m|+4, \ldots, \infty\}$ when $m \neq 0$, and $\eta_m = \{2, 4, \ldots, \infty\}$ when

$m = 0$. This set ensures that the constraints set in Equations 2.5, 2.6, 2.7 are all met. Here a_n^m is the real-valued Zernike coefficient.

Although there is an international standard set by the American National Standards Institute (ANSI) for the definition of Zernike polynomials, many researchers use their own definition to fit the needs of their research. For instance, Navarro et al. (2011) and Janssen (2014) use complex valued Zernike polynomials, where Navarro et al. adds a normalization factor to make the basis orthonormal. Stephenson (2014) and van Brug (1997) use a definition of real-valued Zernike polynomials, where Stephenson uses the ANSI standard, while van Brug uses a different definition for the azimuthal order m.

Because Janssen's algorithm is used in this research, this paragraph will discuss the conversion between bases and their coefficients. The complex valued Zernike polynomial is defined in polar coordinates (ρ, θ) on the unit disc as

$$C_n^m(\rho, \theta) = R_n^{|m|}(\rho) e^{im\theta}, \tag{2.10}$$

where C_n^m is used to emphasize that the polynomial is complex. The radial polynomial $R_n^{|m|}$ is given as

$$R_n^{|m|}(\rho) = \rho^{|m|} P_{\frac{n-|m|}{2}}^{(0,|m|)}(2\rho^2 - 1), \tag{2.11}$$

with $P_k^{(\alpha,\beta)}(x)$ the Jacobi polynomial of degree k, which is orthogonal with respect to the weight $(1-x)^\alpha(1+x)^\beta$ on the interval$[-1, 1]$. Note that the factor $\rho^{|m|}$ is missing in Janssen (2014), but can be found in Janssen (2010). This definition of the radial component $R_n^{|m|}(\rho)$ and the definition of Equation 2.3 are the same. The value of $C_n^m = 0$ for all values of n and m where $n - |m|$ are odd or negative. This leads to a normalization condition of

$$\int_0^1 \int_0^{2\pi} C_n^m(\rho, \theta) \left(C_{n'}^{m'}(\rho, \theta) \right)^* \rho \mathrm{d}\theta \mathrm{d}\rho = \frac{\pi}{n+1} \delta_{nn'} \delta_{mm'}. \tag{2.12}$$

This orthogonality means that, like the real valued Zernike polynomial, any sufficiently smooth (complex) wavefront can be described by

$$W(\rho, \theta) = \sum_{m=-\infty}^{\infty} \sum_{n \in \eta_m} \alpha_n^m C_n^m(\rho, \theta), \tag{2.13}$$

where α_n^m are generally complex valued coefficients corresponding to the complex Zernike polynomial. Expanding the complex exponential in Equation 2.10 leads to the following conversion between this definition of complex

Zernike polynomials and the ANSI standard

$$N_n^m C_n^m(\rho,\theta) = \begin{cases} Z_n^{|m|}(\rho,\theta) + iZ_n^{-|m|}(\rho,\theta), & \text{if } m > 0 \\ Z_n^{|m|}(\rho,\theta) - iZ_n^{-|m|}(\rho,\theta), & \text{if } m < 0 \\ Z_n^m, & \text{if } m = 0, \end{cases} \tag{2.14}$$

where N_n^m is defined in Equation 2.2

From the definition of the complex Zernike polynomial in Equation 2.10 we can also see that the complex conjugate $\left(C_n^{|m|}\right)^*$ must be equal to $C_n^{-|m|}$. This observation, together with the relations between the real and complex Zernike polynomials leads to the expression

$$Z_n^m = \begin{cases} \dfrac{N_n^m}{2}\left(C_n^{|m|} + C_n^{-|m|}\right) = N_n^m \mathrm{Re}\left(C_n^{|m|}\right), & \text{if } m > 0 \\ \dfrac{N_n^m}{2i}\left(C_n^{|m|} - C_n^{-|m|}\right) = N_n^m \mathrm{Im}\left(C_n^{|m|}\right), & \text{if } m < 0 \\ N_n^m C_n^{|m|}, & \text{if } m = 0. \end{cases} \tag{2.15}$$

When using complex polynomials to describe a real wavefront, the coefficients are usually complex valued. In order to transform them back to the coefficients of the real-valued Zernike Z_n^m, the following relations (derived in Appendix A) can be used

$$a_n^m = \begin{cases} \dfrac{1}{N_n^m}\mathrm{Re}\left(\alpha_n^{|m|} + \alpha_n^{-|m|}\right), & \text{if } m > 0 \\ \dfrac{-1}{N_n^m}\mathrm{Im}\left(\alpha_n^{|m|} - \alpha_n^{-|m|}\right), & \text{if } m < 0 \\ \dfrac{1}{N_n^m}\mathrm{Re}\left(\alpha_n^m\right), & \text{if } m = 0. \end{cases} \tag{2.16}$$

2.1.2 Single numbering is introduced to help with computing

In this research, the Zernike polynomials are evaluated on the computer, and data is saved in vectors and matrices. To make it easy to loop over all polynomials, a single index is introduced. In the notation by Thibos et al. (2002), this single index j starts at 1 and monotonically increases, and is given by

$$j = \frac{n(n+2)+m}{2}, \tag{2.17}$$

where n is the Zernike power and m the azimuthal order. The reverse can also be done, that is finding n and m from j as follows

$$n = \left\lceil \frac{-3+\sqrt{9+8j}}{2} \right\rceil, \tag{2.18}$$

$$m = 2j - n(n+2), \tag{2.19}$$

where $\lceil x \rceil$ denotes the "ceiling" function, that is the smallest integer greater than x.

The first 3 powers of Zernike polynomials are written out in Table 2.1 to show that the azimuthal order m starts low and linearly increases per power. Note that this is different from Noll's ordering and Fringe ordering, which are other frequently used ordering schemes.

2.1.3 Aberrations are spatial changes in phase over ideal wavefront and cause deterioration in image quality

When looking at a perfect imaging system, one can say that the presence of a point-source object yields a perfect spherical wave at the exit pupil, converging to the ideal geometrical imaging point (Goodman, 2005). When this is the case, the system is diffraction limited. An aberration is when the wave at the exit pupil deviates from spherical. These aberrations can be caused by many sources. Examples of the sources of aberrations include turbulence in the air when looking at the stars and imperfections of the lenses used in the system.

The effect of aberrations on the image quality can be conveyed with a small example. If a plane wave $P_{in}(x, y)$ hits a lens with focal length f, the electric field $P_{out}(x, y)$ behind the lens can be determined as

$$P_{out}(x, y) = P_{in}(x, y)e^{\frac{-\pi i(x^2+y^2)}{\lambda f}}, \tag{2.20}$$

where λ is the wavelength of the plane wave. If P_{in} is perfectly flat, the outgoing wave will be a perfect spherical wave with the size of the aperture. If the incoming wave has an aberration, or if the lens is not perfectly spherical in shape, the general wavefront after the lens can be described as

$$\mathcal{P}(x, y) = P_{out}(x, y)e^{\frac{2\pi i W(x,y)}{\lambda}}. \tag{2.21}$$

Here, $\frac{2\pi W(x,y)}{\lambda}$ is the total added phase, where $W(x, y)$ is the aberration.

From Fourier optics it is known that the electric field intensity in the focal spot can be described as

$$|U_{focal}(x, y, f)|^2 = \frac{1}{\lambda^2 f^2} \left| \mathcal{F}\left\{ \mathcal{P}e^{\frac{\pi i(x^2+y^2)}{\lambda f}} \right\} \left(\frac{x}{\lambda f}, \frac{y}{\lambda f} \right) \right|^2, \tag{2.22}$$

where $\mathcal{F}\{y\}(x)$ denotes the Fourier transform of y evaluated at x. If P_{in} is a flat wavefront cut off by the aperture, $\mathcal{P}$ can be seen as the aperture with within a phase plate. This added phase will always cause a deterioration of the focal spot quality (Goodman, 2005). Because of this, minimizing aberrations will improve image quality obtained by the system. An example is shown in Figure 2.1.

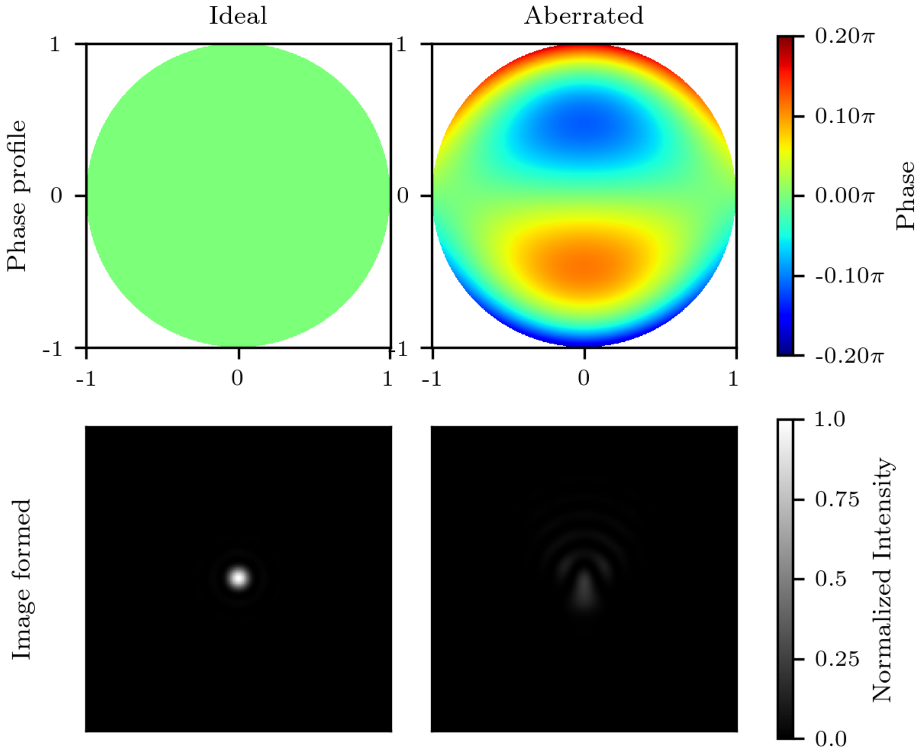

Figure 2.1: The effect of Z_3^{-1} coma on the created image. The top row shows the wavefront before hitting the lens, and the bottom row shows the image formed by this wavefront. Images are formed with the same amplitude plane-wave, so the total power is constant. It can be seen that the shape and the amplitude of the peak intensity are altered when the aberration is present.

2.2 Shack-Hartmann sensors are built such that the local slope of the wavefront can be measured

From the previous section, it is apparent that aberrations in an optical system degrade the quality of the image gathered. In the field of adaptive optics, research is being done on how to cancel these aberrations. One way of achieving this is by measuring the phase aberration φ_W, and by altering an active optical component in such a way that this aberration is canceled out. An example of this can be seen in the European Extremely Large Telescope being built right now. In this telescope, there is an adaptive mirror with a diameter of 2.4 meters consisting of over 8000 actuators which can compensate real time for aberrations due to turbulence and shaking of the optical components due to the wind (European Southern Observatory, 2011).

In order for this compensation to work well, the phase aberration φ_W has to be measured accurately. A typical way of measuring this in an adaptive optics set-up is by using a Shack-Hartmann sensor. A Shack-Hartmann sensor consists of a camera chip and lenslet array. A typical setup and working diagram can be seen in Figure 2.2. The lenslets are placed at the focal distance from the camera chip such that an incoming plane wave will be focussed as many spots on the camera. A plane wave is shown on the left in red. If the incoming wave is aberrated, the spot position will be changed. On the right, one can see the displacements of the spots due to a spherical wave aberration.

In this section, first the amount of displacement due to the aberrations will be derived, and afterwards two algorithms for retrieving the phase due to these displacements will be introduced.

2.2.1 Spot displacement on the sensor is proportional to the average slope of the phase over the lenslet

It can be derived from the theory how much a spot is displaced due to an aberration. Because this displacement is linear, the reverse problem can be solved as well. In other words, one can retrieve the aberration given the spot displacement.

In order to derive this displacement, one important assumption has to be done, namely that the slope of the phase over the lenslet can be approximated with a first order approximation. That is, the slope of the phase does not vary much over the area of the lenslet. This is an important assumption that will come back when determining which aberrations can be resolved.

If the variation of the slope over the lenslet is small enough, we can approximate the slope as

$$\varphi_W = x \left.\frac{\partial \varphi}{\partial x}\right|_{\mathbf{x}_0} + y \left.\frac{\partial \varphi}{\partial y}\right|_{\mathbf{x}_0}, \tag{2.23}$$

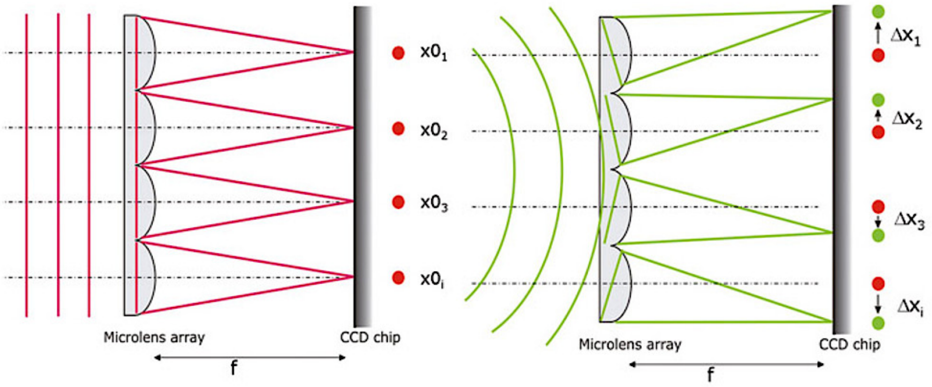

Figure 2.2: Schematic working of a Shack-Hartmann sensor. Adapted from Trioptics (2017).

where $\mathbf{x}_0$ is the center position of the lenslet. Substituting this phase φ_W into 2.21, the wavefront just after one lenslet can be determined as

$$\mathcal{P}(x,y) = P_{in}(x,y)e^{\frac{-\pi i(x^2+y^2)}{\lambda f}} e^{i\left(x\frac{\partial\varphi}{\partial x}\big|_{\mathbf{x}_0} + y\frac{\partial\varphi}{\partial y}\big|_{\mathbf{x}_0}\right)}. \tag{2.24}$$

Using this phase in the expression for the intensity in focus of Equation 2.22, the shape of the spot can be determined by evaluating the Fourier transform of this wavefront. Again, P_{in} can be assumed to be a flat wavefront in the shape of the aperture. Using a circular aperture of radius R, the Fourier transform to be evaluated is

$$\mathcal{F}\left\{\mathcal{P}\right\} = \mathcal{F}\left\{\operatorname{circ}\left(\frac{\sqrt{x^2+y^2}}{R}\right) \cdot e^{i\left(x\frac{\partial\varphi}{\partial x}\big|_{\mathbf{x}_0} + y\frac{\partial\varphi}{\partial y}\big|_{\mathbf{x}_0}\right)}\right\}, \tag{2.25}$$

where circ is defined as

$$\operatorname{circ}(r) = \begin{cases} 1 & r \leq 1 \\ 0 & \text{otherwise} \end{cases}. \tag{2.26}$$

Using the convolution theorem, one can see that that the spot becomes a convolution of the Airy disc (from the circular aperture), and the two delta peaks $\delta\left(x - \frac{1}{2\pi}\frac{\partial\varphi}{\partial x}\Big|_{\mathbf{x}_0}\right)\delta\left(y - \frac{1}{2\pi}\frac{\partial\varphi}{\partial y}\Big|_{\mathbf{x}_0}\right)$. This convolution is nothing more than evaluating the original function at a different place. Substituting this knowledge back in Equation 2.22, the final expression for the intensity in the focal field becomes

$$|U_{focal}(x,y,f)|^2 = \frac{1}{\lambda^2 f^2}\left|\mathcal{F}\left\{\operatorname{circ}\left(\frac{\sqrt{x^2+y^2}}{R}\right)\right\}\left(\frac{x}{\lambda f} - \frac{1}{2\pi}\frac{\partial\varphi}{\partial x}\bigg|_{\mathbf{x}_0}, \frac{y}{\lambda f} - \frac{1}{2\pi}\frac{\partial\varphi}{\partial y}\bigg|_{\mathbf{x}_0}\right)\right|^2. \tag{2.27}$$

This means that the shift in the peak intensity scales linearly with the slope of the phase over the lenslet. The shift in x- and y-position of the spots, denoted as Δx and Δy, on the camera chip can be expressed as

$$\begin{cases} \Delta x &= \dfrac{\lambda f}{2\pi} \left.\dfrac{\partial \varphi}{\partial x}\right|_{\mathbf{x}_0} \\ \Delta y &= \dfrac{\lambda f}{2\pi} \left.\dfrac{\partial \varphi}{\partial y}\right|_{\mathbf{x}_0} \end{cases}. \tag{2.28}$$

It is useful to define the aberration W on the unit disc, due to the fact that the Zernike polynomials are orthogonal there. If r is the radius of the beam incoming on the Shack-Hartmann sensor, the slopes of the aberration can be expressed as

$$\begin{cases} \left.\dfrac{\partial W}{\partial x}\right|_{\mathbf{x}_0} &= r\dfrac{\Delta x}{f} \\ \left.\dfrac{\partial W}{\partial y}\right|_{\mathbf{x}_0} &= r\dfrac{\Delta y}{f} \end{cases} \tag{2.29}$$

for a wavefront with constant slope. Dai (2008) has proven that for a varying wavefront over the subaperture, the slope needs to be averaged over that subaperture. The expressions for the average slopes in terms of displacement of the spot on the camera chip becomes

$$\begin{cases} \dfrac{1}{A_\Sigma}\displaystyle\int_\Sigma \dfrac{\partial W}{\partial x}\mathrm{d}x\mathrm{d}y &= r\dfrac{\Delta x}{f} \\ \dfrac{1}{A_\Sigma}\displaystyle\int_\Sigma \dfrac{\partial W}{\partial y}\mathrm{d}x\mathrm{d}y &= r\dfrac{\Delta y}{f} \end{cases} \tag{2.30}$$

where Σ is the illuminated sub-aperture domain, with surface area A_Σ. Here Σ changes when the sub-aperture is only partially illuminated (i.e. at the edge of the beam), and therefore A_Σ does as well. This averaging of the slope is important in recovering the wavefront, as explained in the following sections. Figure 2.3 shows an example Shack-Hartmann spot pattern, with two different illuminated areas A_Σ. In the Figure, $A_{\Sigma 1}$ shows a spot fully within the illuminated area, while $A_{\Sigma 2}$ shows a spot close to the edge of the illuminated area.

2.2.2 A conventional least-squares method fits the local derivatives of Zernike polynomials to gather the coefficients

The least-squares (LSQ) fit is based on the real Zernike polynomials, and uses the fact that the coefficients are not dependent on x and y. The wavefront in x, y coordinates (with $\sqrt{x^2 + y^2} \leq 1$) can be described as

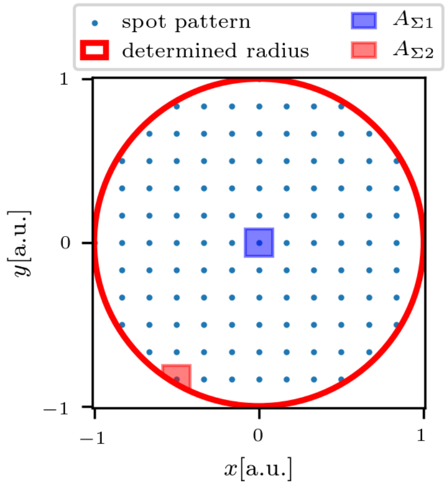

Figure 2.3: Sample Shack-Hartmann pattern with two different sub-aperture sizes. Blue shows the surface area when the spot is not close to the border, while the red area is taken when the spot is close to the edge of the illuminated area.

$$W(x,y) = \sum_{m=-\infty}^{\infty} \sum_{n \in \eta_m} a_n^m Z_n^m(x,y). \tag{2.31}$$

The measured quantity, however, is not W but $\frac{\partial W}{\partial x}$ and $\frac{\partial W}{\partial y}$. Taking the partial derivatives to x and y results in the over determined system of

$$\begin{cases} \dfrac{\partial W}{\partial x} = \displaystyle\sum_{m=-\infty}^{\infty} \sum_{n \in \eta_m} a_n^m \frac{\partial Z_n^m}{\partial x} \\ \dfrac{\partial W}{\partial y} = \displaystyle\sum_{m=-\infty}^{\infty} \sum_{n \in \eta_m} a_n^m \frac{\partial Z_n^m}{\partial y}. \end{cases} \tag{2.32}$$

This system can be solved for finite length a_n^m. Using Equation 2.30, given the displacements Δx and Δy, one can create a vector $\mathbf{s}$ containing the slopes as such

$$\mathbf{s} = \begin{bmatrix} \left.\dfrac{\partial W}{\partial x}\right|_1 & \left.\dfrac{\partial W}{\partial x}\right|_2 & \cdots & \left.\dfrac{\partial W}{\partial x}\right|_{n_{\text{spots}}} & \left.\dfrac{\partial W}{\partial y}\right|_1 & \left.\dfrac{\partial W}{\partial y}\right|_2 & \cdots & \left.\dfrac{\partial W}{\partial y}\right|_{n_{\text{spots}}} \end{bmatrix}^T. \tag{2.33}$$

The partial derivatives of the Zernikes in the x- and y-direction can also be put in a matrix, called the geometry matrix. The geometry matrix G can be built up $\left.\frac{\overline{\partial Z_j}}{\partial x}\right|_n$, the average gradient of Zernike mode j at the position of spot n. This averaging is done due to the fact that the spot displacement measured with the Shack-Hartmann sensor is proportional to the average slope of the wavefront, as expressed in Equation 2.30. It should be noted that the positions over which the averaging is done is normalized to the unit disc. These windows are the same defined in 2.30 and 2.3. The matrix will have a size of $(2n_{\text{spot}} \times J)$, where J is the maximum index for the Zernike modes used to have a good approximation of the true wavefront. The expression for G becomes

$$G = \begin{bmatrix} \left.\frac{\overline{\partial Z_1}}{\partial x}\right|_1 & \left.\frac{\overline{\partial Z_1}}{\partial x}\right|_2 & \cdots & \left.\frac{\overline{\partial Z_1}}{\partial x}\right|_{n_{\text{spot}}} & \left.\frac{\overline{\partial Z_1}}{\partial y}\right|_1 & \left.\frac{\overline{\partial Z_1}}{\partial y}\right|_2 & \cdots & \left.\frac{\overline{\partial Z_1}}{\partial y}\right|_{n_{\text{spot}}} \\ \left.\frac{\overline{\partial Z_2}}{\partial x}\right|_1 & \left.\frac{\overline{\partial Z_2}}{\partial x}\right|_2 & \cdots & \left.\frac{\overline{\partial Z_2}}{\partial x}\right|_{n_{\text{spot}}} & \left.\frac{\overline{\partial Z_2}}{\partial y}\right|_1 & \left.\frac{\overline{\partial Z_2}}{\partial y}\right|_2 & \cdots & \left.\frac{\overline{\partial Z_2}}{\partial y}\right|_{n_{\text{spot}}} \\ \vdots & \vdots & \ddots & \vdots & \vdots & \vdots & \ddots & \vdots \\ \left.\frac{\overline{\partial Z_J}}{\partial x}\right|_1 & \left.\frac{\overline{\partial Z_J}}{\partial x}\right|_2 & \cdots & \left.\frac{\overline{\partial Z_J}}{\partial x}\right|_{n_{\text{spot}}} & \left.\frac{\overline{\partial Z_J}}{\partial y}\right|_1 & \left.\frac{\overline{\partial Z_J}}{\partial y}\right|_2 & \cdots & \left.\frac{\overline{\partial Z_J}}{\partial y}\right|_{n_{\text{spot}}} \end{bmatrix}^T . \tag{2.34}$$

The system of Equation 2.32 can then be written as

$$\mathbf{s} \approx G \cdot \mathbf{a}, \tag{2.35}$$

where $\mathbf{a}$ is the vector containing the Zernike coefficients. The least-squares estimation of a_n^m becomes

$$\mathbf{a} \approx G^+ \cdot \mathbf{s}, \tag{2.36}$$

where G^+ the generalized inverse of the geometry matrix. This is an approximation as G only contains the information of a finite number of Zernike modes, and their contribution is averaged over the lenslet array.

2.2.3 Janssen's method uses an analytical relation between the local derivatives of the wavefront and Zernike polynomials

Janssen's method relies on an analytical relation found between the local derivatives of the wavefront and Zernike polynomials. This is in contrast with the least-squares fit as described in the previous subsection, where there was a link between the local derivatives of the wavefront and the derivatives of the Zernike polynomials.

The reconstruction is based on the identities

$$\begin{aligned} \frac{\partial C_n^m}{\partial x} &= \frac{\partial C_{n-2}^m}{\partial x} + n\left(C_{n-1}^{m-1} + C_{n-1}^{m+1}\right) \\ \frac{\partial C_n^m}{\partial y} &= \frac{\partial C_{n-2}^m}{\partial y} + in\left(C_{n-1}^{m-1} + C_{n-1}^{m+1}\right), \end{aligned} \tag{2.37}$$

where these identities allow the expression of any derivative Zernike polynomial as a sum of Zernike polynomials. The conclusions of Janssen's work are described here in this section, and for the full derivation, one is encouraged to read Janssen (2014).

The wavefront for Janssen's method is described as

$$W(\rho,\theta) = \sum_{m=-\infty}^{\infty} \sum_{n\in\eta_m} \alpha_n^m C_n^m(\rho,\theta), \tag{2.38}$$

where $C_n^m(\rho,\theta)$ the complex Zernike polynomials, and α_n^m the complex Zernike coefficient. Janssen has found that the complex coefficients can be estimated as

$$\hat{\alpha}_n^m = c_n^m \varphi_n^m - c_{n+2}^m \varphi_{n+2}^m, \tag{2.39}$$

where

$$c_n^m = \frac{1+\delta_{n|m|}}{2n} \tag{2.40}$$

$$\varphi_n^m = \frac{1}{2}\left(\beta_+\right)_{n-1}^{m+1} + \frac{1}{2}\left(\beta_-\right)_{n-1}^{m-1}, \tag{2.41}$$

and where $\delta_{nn'}$ is the Kronecker delta equal to 1 if $n = n'$ and 0 otherwise. Furthermore β_+ and β_- are the least-squares solution to the problems

$$\frac{\partial W}{\partial x} \pm i\frac{\partial W}{\partial y} = \sum_{m=-\infty}^{\infty} \sum_{n\in\eta_m} \left(\beta_\pm\right)_n^m C_n^m. \tag{2.42}$$

Note that the desired coefficients α_n^m are analytically related to four β coefficients, namely $\left(\beta_+\right)_{n+1}^{m+1}$, $\left(\beta_+\right)_{n-1}^{m+1}$, $\left(\beta_-\right)_{n-1}^{m-1}$, and $\left(\beta_-\right)_{n+1}^{m-1}$. The fact that α_n^m is analytically related to β coefficients is desirable, because β-coefficients can directly be estimated (in a least-squares sense) from measurable quantities. This fit is made in the same way as the least-squares method. This means that also the complex Zernike polynomials need to be averaged over the lenslets. The fit to get the β coefficients, however, is done with a different basis than in the least-squares method to find the a-coefficients. The effects of this are discussed in the following section.

As a note for this method, when $n = |m|$, there will be non-existent combinations of n and m in Equation 2.41. In that case the value of β will be set to 0. For instance, $\hat{\alpha}_1^1$ is among others dependent on $(\beta_+)_0^2$, which goes against the constraint given in Equation 2.7.

To go from complex coefficient α_n^m to the real coefficent a_n^m, the relations in Equation 2.16 can be used. A good check to see if everything has gone right with indexing would be to check if the imaginary part of a_n^m is negligible compared to the real part, as the measured wavefront is real-valued.

2.2.4 The main difference between the methods is in the basis for fitting

The main difference between the least-squares method and Janssen's method for finding the coefficients is in how the fitting is done. Both methods use a least-squares fit using a geometry matrix, but the matrix elements are constructed differently. In the least-squares method, the geometry matrix elements are evaluations of the average gradient of the real valued Zernike polynomials over certain windows, while for Janssen's method it is the average of the complex valued Zernike polynomials over the same windows.

The gradients of the Zernike polynomials are known not to be orthogonal. This can cause problems called cross-talk when fitting the coefficients, especially when there are more aberrations present in the system than are being fit.

If $\mathbf{a}$ is an M dimensional vector containing the coefficients of the aberrations present in the system, the slopes on the Shack-Hartmann sensor can be determined as

$$\mathbf{s} = G\mathbf{a}, \tag{2.43}$$

where $\mathbf{s}$ is an $2n_{\text{spot}}$ long vector containing the x- and y-displacement on the Shack-Hartmann sensor and G an $2n_{\text{spot}} \times M$ geometry matrix as defined in Equation 2.34. Note that the first column contains the x- and y-derivatives of the first Zernike polynomial evaluated in all n_{spot} points. When a least-squares estimation of the coefficients $\hat{\mathbf{a}}$ (where the hat denotes that it is the estimated parameter) is made using less Zernike polynomials, up to Zernike polynomial $J < M$, cross-talk will occur. The estimator $\hat{\mathbf{a}}$ can be expressed as

$$\hat{\mathbf{a}} \approx G_l^{+}\mathbf{s} \tag{2.44}$$

$$\hat{\mathbf{a}} \approx G_l^{+}G\mathbf{a}, \tag{2.45}$$

where G_l is the geometry matrix containing the columns of the first J Zernike polynomials. The estimator will estimate the lower order values of the coefficients with influence of the higher values, because the matrix $G_l^{+}G$ will not be an identity matrix. A derivation of which Zernike modes influence which lower order ones can be found in Appendix D.

When estimating the coefficient $\hat{a}_n^m$, a higher order aberration $a_{n'}^{m'}$ will influence the estimation if it is not accounted for in G_l (i.e. the single index of $a_{n'}^{m'}$ $j > J$) and if

$$\{(n, m, n', m') \in \mathbb{Z} \mid n \in \eta_m,\ m = m' \text{ or } m = m' \pm 2,$$
$$n' > n,\ n \geq m' + 2,\ n' \in \eta_{m'},\ m' \neq 0\},$$

or if

$$\{(n, m, n', m') \in \mathbb{Z} \mid n \in \eta_m,\ m = m' \text{ or } m = m' + 2,$$
$$n' > n,\ n \geq 2,\ n' \in \eta_{m'},\ m' = 0\},$$

where in both cases η_m and $\eta_{m'}$ are the sets of allowed values for n and n' dependent on m and m' such that Equations 2.5, 2.6 and 2.7 are all met.

Because of this, it is expected that the least-squares method will wrongly estimate the coefficients if there are higher order aberrations present that are not accounted for in the geometry matrix G_l. For Janssen's method, the geometry matrix contains the Zernike polynomials themselves, and therefore it is not expected to present any cross-talk. This is experimentally verified and shown in Section 5.2. Also the accuracy when enough fitting powers are present, accuracy when fitting too many powers, the error landscape of both reconstruction method and the algorithm complexity is shown in the Results section. The experiments are described in the Experimental setup and Experimental method section.

3 Experimental setup

In order to compare Janssen's method and the least-squares method, the following experimental setup has been designed.

- A Michelson interferometer is used to gather the reference and the aberrated beam.
- Controlled aberrations are added using a spatial light modulator.
- Artifacts of using a reflective spatial light modulator are then removed using an iris.
- In order to visually inspect if aberrations are added correctly, a CCD camera is added to view the interference pattern generated by the interferometer.

This section discusses how the Michelson interferometer works, how it can be used to gather the necessary data for both Shack-Hartmann reconstruction methods and how it needs to be modified in order to remove the artifacts introduced by the reflective spatial light modulator.

3.1 A Michelson interferometer is used to gather the necessary information

The choice to build an interferometer was made due to the fact that the Shack-Hartmann camera needs a flat wavefront reference as well as the aberrated wavefront. The choice for the Michelson interferometer was made due to the availability of a reflective SLM, and the relatively simple nature of the setup. The following sections introduce the Michelson interferometer and how it can be used to make measurements using a Shack-Hartmann sensor.

3.1.1 Traditional Michelson interferometer makes an interference pattern between a reference arm and an aberrated arm

An interferogram is an image created by superimposing two wavefronts. This interferogram therefore contains information about the two wavefronts. A typical Michelson interferometer is shown in Figure 3.1. In this figure, the lenses f_1 and f_2 are used to expand and collimate the beam. This collimated beam is shone on an iris, which will block most of the light. If the iris is small compared to the size of the collimated laser beam, the light after the pinhole can be considered a as a plane wave with uniform intensity distribution. This beam is then split by the 50-50 beamsplitter and sent to the reference mirror and to the SLM. The SLM and the reference mirror are then imaged on an interferogram camera using a $4f$ telescopic system. This is done with the lenses f_3 and f_4. If the system is aligned well, the only difference in optical path comes from the phase modulation of the SLM.

At the interferometer camera, the electric field will be a superposition of the two wavefronts; one coming from the reference mirror and one coming from the SLM. Denoting the SLM phase aberration as $W(x, y)$, the phase of the reference mirror given as $\phi(x, y)$, the electric field at the interferometer camera can be expressed as

$$\begin{split} E(x,y,t) = A_r(x,y)\exp\left(i(k\phi(x,y) - \omega t)\right) + \\ A_{SLM}(x,y)\exp\left(i(k(\phi(x,y) + kW(x,y)) - \omega t)\right), \end{split} \tag{3.1}$$

where A_r and A_{SLM} are the amplitudes of the reference beam and the beam from the SLM respectively, k is the wavenumber equal to $\frac{2\pi}{\lambda}$, and ω the angular frequency of the light used. However, it is not the electric field which can be measured with the camera, only the irradiance. Hence, the intensity measured at the camera can be expressed as

$$I(x,y) = A_r(x,y)^2 + A_{SLM}(x,y)^2 + 2A_r(x,y)A_{SLM}(x,y)\cos\left(kW(x,y)\right). \tag{3.2}$$

Note that the time dependence in the intensity disappears. The intensity at point (x, y) is now only dependent on the phase difference kW, and the intensity varies between a minimum intensity of $I_{min} = (A_r - A_{SLM})^2$ and a maximum intensity of $I_{max} = (A_r + A_{SLM})^2$. This intensity is also cyclic, meaning that the intensity is the same value for $kW = a$ as it is if $kW = a + 2\pi$. Figure 3.2 shows a few interference patterns from low order Zernike aberrations produced with this type of interferometery setup. Interferometers are discussed in more detail in chapter 1 of Malacara (2007).

Using this information on how to obtain the interferogram patterns based on the aberrations, one can check if the aberrations are added correctly by comparing the measured interferogram with the expected one.

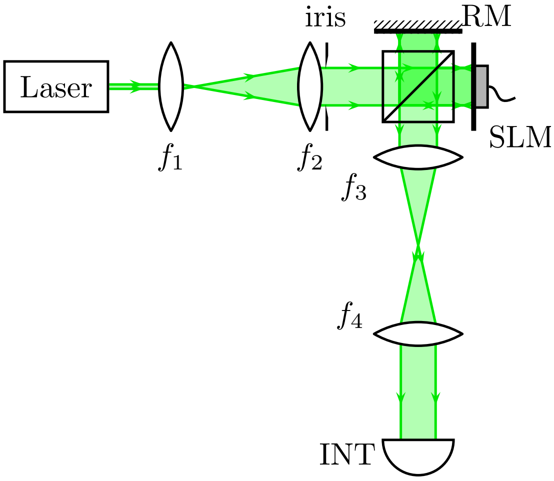

Figure 3.1: Simplified version of the interferometer setup used in the current research. Modeled after a Michelson interferometer.

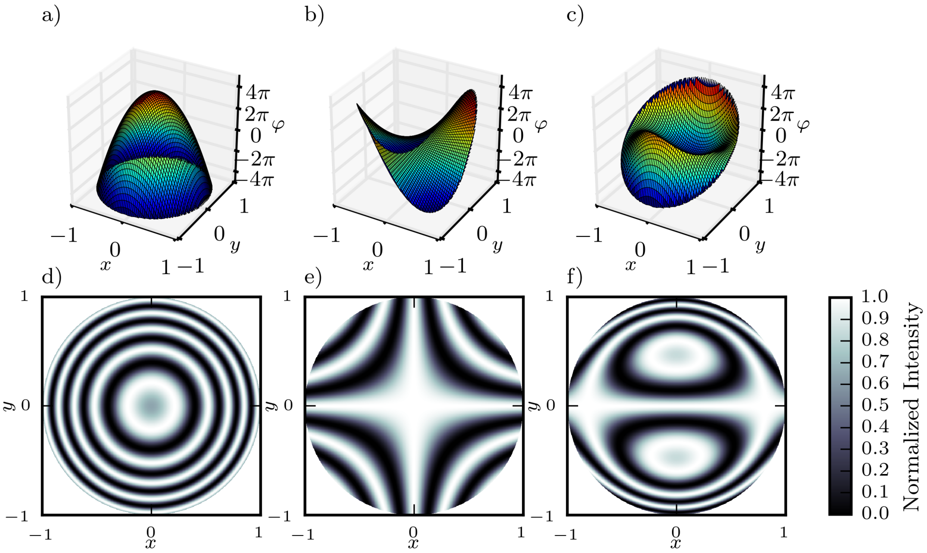

Figure 3.2: Low order Zernike aberrations and their associated interferograms. a) defocus, b) astigmatism and c) coma, d) to f) their respective interferograms.

3.1.2 Arms can be blocked to create the reference and aberration spot pattern

If one replaces the interferogram camera with a Shack-Hartmann sensor, one is almost able to use it directly for measurements. As explained in Section 2.2, the wavefront can be recovered based on a displacement of spots. To measure these reference spots, a uniform intensity plane wave should be incident on the Shack-Hartmann sensor. An approximation of this reference plane wave can be achieved if one blocks the beam path between the beamsplitter and the SLM. That way, only the beam from the reference mirror reaches the Shack-Hartmann sensor. If the mirror is flat enough, the reference beam can be considered a plane wave.

After this reference has been established, one can block the beam between the beamsplitter and the reference mirror, to get a spot pattern created by the phase pattern introduced by the SLM.

3.2 A spatial light modulator is used to add controlled aberrations

One way of altering the phase of a light beam is by using a spatial light modulator (SLM). In the current research, a liquid crystal on silicon (LCOS) SLM is used. A schematic cut-through of an LCOS SLM is shown in Figure 3.3. There it can be seen that the SLM consists of a silicon backplane with electrodes. These electrodes are pixelated, meaning there are many of them arranged in a matrix which can be addressed individually. Below the glass substrate on the top is a transparent electrode, which is used together with the pixelated electrodes to apply a voltage over the liquid crystal layer.

The liquid crystals can be seen as a uniaxial birefringent material. This means that the refractive index of the material changes with the polarization and propagation direction of the light. In Figure 3.3 the crystals are displayed as ellipsoids, and in Figure 3.4 it is shown that the lengths of the axes of these ellipsoids indicate the refractive index direction. The alignment layers make sure that the liquid crystals are aligned in a certain direction in the “off”-state (i.e. when no voltage is applied). When a voltage is applied, the alignment of the liquid crystals is changed and with that the refractive index of the birefringent material.

The input light in the spatial light modulator therefore undergoes a different optical path with different length dependent on the voltage applied to each pixel. In this fashion, the phase retardation of the incoming light can be modulated effectively on a pixel by pixel basis.

It is important to note that the SLM is calibrated with a certain polarization direction of light, due to the alignment layers dictating the preferred direction in the off-state. This polarization is important when designing the final setup, and is discussed at the end of the next Section.

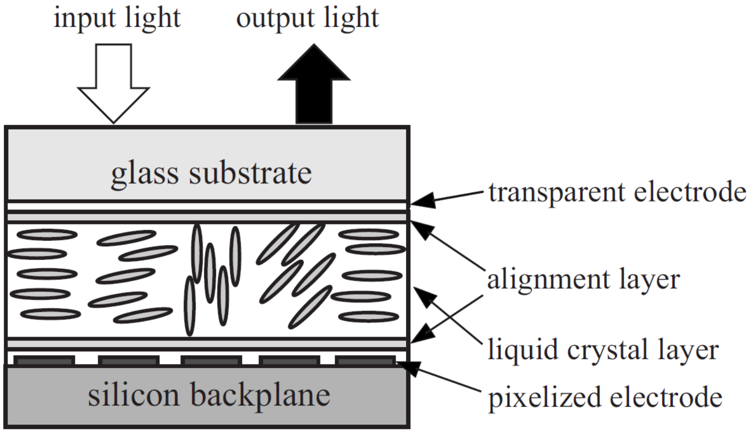

Figure 3.3: A schematic cross-section of an LCOS SLM device. Adapted from Matsumoto et al. (2008).

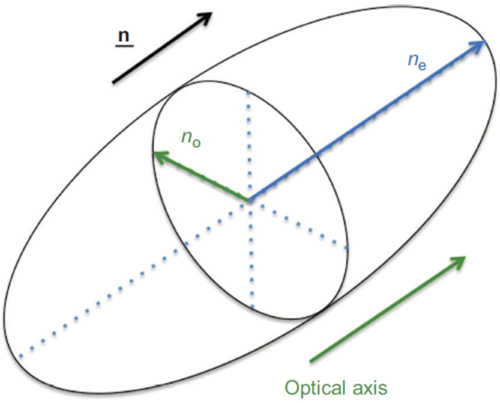

Figure 3.4: Schematic overview of the refractive indices of the liquid crystals, whereby n_o the ordinary refractive index and n_e the extraordinary index. Adapted from Zhang et al. (2014).

3.3 An iris and lens combination is used to block the zeroth order reflected light

As shown in figure Figure 3.3, part of the silicon backplane is not covered by the electrodes. This means that part of the the incoming beam is reflected without any modulation, even if there is a voltage over the electrodes. This is called the zeroth order reflected light. If this is left, the final wavefront would consist of both unaberrated and aberrated phase.

In order to remove this zeroth order reflected light, the aberration addressed to the SLM is altered. On top of the original aberration, a phase ramp is added. This phase ramp in terms of aberrations is a constant tip/tilt. It is known from Section 2.2.1 that adding a constant tip/tilt to the phase of the beam before a lens shifts the peak intensity in the focal plane. Using this shift, the SLM can be tilted in exactly the opposite direction to counteract this shift. The light hitting the space where no electrode is present would not be aberrated, and this constant tip/tilt will not be present in the phase of the unaberrated light. Due to the angle of the SLM, this unaberrated light will reflect at a different angle. This difference in phase pattern of the aberrated and unaberrated light make it so that when focused with a lens, the spots of the aberrated and unaberrated will not coincide, but will be spatially apart. This displacement enables the separation of aberrated and unaberrated light using for instance a iris. This effect can be seen in Figure 3.5. The zeroth order light is indicated with a more grayish beam, and is seen hitting the iris. The aberrated light is the greenish one, and can be seen to hit the iris exactly in the center.

The total amount of displacement of the zeroth order light is given by the angle θ with which the SLM is slanted and the focal length of lens f_3. From Zhang et al. (2009), the displacement Δl of the spot is determined as

$$\Delta l = f \tan\theta, \tag{3.3}$$

The maximum angle used in this research is determined by the SLM pitch (the physical distance between the centers of the SLM pixels). In order to prevent aliasing in the added phase pattern, the maximum phase difference over 4 pixels vertically or horizontally is 2π. Because the aberration under inspection has to be added on top of the phase ramp on the SLM, it is determined that the added phase ramp will be 2π over 8 pixels. An added phase of 2π means that the wave has a full wavelength of retardation. Using this, $\tan\theta$ can be substituted in Equation 3.3. The displacement Δl can then be written in terms of the wavelength of used light and the pitch, namely

$$\Delta l = \frac{\lambda f}{8p}, \tag{3.4}$$

where p is the pitch of the SLM. The radius of the iris should be slightly smaller than this displacement.

Knowing this maximum iris size, one is able to calculate if the desired added aberration “fits” within the pinhole by calculating the spot size using Equation 2.22. However, in the setup used in the current research, the limiting factor was not the pinhole size, but rather the aliasing constraint on the SLM. The aberration was kept within the iris by keeping the tip/tilt component of the added aberrations low.

What also can be seen from this setup (shown in Figure 3.5, with a parts list in Table 3.1) are the added components of a Faraday rotator (FR), a filter, a half-wave plate ($\lambda/2$), and the Shack-Hartmann sensor. The Faraday rotator is placed to protect the laser from any reflected light, the filter is used to regulate the intensity such that both cameras are not saturated, and the half-wave plate can be rotated such that the polarization of the beam coincides with the required polarization of the SLM.

The last section of the new setup contains a beamsplitter to split the incoming beam to the Shack-Hartmann sensor and to a CCD camera. With this camera one can take a look at the interferogram when both arms are not blocked. This is in order to see if the SLM is adding the correct phase pattern, to see if the initial aberrations of the system are adequately removed, and to look at the alignment of the system. In this arrangement, the setup can be used to do all the necessary steps for successful measurements with the Shack-Hartmann wavefront sensor. These necessary steps are described in more detail in Section 4.

Table 3.1: The components used in the current research. The setup is shown in Figure 3.5.

Part	Description
Laser	Melles Griot frequency stabilized, linearly polarized He-Ne laser
FR	Faraday Rotator to protect the laser from reflections
filter	Grey glass uniform filter
$\lambda/2$	Half-wave plate
f_1	focal length 25mm
f_2	focal length 500mm
RM	Edmund optics mirror, $\lambda/20$ flatness
SLM	Holoeye PLUTO-2-VIS-056
f_3	focal length 250mm
f_4	focal length 250mm
SH	Custom microlens array (pitch = 5 2µm, f =17 6mm) with UI-3370CP CMOS camera
INT	SVS-Vistek eco1050MTLGEC - GigE CMOS camera

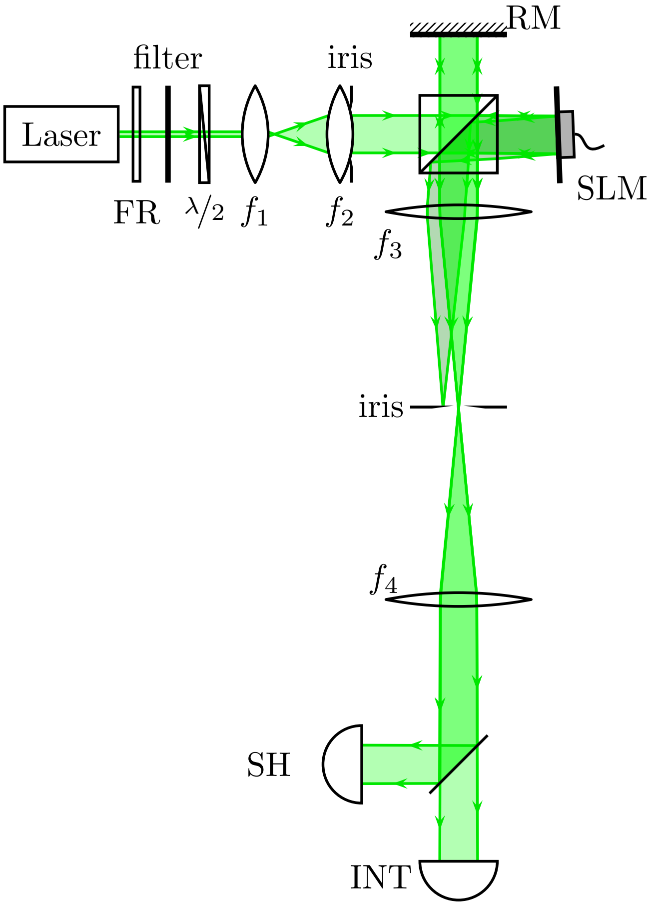

Figure 3.5: Altered interferometry setup to filter out the zeroth order reflection from the SLM. The zeroth order light is shown in gray. The components used in the current research are noted in Table 3.1.

4 Experimental method

Using the described experimental setup, all steps necessary to compare Janssen's method to the least-squares method can be performed. All necessary steps are shown in Algorithm 1, and separately described in more detail in their respective subsections.

Algorithm 1 Complete measurement and comparison of Shack-Hartmann phase retrieval algorithms

```
Remove initial aberrations of the entire system (described in Section 4.1)
Add controlled aberration $\mathbf{a}$ to the SLM (described in Section 4.2)
Gather flat and aberrated wavefront Hartmannograms [1]
Find the optimal center and radius position for both methods separately
  such that the RMS value is minimized (described in Section 4.3)
Calculate Zernike coefficients for both methods using optimized center
  and radius for all desired Zernike powers
Calculate error landscape by varying center position and radius
```

4.1 The initial aberrations are removed using the SLM

In order to be certain that only the aberration added on the SLM is measured, first all initial aberrations are minimized. These aberrations can include alignment errors, but also aberrations stemming from the fact that the SLM might not be completely flat (Matsumoto et al., 2008).

Removing the initial aberrations is done using the Shack-Hartmann sensor and retrieving the wavefront using the least-squares method. The steps necessary for this process are described in pseudocode in Algorithm 2.

Recalling from the theory described in Section 2.2, in order to recover the coefficients describing the aberrated wavefront, $\mathbf{s}$ and G have to be constructed. $\mathbf{s}$ relies on the two Hartmannograms, one of the flat wavefront of the reference mirror and one of the aberrated wavefront from the SLM; and the radius r_{SH} of beam hitting the Shack-Hartmann sensor.

To construct G it is necessary to average the Zernike polynomials or their gradients, dependent on the reconstruction method. The window over which the polynomial has to be averaged can be seen as a scaled version of the lenslet, scaled so that all illuminated lenslets fit the unit disc. In order to compute the Zernike polynomials in these windows, the center position $\mathbf{c}$ and the radius r_{SH} of the beam on the Shack-Hartmann sensor have to be known. The window size is estimated by the average distance between the nearest neighbor spots on the Shack-Hartmann sensor. The side length of the window is denoted with `box_len`. The center position $\mathbf{c}$ is estimated at

---

[1] Hartmannogram is the image of the spot pattern generated by the Shack-Hartmann sensor

first as the center of mass of all the spots on the Shack-Hartmann sensor. The radius is estimated by calculating the length between the center and the furthest spot from the center.

Algorithm 2 Removal of initial aberrations

```
Require: $f_{\mathrm{SH}}$
Apply phase ramp to SLM
Acquire Hartmannogram flat wavefront
From Hartmannogram, estimate center $\mathbf{c}$, radius $r_{\mathrm{SH}}$, box_len
Given $\mathbf{c}$, $r_{\mathrm{SH}}$ and the Hartmannogram, generate geometry matrix $G$
for $i \in \{0, 1, 2, 3\}$ do
    Acquire Hartmannogram of SLM wavefront
    Calculate $\mathbf{s}$, given $r_{\mathrm{SH}}$, $f_{\mathrm{SH}}$ and both Hartmannograms
    Calculate $\hat{\mathbf{a}} \approx G^{+}\mathbf{s}$
    Add $-\gamma\hat{\mathbf{a}}$ to the SLM pattern
end for
```

Here, $\gamma \in [0, 1]$, and is chosen to be 0.5 in the current research. Also, $\hat{\mathbf{a}}$ denotes the vector of *estimated* coefficients. Using this parameter, it was found that repeating the measurement and correction 4 times was enough to have the wavefront flat enough for measurements.

The way a phase pattern is addressed to the SLM is as follows. First, an aperture on the SLM is defined. In the current research this is a circular aperture, but it can also be done using an annular one. All pixels i within this aperture are noted. A "Zernike matrix" can be set up, such that for each pixel i within the aperture the value of all necessary Zernike polynomials can be computed. In matrix form this would be

$$Z = \begin{bmatrix} Z_1|_1 & Z_2|_1 & \cdots & Z_J|_1 \\ Z_1|_2 & Z_2|_2 & \cdots & Z_J|_2 \\ \vdots & \vdots & \ddots & \vdots \\ Z_1|_I & Z_2|_I & \cdots & Z_J|_I \end{bmatrix}, \tag{4.1}$$

where J is the total amount of Zernike polynomials evaluated, and I is the total amount of pixels within the aperture. Due to the cyclic nature of the phase pattern (as explained in Section 3.1) and the limits of the SLM, the phase difference assigned to the SLM should be between 0 and 2π. This can be done using the modulo (or mod) operation. $a \bmod n$ gives remainder of a divided by n.

If $\mathbf{p}$ is a vector containing the values of the individual pixels of the SLM, it can be constructed from the vector $\mathbf{a}$ containing the coefficients for the to-be-added aberration by

$$\mathbf{p} = (Z\mathbf{a}) \bmod 2\pi. \tag{4.2}$$

Therefore, in the case of updating the SLM pattern in line 9 of Algorithm 2, one can use

$$\mathbf{p}_{new} = (\mathbf{p}_{old} - \gamma Z\hat{\mathbf{a}}) \bmod 2\pi. \tag{4.3}$$

4.2 A controlled aberration is added and measured

After the correction is done and the wavefront from the SLM is flattened, the phase pattern of the "flat" phase is saved. To this phase pattern the aberration is added, in the same fashion as the correction is added.

After this is added and modulated, it is necessary to check if the the maximum phase change over 4 pixels is not being exceeded. This is necessary to check if aliasing of the SLM phase will not occur. In the current research this aliasing constraint is simplified to the constraint that the difference between two neighboring pixels should not exceed 0.5π. This is evaluated in the following way:

Let $p_{i,j}$ be the value of the pixel located at position i, j on the SLM electrode matrix. Then first two matrices are constructed

$$\begin{aligned} \Delta p_x &= p_{i,j+1} - p_{i,j}, \\ \Delta p_y &= p_{i+1,j} - p_{i,j}. \end{aligned} \tag{4.4}$$

Afterwards, the element-wise minimum is taken between Δp and $2\pi - |\Delta p|$ for both x and y, in order to account for the modulated phase. If any of the values of this piecewise minimum is above 0.5π, it is said to break the aliasing constraint.

After the aliasing test has been passed, and the phase has been applied to the SLM, the aberrated phase can be looked at using the interferometer camera. If visually everything is correct as well, the Hartmannogram can be taken.

4.3 The center position and radius are found optimizing the error at 8 Zernike powers

In order to perform both reconstruction methods, the radius and center should be known or estimated before reconstruction can be done. The slopes vector $\mathbf{s}$ is dependent on the radius of the beam hitting the Shack-Hartmann sensor (due to the scaling with r in Equation 2.29), while the geometry matrix G is dependent on both the center-position of the beam on the sensor and the radius. In order to fairly judge both methods, rather than estimating the center and radius, these parameters are found by optimization. The initial guess for these parameters are the same as the parameters used in the removing of initial aberrations. Using the methods described in Section 2.2.2 and Section 2.2.3, the coefficients can be gathered from the Hartmannograms.

Using the known added aberration and the measured aberration coefficients, an RMS error can be defined. For this, a new Zernike matrix similar to Equation 4.1 is constructed, this time with N points on a grid within the unit disc. The reference phase $\mathbf{p}_{\text{ref}}$ and the recovered phase $\mathbf{p}_{\text{rec}}$ can be constructed as

$$\mathbf{p} = Z\mathbf{a}, \tag{4.5}$$

where for $\mathbf{p}_{\text{ref}}$, the reference vector $\mathbf{a}_{\text{ref}}$ is used, while for $\mathbf{p}_{\text{rec}}$ the estimated coefficient vector $\hat{\mathbf{a}}$ is used. Using this definition for the reference and recovered phase, the RMS error is determined as

$$\varepsilon = \left\| \frac{\mathbf{p}_{\text{ref}} - \mathbf{p}_{\text{rec}}}{N} \right\|_2, \tag{4.6}$$

where $\|\mathbf{x}\|_2$ is the Euclidean vector norm of vector $\mathbf{x}$.

This RMS error is then minimized for center position and radius of the beam on the Hartmannogram. A limited memory bound Broyden-Fletcher-Goldfarb-Shanno (L-BFGS-B) minimization algorithm is done to find the center position and radius separately for both the least-squares method and Janssen's method. The termination conditions for this optimization were

$$\begin{aligned} \frac{f^k - f^{k+1}}{\max\{|f^k|, |f^{k+1}|, 1\}} &\leq 10^{-5}, & (4.7)\\ \max\{|\text{proj}(g_i)|\ i = 1, ..., n\} &\leq 10^{-5}, & (4.8)\\ k &\geq 10^3, & (4.9) \end{aligned}$$

where f^k is the value of the RMS error of the k^{th} iteration of the minimization algorithm, and $\text{proj}(g_i)$ is i^{th} component of the projected gradient where n projections are made. If any of these statements were true, the optimization was terminated. After looking at the RMS error landscapes, it was found that not every minimum found was a global minimum. If this was the case, the global minimum coordinates were estimated using the RMS landscape graphs, and a brute force optimization was run around those coordinates. This brute force optimization calculates the RMS error value in a grid of points. From the coordinates with the lowest RMS error, a new downhill simplex minimization algorithm is started. This way the global minimum was attempted to be found, and the optimal center and radius positions were determined.

In the current research, the necessary aberration coefficients are obtained using 8 Zernike powers. From Soloviev and Vdovin (2006) it is concluded that a good rule of thumb for the amount of Zernike polynomials that can be fit given k spots on the Shack-Hartmann sensor is ${}^{k}\!/_{3}$. In the current research, there were about 144 spots on the Shack-Hartmann sensor, and there are 45 polynomials in the first 8 Zernike powers.

For Janssen's method, the amount of polynomials fit and the amount of retrieved coefficients is different. If a fit is made with up to 8 powers of Zernike polynomials, the first 7 powers of coefficients can be retrieved. For the most fair comparison, it is chosen to keep the amount of Zernike powers used for fitting the same for both experiments. This has as a consequence that whenever the methods are compared, Janssen's method's coefficients will contain one power less than the least-squares method. The effects of this are discussed in the results.

It should be noted that this optimization can take long due to the fact that the geometry matrix needs to be calculated in every iteration, as the values in the matrix differ with center position and radius.

These optimized parameters can then be used to find the RMS value fitting any amount of Zernike powers, and can also be used to determine the error landscape by calculating the RMS values when the center and radius differ slightly from the optimal value. This landscape is found using 8 Zernike powers in the current research.

The RMS error landscape is determined by displacing the center position a certain amount ($disp$) and varying the radius of the beam on the Shack-Hartmann sensor Δr. The displacement is shown in Figure 4.1 where it can be seen that there are 8 concentric circles (including a circle with radius 0), all containing 7 displacements. The concentric equally spaced between 0 and 3 pixels, and the angles between the measurement points are equally spaced between 0 and 2π (not including 2π). At all of these data points, the the RMS error is calculated for 7 different radii Δr, equally spaced between -3 pixels and $+3$ pixels with respect to the optimized radius. A surface is plot as a function of displacement $disp$ and radius difference Δr. This surface is plot through the median of the of 7 values on a concentric circle. Error bars show the maximum and minimum value on the circle.

In order to compare the least-squares method to Janssen's method, it is not the RMS error ε that is shown, but rather a normalized version of this. The normalized RMS error is defined as

$$\varepsilon_{norm}(disp, \Delta r) = \varepsilon(disp, \Delta r) - \varepsilon(0, 0). \tag{4.10}$$

This is done such that all errors are in the range $[0, \infty)$, and both errors can be shown on the same scale. These error landscapes can be seen in Section 5.4

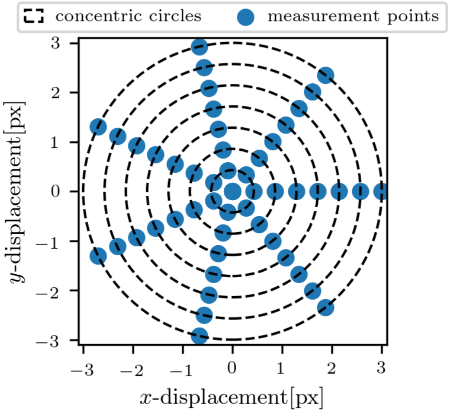

Figure 4.1: The measurement points in the xy-plane with which the RMS error landscape is determined. The concentric circles are equally spaced between 0 and 3 pixels, and the angle between the measurement points are equally spaced between 0 and 2π (not including 2π).

5 Results

In order to compare the least-squares method and Janssen's method, three different test cases have been measured and analyzed. First, specific Zernike aberrations were added to see the effect of different combinations of Zernikes. From Section 2.2.4 it is known that the least-squares method presents cross-talk between estimated coefficients while Janssen's method is hypothesized not to show this. Therefore, in the first set of aberrations added, three cases are defined. First only single aberrations are added as a zero-measurement to see if with only one present aberration they perform equally. Afterwards, a combination of three aberrations are added that are not supposed to show cross-talk. Lastly, four cases of aberrations are added where cross-talk is present. The aberrations are shown in Figure 5.1, and the table with exact coefficients in Table E.1.

The second set of aberrations measured were taken from a Leica microscope objective. These aberrations were measured by Leica at two different wavelengths, 365 nm and 544 nm, and both aberrations were implemented with different peak-to-valley values, but keeping the ratios the same. The aberrations are shown in Figure 5.2, and the table with exact values for the coefficients in Table E.2 and E.3. These coefficients present a set of aberration coefficients which occur in a lens-measurement setting.

The third set of aberrations measured are created by a random phase pattern. This random phase pattern was filtered using a two-dimensional Butterworth filter with different cut-off frequencies to vary the magnitude of high spatial frequency components. After the filtering, up to 10 Zernike powers are fit to this surface and the coefficients are saved. After this, the surface described by the Zernike coefficients is added, in order to have the exact value of all coefficients to compare to the measurements taken. The aberrations are shown in Figure 5.3, and the table with exact coefficients in Table E.4 and E.5. These sets of coefficients represent a set of coefficients which could occur when measuring the aberrations caused by turbulent air.

These experiments will first of all be used to show that the methods are equally accurate when using enough fitting powers. Afterwards, it is shown that Janssen's method better estimates the Zernike coefficients when using fewer fitting powers. Furthermore, it is shown that the RMS error landscapes are similar in shape and therefore both equally susceptible to errors in the center position or radius. Lastly, it is shown that due to using complex numbers, Janssen's method is at least 3.5 times slower than the least-squares method.

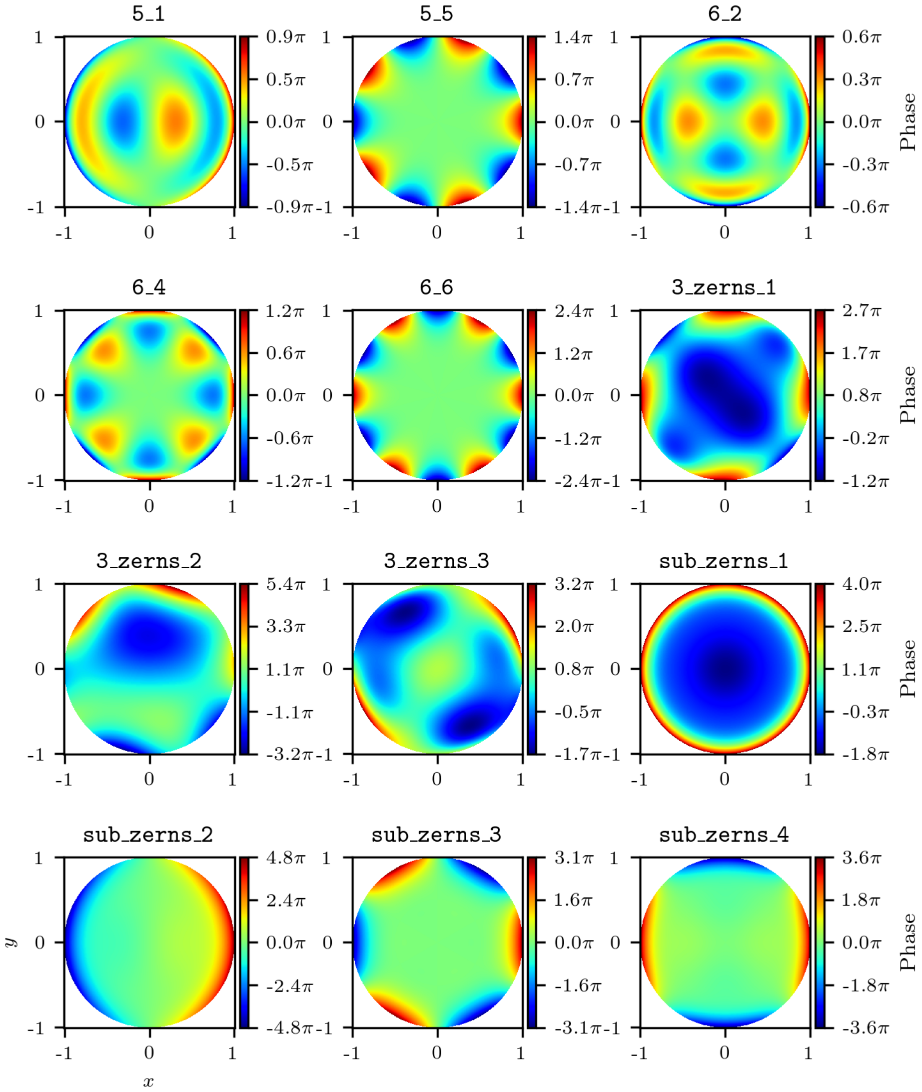

Figure 5.1: Visualization of the added phase patterns for the specific Zernike aberration case. Above the subplots is the code given to the measurement.

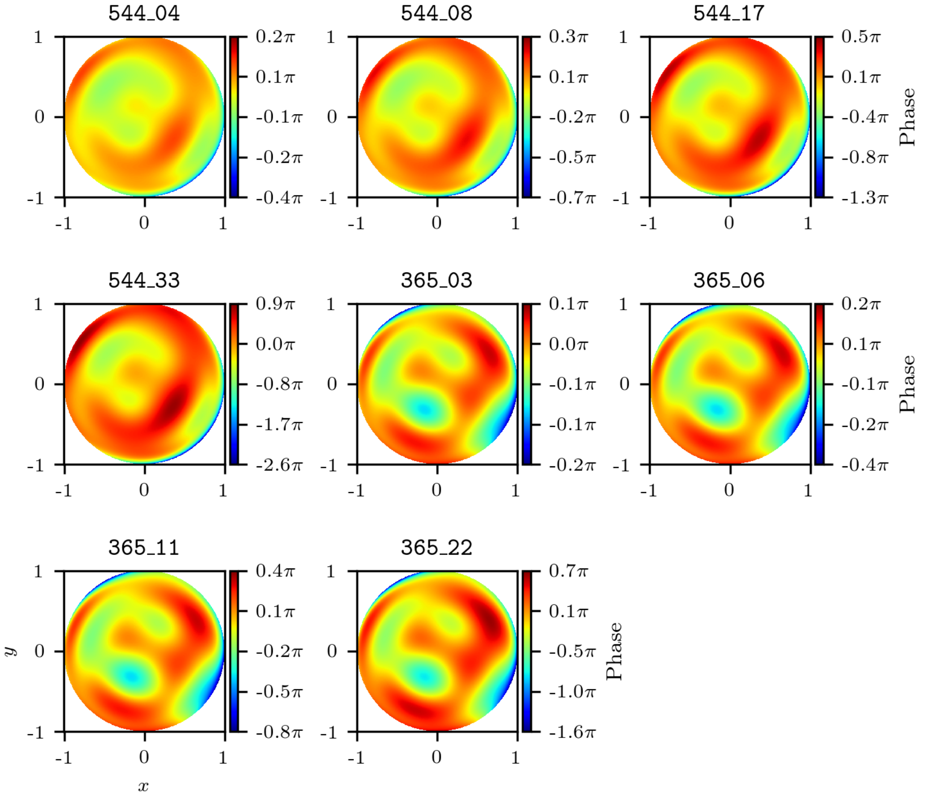

Figure 5.2: Visualization of the added phase patterns for lens aberrations case. Above the subplots is the code given to the measurement.

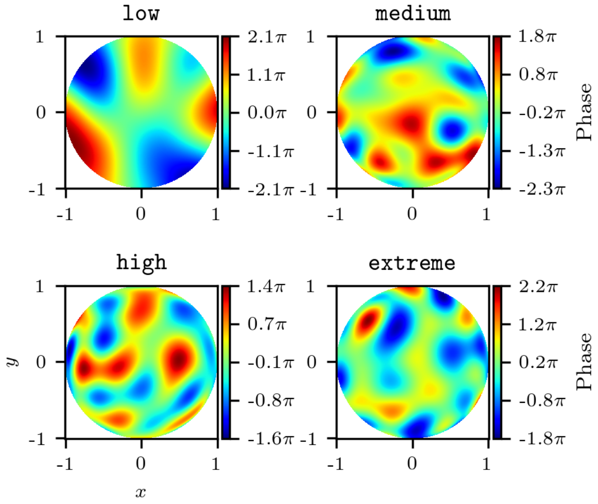

Figure 5.3: Visualization of the added phase patterns for the random phase aberrations case. Above the subplots is the code given to the measurement.

5.1 Least-squares method and Janssen's method have comparable accuracies with optimal amount of fitting powers

In order to compare accuracies of both methods, the optimal amount of Zernike powers are used when fitting. From Section 4.3 it is known that for the current research, that amount is 8 Zernike powers. The RMS error ε is determined using 600 points on an equally spaced grid. It has to be noted that when fitting 8 powers of polynomials, Janssen's method only can gather Zernike coefficients up to and including the 7^{th} power.

This subsection will show that throughout all experiments, Janssen's method and the least-squares method have comparable RMS error when using this optimal amount of Zernike powers.

5.1.1 Accuracy is comparable when adding specific Zernike aberrations

When looking at the specific Zernike aberration experiment, one can see that Janssen's method and LSQ method perform very similarly when fitting the optimal amount of Zernike powers, with an overview of the RMS errors in the barchart in Figure 5.4. Most notable differences are at `5_5` and `6_6`, where the LSQ method performs better, and at `3_zerns_1`, `sub_zerns_1` and `sub_zerns_4`, where Janssen's method performs better. The reconstructions using the recovered coefficients are shown in Figure 5.5, Figure 5.6 and Figure 5.7. From these figures it can be seen that also visually the least-squares method and Janssen's method compare very well.

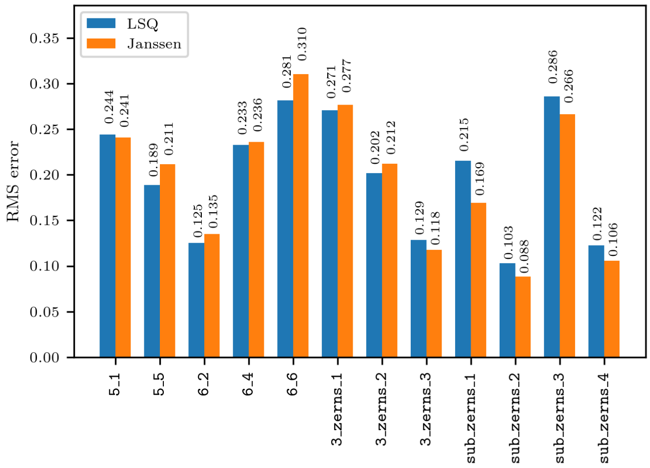

Figure 5.4: Barchart detailing the RMS values between the added specific Zernike aberration and the reconstructions using the LSQ and Janssen's method.

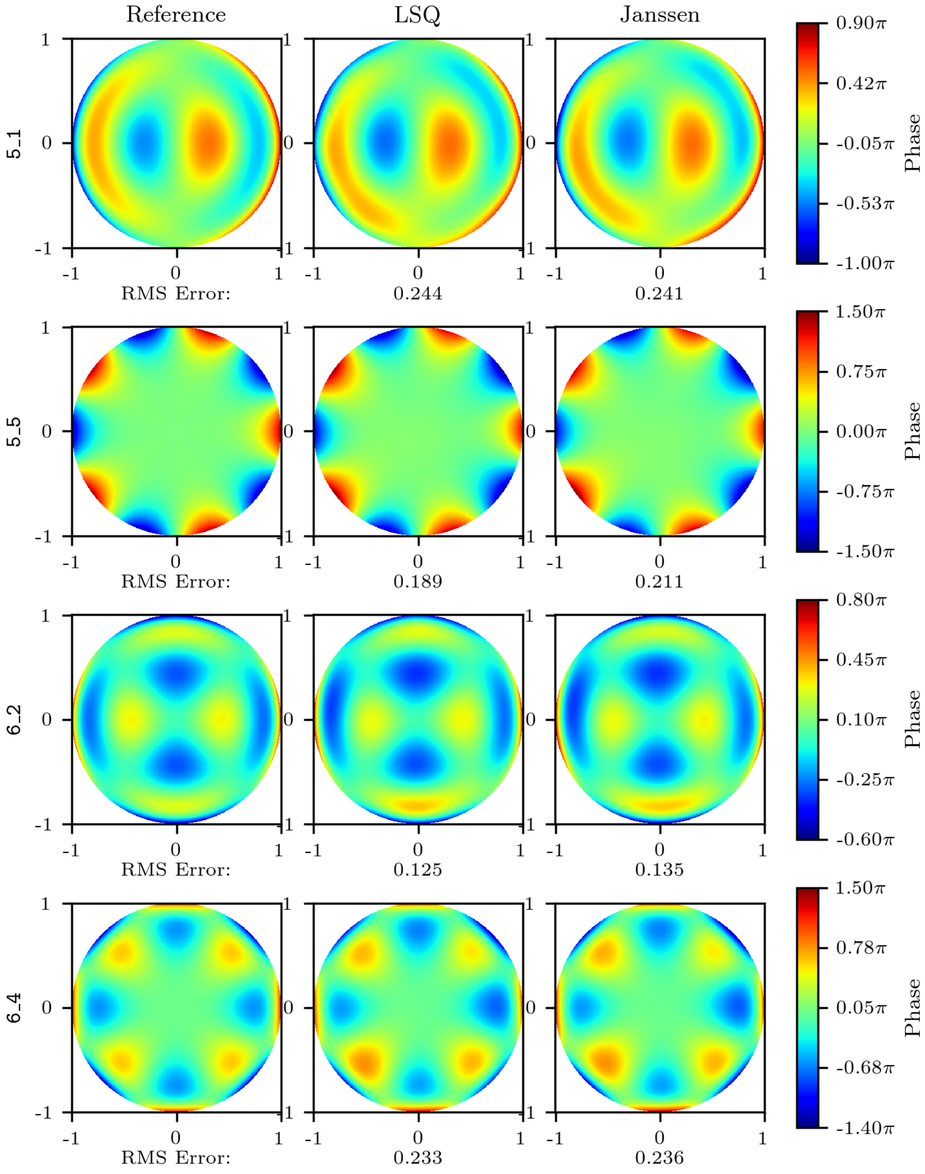

Figure 5.5: The first 4 added aberrations and their reconstructions of the specific Zernike experiment. RMS errors are noted below the reconstructions.

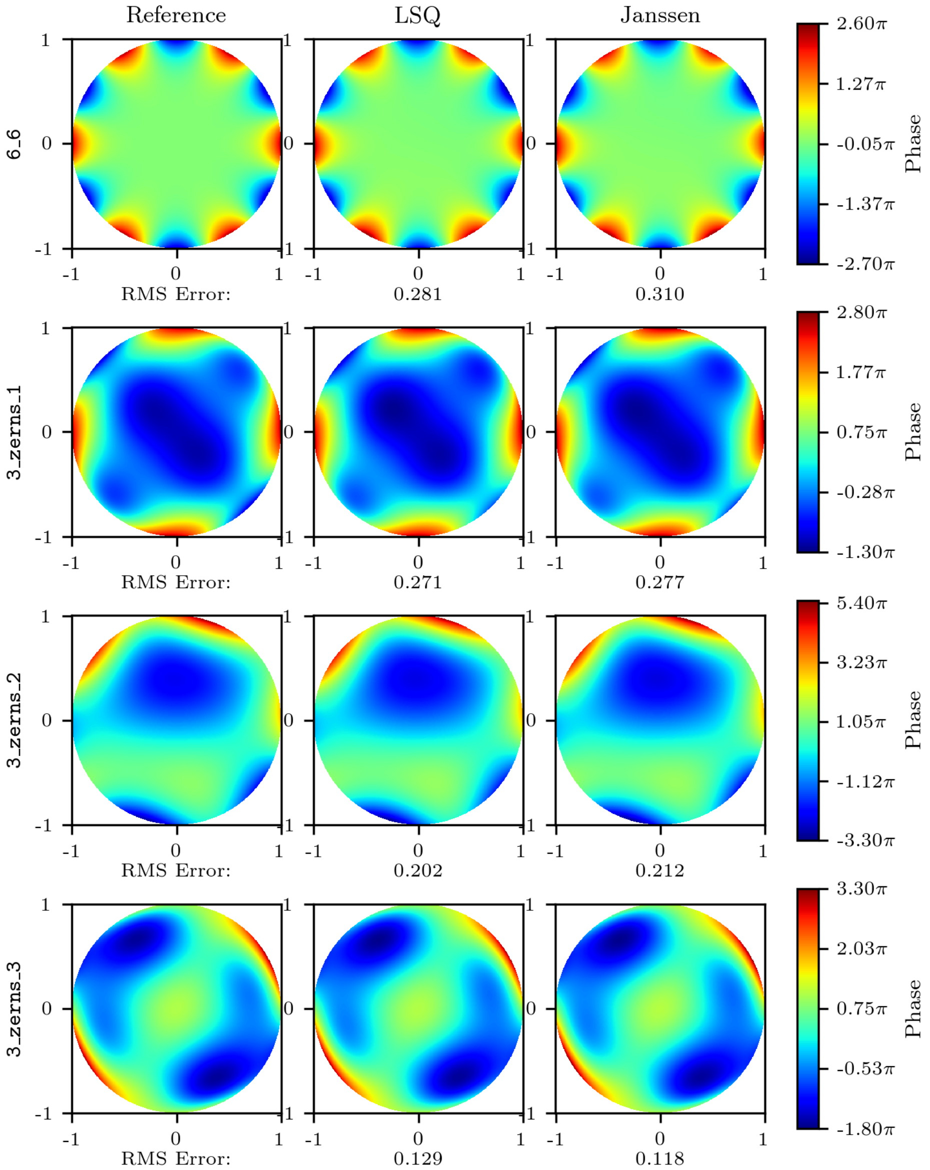

Figure 5.6: The second 4 added aberrations and their reconstructions of the specific Zernike experiment. RMS errors are noted below the reconstructions.

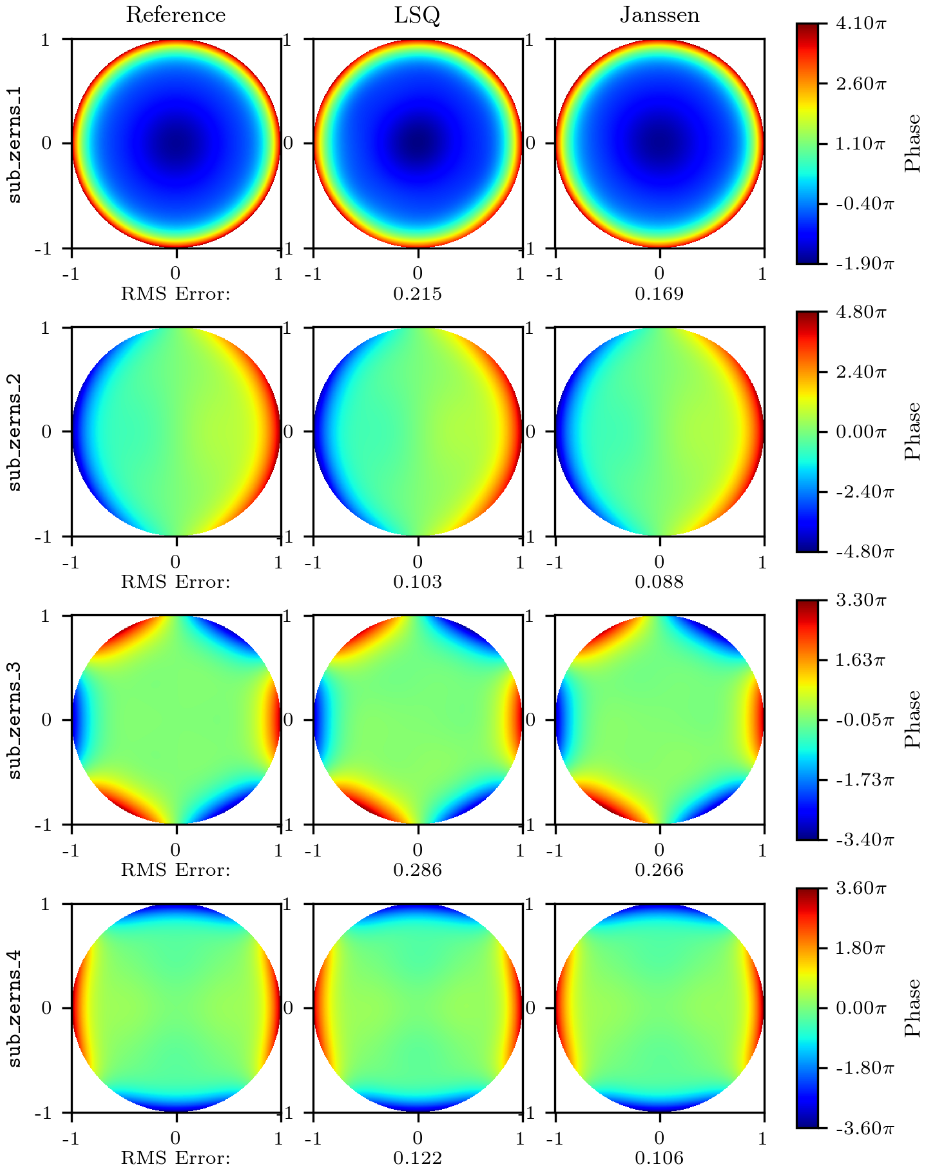

Figure 5.7: The last 4 added aberrations and their reconstructions of the specific Zernike experiment. RMS errors are noted below the reconstructions.

5.1.2 Accuracy is comparable when simulating lens aberrations

When looking at typical lens aberrations like the ones measured by LEICA, one can see that also these can be reconstructed well by both the least-squares method and Janssen's method. Again a barchart is made summarizing all the RMS values (shown in Figure 5.8). A trend that can be seen from this barchart is that when the peak-to-valley value of the aberrations go up, the error in Janssen's method also goes up. This can be explained by the fact that the influence of the higher order aberrations grows as the coefficient grows. Janssen's reconstruction is made with only 7 powers of coefficients, while the least-squares method has 8 powers of coefficients, and the lens aberrations are measured up to and including the tenth power. The experiments with lower peak-to-valley measurements show that these aberrations have less influence on the total RMS.

In Figure 5.9 this difference between the least-squares method and Janssen's method is visible in for instance the bottom right corner. The original aberration there is at its lowest there. In all four cases, Janssen's method overestimates the phase at the edge, while the least-squares method estimates it closer to it's original value. In Figure 5.10 this difference is seen in for instance the height of the central peak. In all four cases, Janssen's method underestimates the height of this peak, while the least-squares method estimates it closer to the reference height.

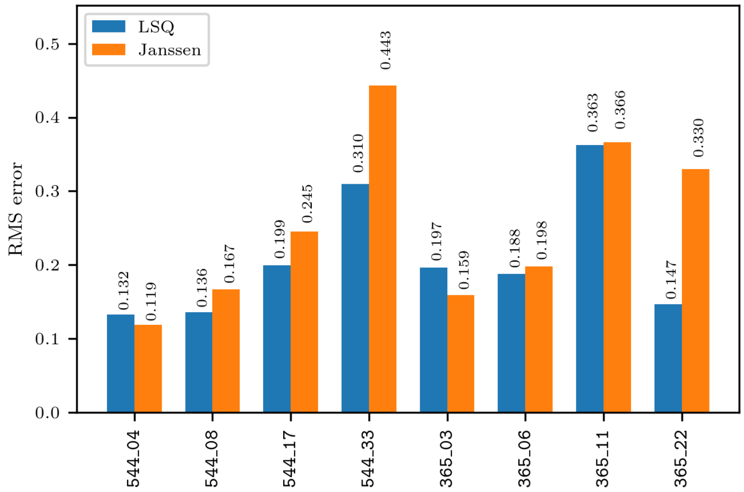

Figure 5.8: Barchart detailing the RMS values between the added lens aberration and the reconstructions using the LSQ and Janssen's method.

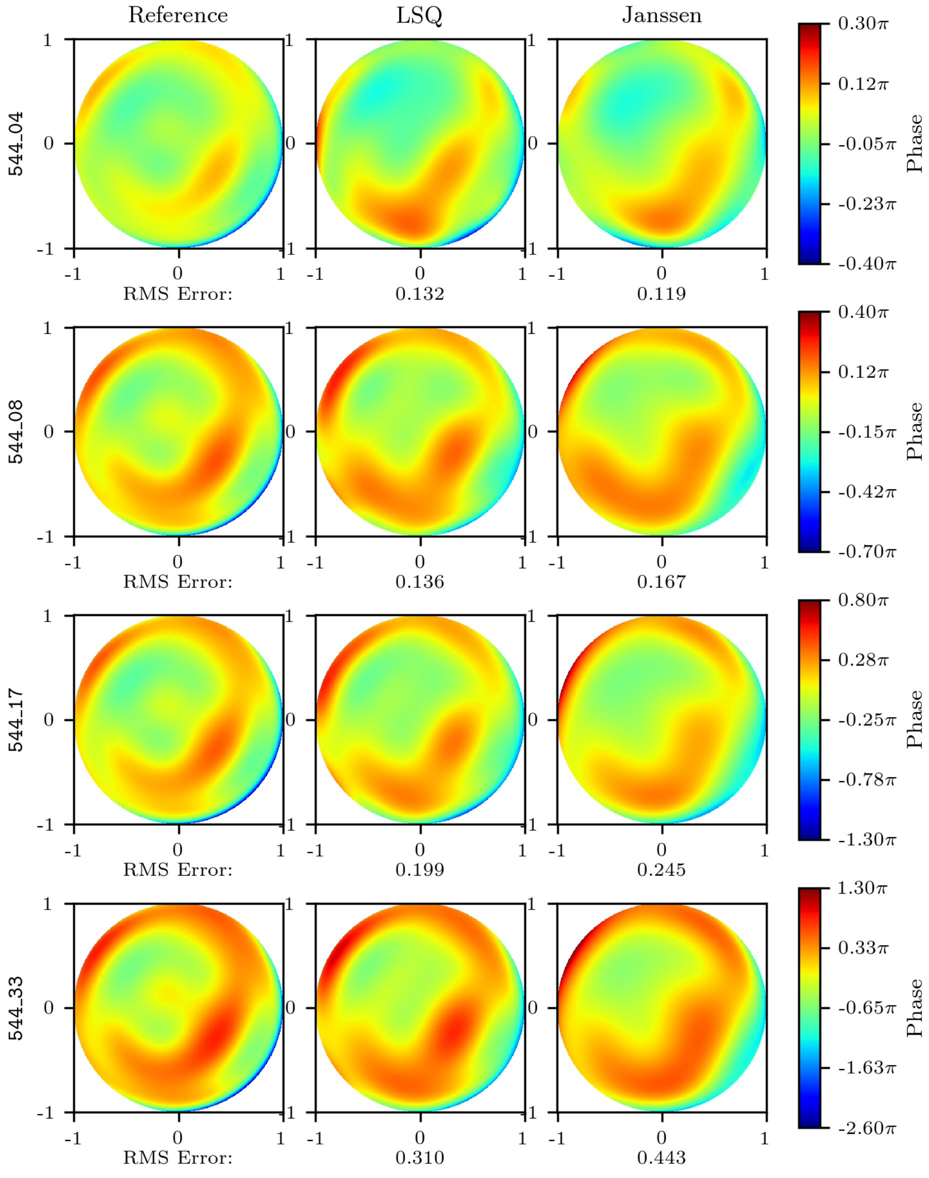

Figure 5.9: The added and reconstructed phases of the lens aberrations of the `544` series. The peak-to-valley ratio increases from top to bottom. RMS errors are noted below the reconstructions.

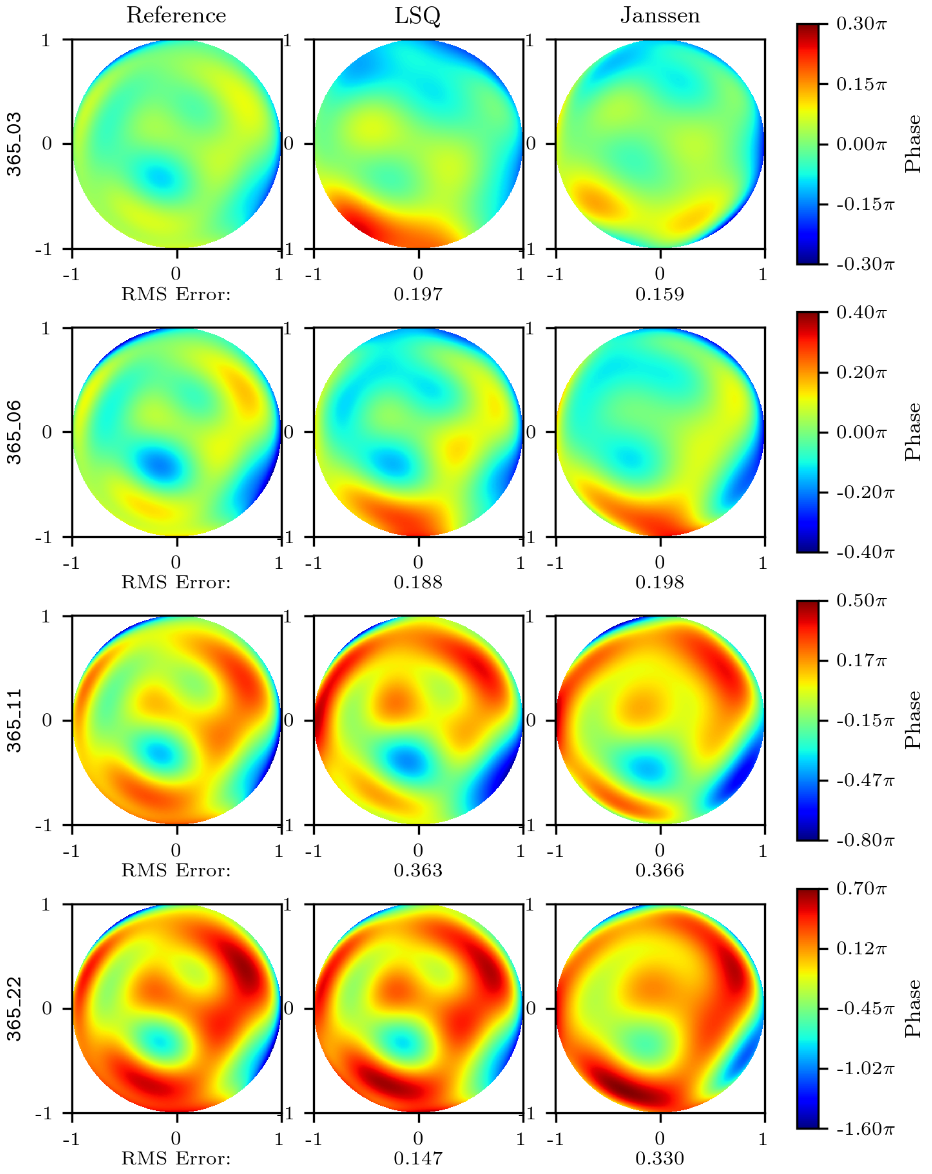

Figure 5.10: The added and reconstructed phases of the lens aberrations of the `366` series. The peak-to-valley ratio increases from top to bottom. RMS errors are noted below the reconstructions.

5.1.3 Accuracy is comparable when simulating a random phase pattern

From the barchart in Figure 5.11 it can be seen that for the random phase aberrations, for the low `low` measurement Janssen's method performs slightly better. For the rest of the measurements the least-squares method performs better. When the value of the RMS error is compared with the previous measurements one can see that this value is significantly higher. This is due to the fact that from `medium` onwards, the presence of higher order Zernikes is significantly increased. The Zernike coefficients present are shown in Figure 5.13. The fact that for both reconstructions the RMS value is significantly high is another indication that not all aberrations are measured, and the reconstructions shown in Figure 5.14 show visually that there is a great discrepancy between the reconstructions and the added aberration, apart from `low`.

This presumption is confirmed when looking at the RMS errors when fitting more Zernike coefficients to the measured data. When instead of fitting 8 Zernike powers, 9 Zernike powers are fit (barchart in Figure 5.12 and visual in Figure 5.15), one can see that the RMS errors decline in all cases where higher order Zernike coefficients are present. The least-squares method is seen again to have lower RMS values for the cases `medium`, `high` and `extreme` with respect to Janssen's method.

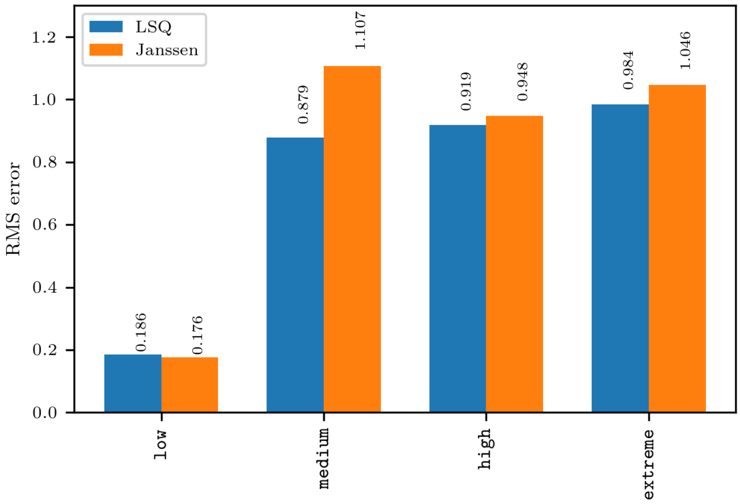

Figure 5.11: Barchart detailing the RMS values between the added random aberration and the reconstructions using the LSQ and Janssen's method.

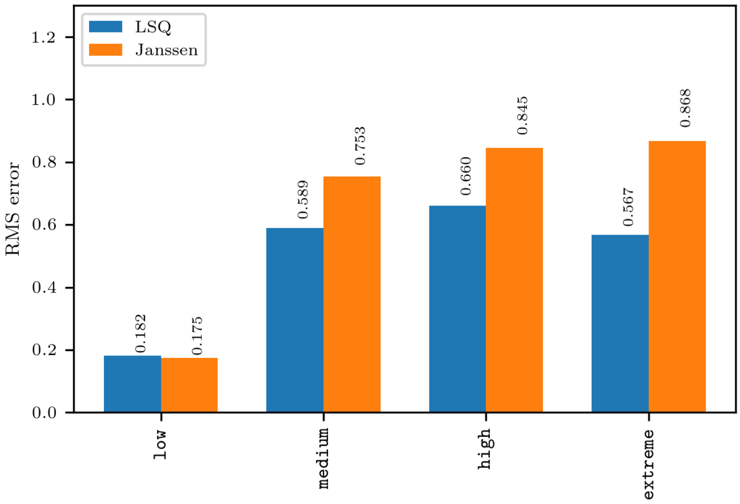

Figure 5.12: Barchart detailing the RMS values between the added random aberration and the reconstruction using 9 fitting powers using the LSQ and Jassen's method. Note that the y-scale is the same as in Figure 5.11.

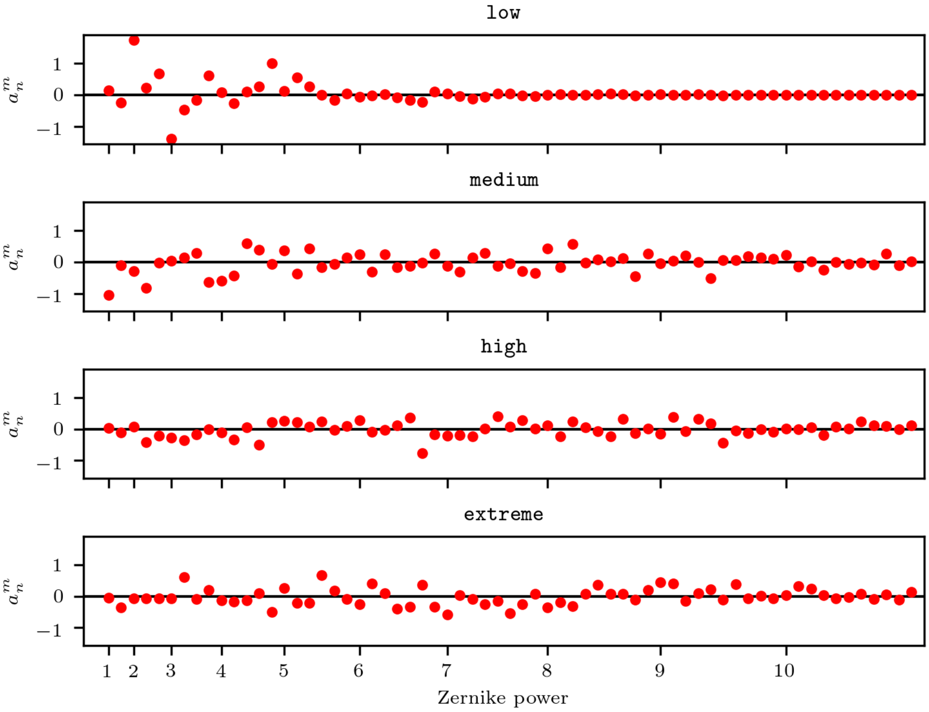

Figure 5.13: The added Zernike coefficients for the 4 random phase aberrations.

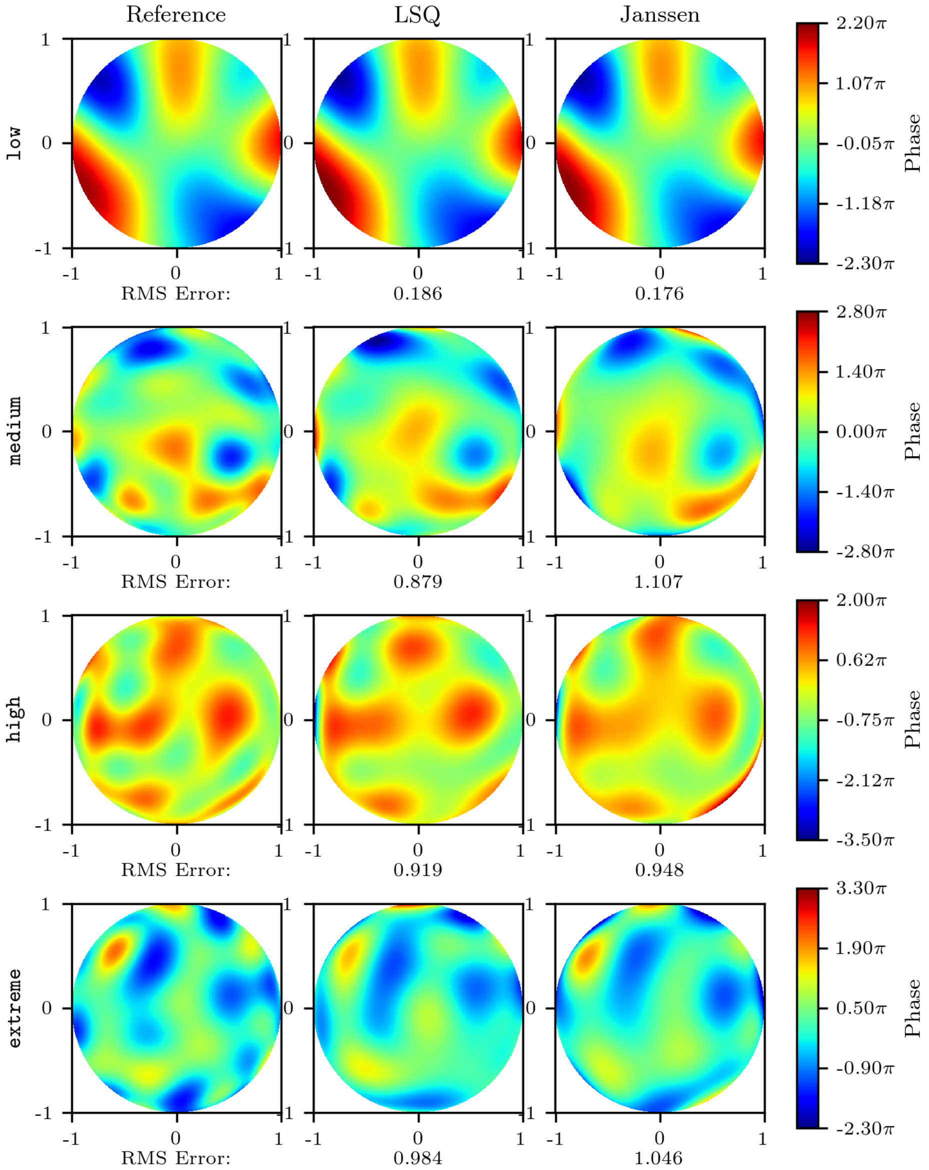

Figure 5.14: The added and reconstructed phases of the random phase pattern experiment. RMS errors are noted below the reconstructions.

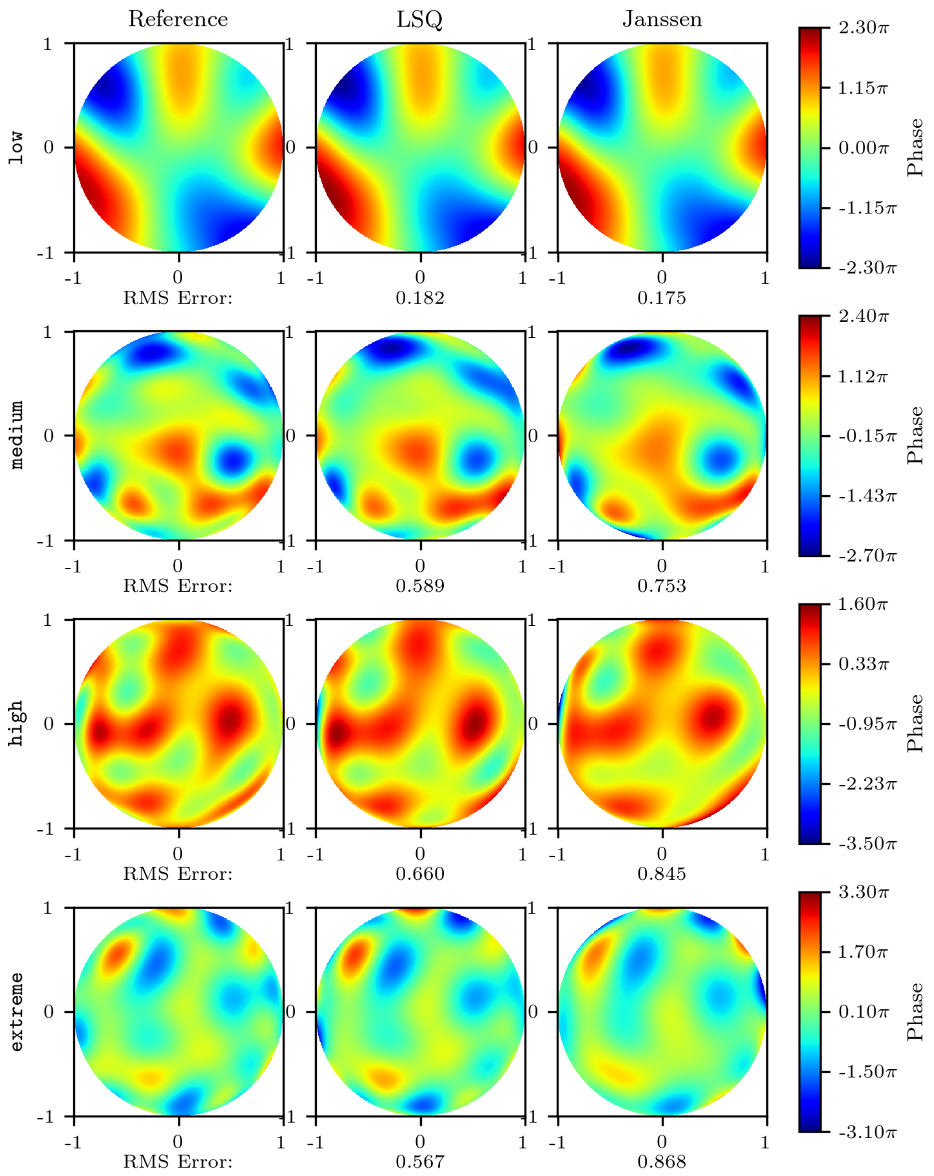

Figure 5.15: Reconstructions using 9 Zernike fitting powers, rather than 8. It can be seen that in the cases where higher order aberrations are strongly present, the RMS value drops for both reconstruction methods with respect to fitting 8 Zernike powers.

5.2 Janssen's method estimates more accurately with fewer fitting powers

The previous section has shown that when fitting 8 or 9 powers of Zernike polynomials, both Janssen's method and the least-squares method provide comparable accuracy in reconstructing the wavefront. However, it is known that the least-squares method presents cross-talk of coefficients when less Zernike powers are fit than there are aberrations present in the system, as shown in Section 2.2.4. In this section it is shown experimentally that this is not the case for Janssen's method. After this, statistical research using the absolute estimation error of the Zernike coefficients shows that Janssen's method is more accurate when fitting $n+1$ powers when estimating a_n^m (i.e. fitting 3 Zernike powers for the aberrations a_2^m).

5.2.1 Janssen's method does not present cross-coupling of aberrations

Using the same center position and radius, different amount of Zernike powers can be fit in order to see the convergence behavior of gathered coefficients. Due to the fact that there are only 1, 2, or 3 Zernike modes present in the specific Zernike experiment, the convergence behavior of these experiments visualized. A selection is shown in Figures 5.16 to 5.21, the rest is shown in Appendix B.

From the single Zernike experiments `5_1` and `6_4` in Figure 5.16 and Figure 5.17 it can be seen that the two reconstruction methods both perform similarly well. When enough powers are fit, both methods estimate the coefficient accurately.

For the 3 random Zernike experiments `3_zerns_1` and `3_zerns_3` in Figure 5.18 and Figure 5.19 it can also be seen that the "initial guesses" (that is the coefficient determined with the least amount of fitting powers possible) of the coefficients are accurate, and don't change drastically if more Zernike powers are fit. The coefficients seem to be able to be measured independently from each other, and there is no difference between the least-squares method and Janssen's method. This is as expected from the theory.

However, looking at the subsequent Zernike experiments `sub_zerns_1` and `sub_zerns_3` a difference can be seen between the two reconstruction methods. The initial guesses of the least-squares method over- or under-estimates the presence of the aberration when not enough powers are fit. From Figure 5.20 it can be seen that defocus is overestimated more than 50% until 4 powers are fit. At 4 fitting powers, the spherical aberration coefficient a_4^0 is overestimated. All values seem to be within normal range at 8 powers fit. The same can be seen in Figure 5.21, where the coefficient a_3^3 is overestimated at 3 and 4 fitting powers. Janssen's method does not present this over-estimation.

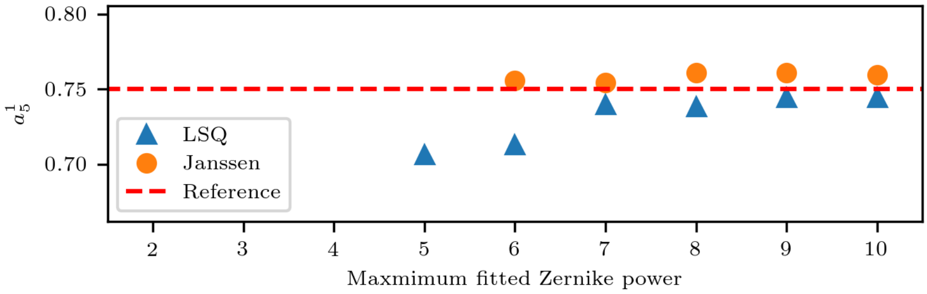

Figure 5.16: Convergence of coefficients for the `5_1` experiment.

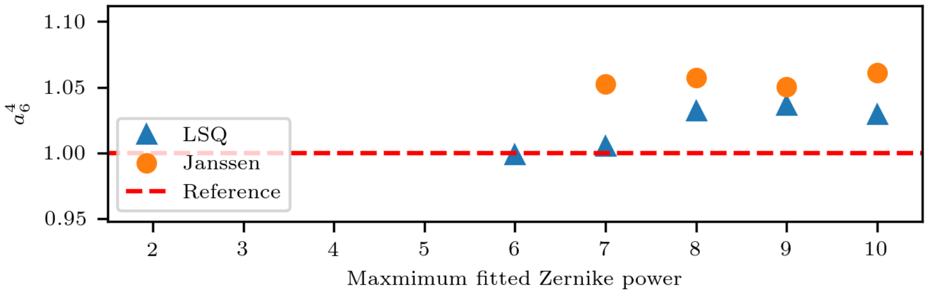

Figure 5.17: Convergence of coefficients for the `6_4` experiment.

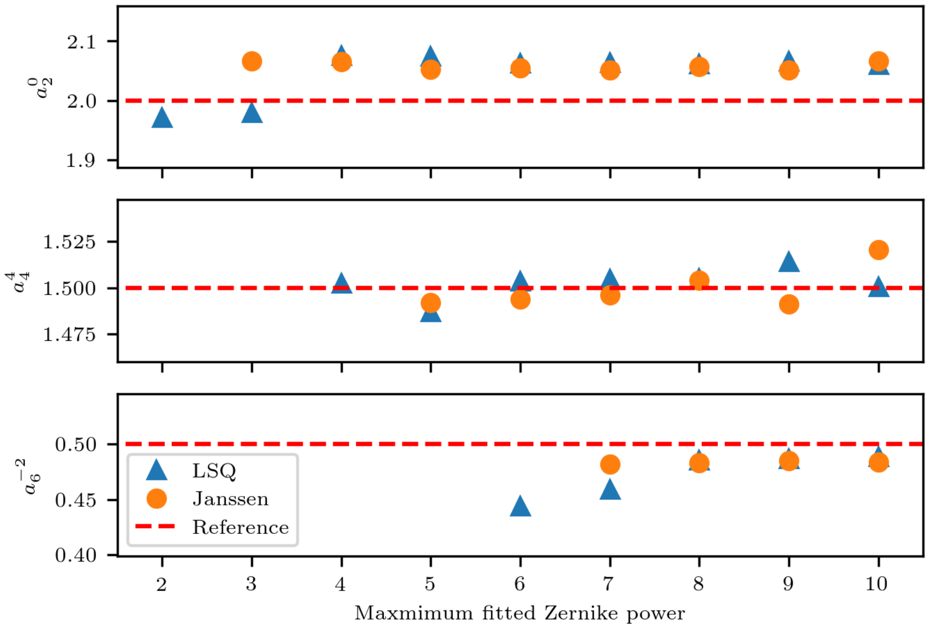

Figure 5.18: Convergence of coefficients for the `3_zerns_1` experiment.

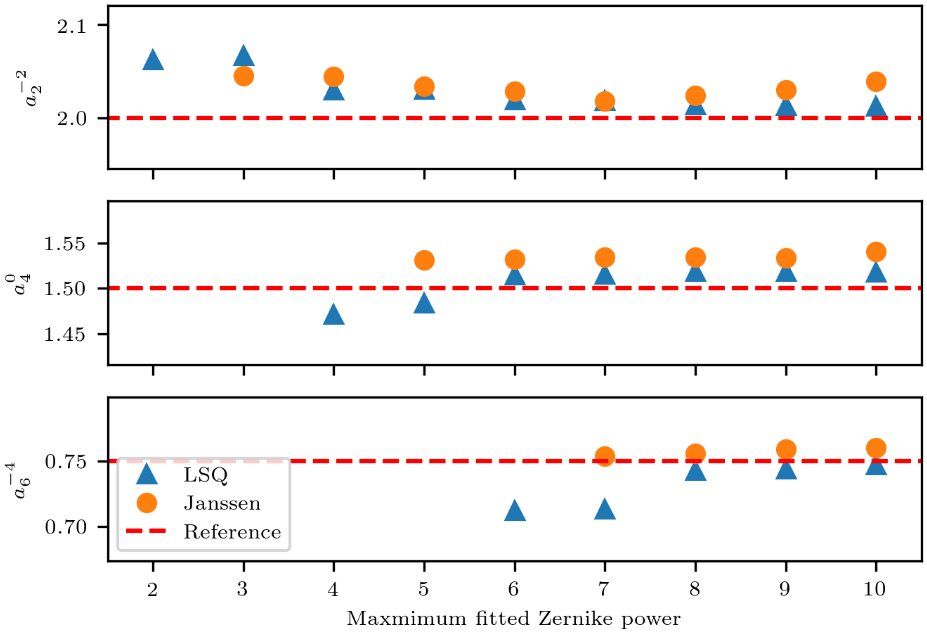

Figure 5.19: Convergence of coefficients for the `3_zerns_3` experiment.

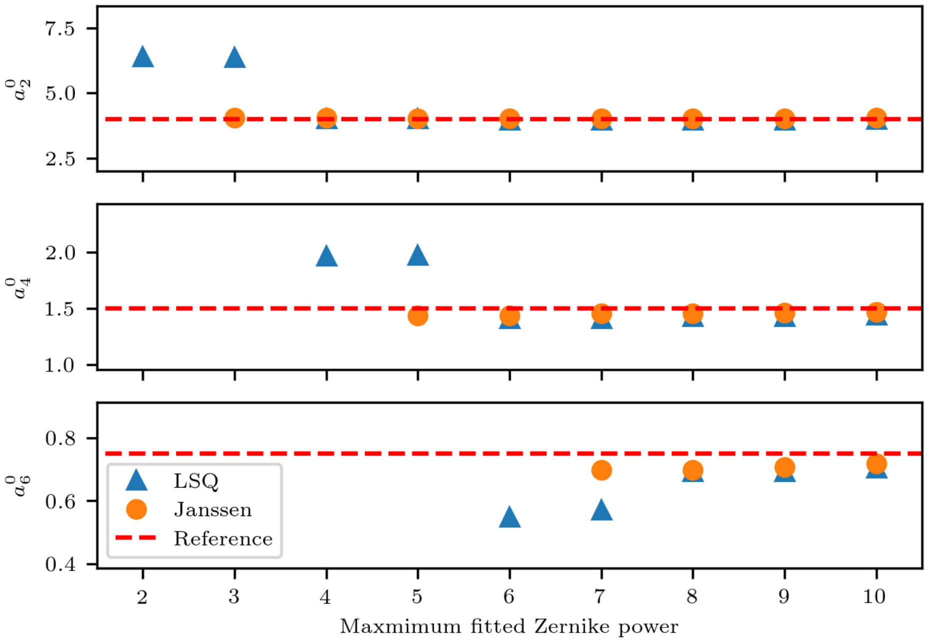

Figure 5.20: Convergence of coefficients for the `sub_zerns_1` experiment.

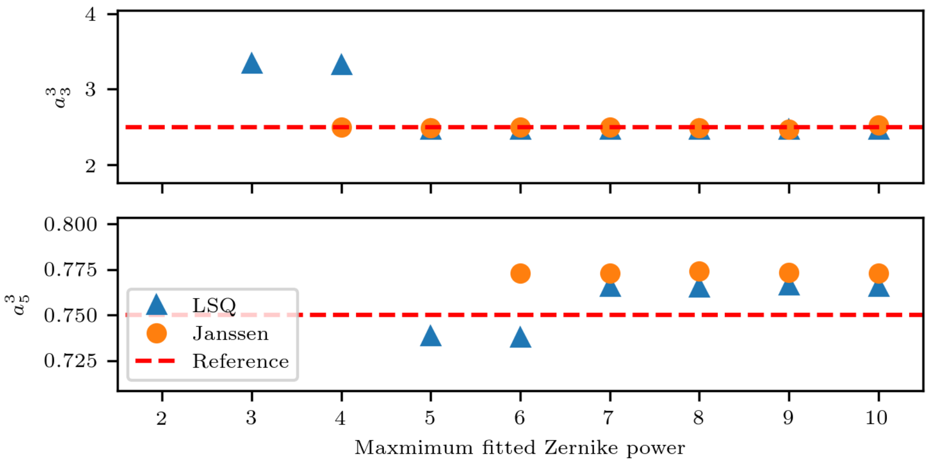

Figure 5.21: Convergence of coefficients for the `sub_zerns_3` experiment.

5.2.2 Least-squares method has a bigger spread between the determined and added aberration coefficient

This cross-talk between two aberrations can be further exemplified by looking at the difference between the estimated coefficients $\hat{a}_n^m$ and the reference coefficient a_n^m given a fitting power k. A new notation $(\hat{a}_n^m)_k$ is introduced, meaning the estimated coefficient $\hat{a}_n^m$ using k fitting powers. The goal is to determine the minimum fitting power k for which Janssen's method and the least-squares method provide an accurate estimation $\hat{a}_n^m$.

To do this, the fitting power has been varied from 3 to 9, looking at $\log_{10}|a_n^m - (\hat{a}_n^m)_k|$ for $k = n+1$, $n+2$ and $n+3$. For example, the accuracy of estimating $\hat{a}_2^0$ is determined for fitting powers $k = 3$, 4 and 5. This accuracy is shown in a notched boxplot. In other words, the data set $n+1$ contains all values of $\log_{10}|a_n^m - (\hat{a}_n^m)_{n+1}|$ varying n from 2 to 8. For the $n+2$ dataset, the fitting powers are varied from 2 to 7 in order to prevent taking aliasing into account. The effects of aliasing on the accuracy of the fits can be seen in Section 5.3.

An annotated example of a notched boxplot is shown in Figure 5.22. A boxplot shows how the data is distributed by showing the quartiles. For instance, the first quartile is the value of the data at exactly a quarter of the "length" of the data, i.e. the $^{n}/_{4}{}^{\text{th}}$ entry if the total data has n entries. The first and the third quartile Q_1 and Q_3 are the outsides of the box, and the line in the middle is the median. The whiskers show the distribution of data outside of the Inner Quartile Range (IQR, $Q_3 - Q_1$). In these boxplots, the whiskers are positioned at $Q_1 - 1.5\text{IQR}$ and $Q_3 + 1.5\text{IQR}$. The outliers are data points that lie either below $Q_1 - 1.5\text{IQR}$ or above $Q_3 + 1.5\text{IQR}$. These points are taken into account for the determination of the median and the quartiles.

The notched boxplot is chosen to represent the data because next to showing the distribution of the data, it also can be used as a quick way to informally test if the medians are equal (Chambers, 1983). This can be done because the notch is drawn at the 95% confidence interval of the median, at the positions

$$M \pm 1.57\frac{\mathrm{IQR}}{\sqrt{n}}, \tag{5.1}$$

where M is the median, IQR the interquartile range and n the amount of measurements.

Boxplots are made for all three experiments, the specific Zernike experiment in Figure 5.23, the lens aberration experiment in Figure 5.24 and the random phase aberration experiment in Figure 5.25. These boxplots are shown in logarithmic scale. As recommended in Cox et al. (2013), the median and quartiles are determined using the logarithm of the data, rather than the raw data itself.

From these boxplots it becomes apparent that Janssen's method is better at estimating the Zernike coefficients using $n+1$ Zernike powers. In all three experiments one can see that the median Janssen's method is lower than the median of the least-squares method because the notches don't overlap. The least-squares method also has the upper whisker higher in all experiments, making it significantly worse than Janssen's method.

However, when fitting $n+2$ and $n+3$ Zernike powers, the difference between the two methods fades. For all three experiments the notches overlap and the distribution shapes are very similar.

A statistical test can be done to see whether or not both distributions are drawn from the same (continuous) distribution, namely the Kolmogorov-Smirnov test. Using `python`, this test can be done by comparing the datasets of errors from Janssen's method and the least-squares method, and a double sided p-value is returned. An overview of these p-values can be seen in Table 5.1.

This test confirms the hypothesis that the distributions of errors for fitting $n+1$ powers is very unlikely to be from the same distribution. Fitting more powers, $n+2$ or $n+3$, it is even likely that the errors for the specific Zernikes and random phase aberrations are drawn from the same distribution.

Using this data it can be determined that the least-squares method is equally accurate in estimating the Zernike coefficient a_n^m as Janssen's method if $n+2$ fitting powers or more are used. It should be noted that there is an upper bound to the amount of fitting powers that can be used due to aliasing (Herrmann, 1981).

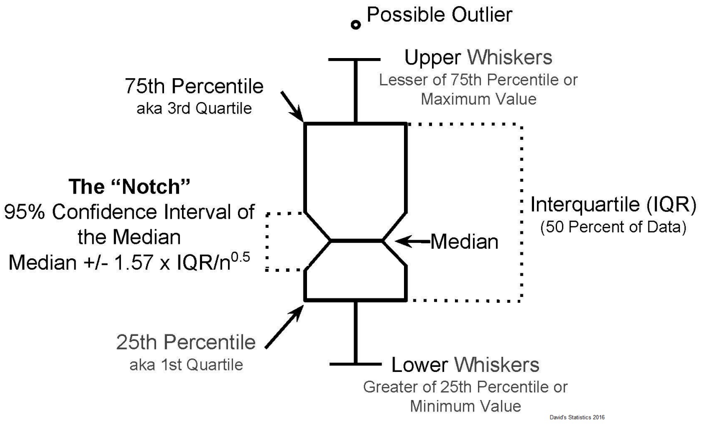

Figure 5.22: An example notched boxplot. Here n is the amount of samples. Adapted from David Doyle (2013)

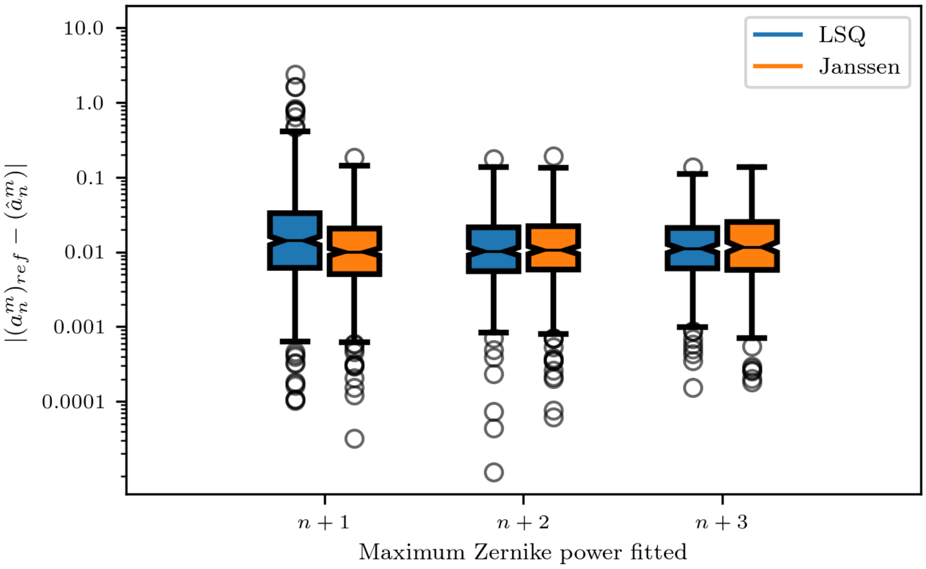

Figure 5.23: Boxplot of the accuracy results of the specific Zernike experiment. Note the logarithmic y-scale.

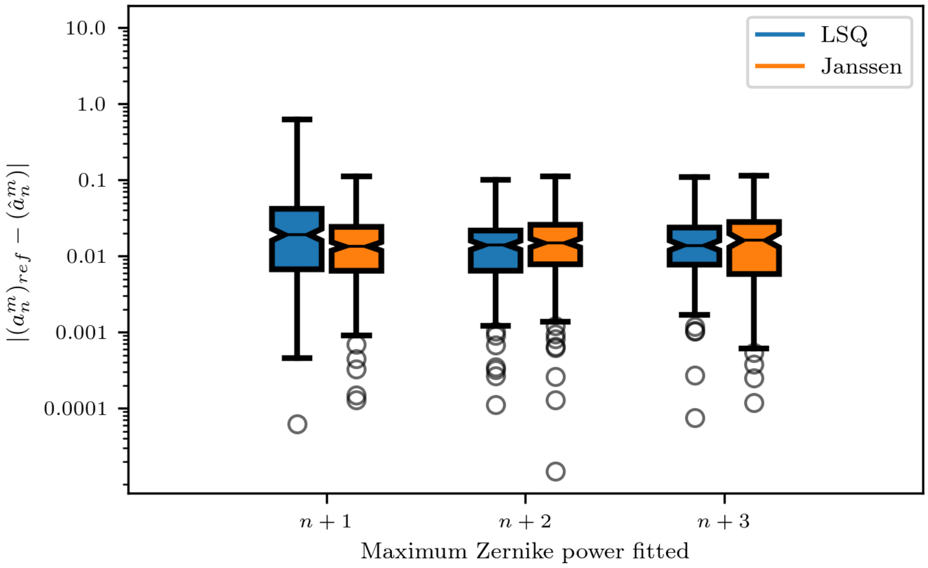

Figure 5.24: Boxplot of the accuracy results of the lens aberration experiment. Note the logarithmic y-scale.

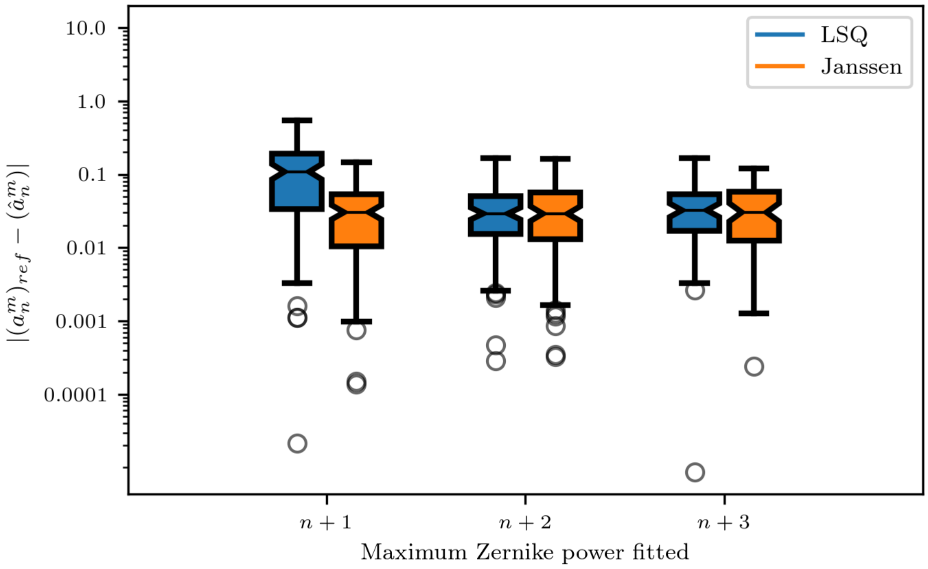

Figure 5.25: Boxplot of the accuracy results of the random phase aberration experiment. Note the logarithmic y-scale.

Table 5.1: The Kolmogorov-Smirnov test double sided p-values for the Hypothesis that both sets are drawn from the same distribution for the values $\log_{10}|a_n^m - (\hat{a}_n^m)_k|$.

power k	Specific Zernikes	Lens aberrations	Random phase aberrations
$n+1$	0.00004	0.00002	0.00000
$n+2$	0.77624	0.13240	0.96102
$n+3$	0.49903	0.31827	0.95609

5.3 Both methods experience aliasing when fitting more Zernike powers

It has been shown that the optimal amount of Zernike powers to be fit is 8 in the current research. It is known from the least-squares method that the quality of reconstruction gets worse when too many Zernikes are fit due to aberration aliasing (Herrmann, 1981). Aberration aliasing stems from the fact that higher order aberrations become indistinguishable from lower order aberrations due to the fact that the values in the geometry matrix are evaluated on a finite mesh. Aberration aliasing is different from the cross-talk previously discussed because aberration aliasing does not stem from from non-orthogonal columns. Due to the fact that the aberration aliasing does not stem from non-orthogonality, both methods are expected to show aberration aliasing.

It is expected that the aberration aliasing is most strongly seen in specific Zernike aberrations case. This is expected because there the added aberrations can all be resolved using the optimal 8 powers. Fitting more powers will therefore not add accuracy. The other two experiments, the lens aberrations and the random phase aberrations, do contain aberrations of higher power than the optimal 8. Therefore it is expected that the RMS error will go down even if more than 8 powers are fit. However, a limit is expected where the aliasing will have stronger effects than the reduction of RMS by estimating more powers.

In the following graphs, one can see the RMS error when fitting 5 to 14 Zernike powers using the center position and radius as defined in Section 4.3. This is shown for all experiments.

Figure 5.26 shows the convergence and subsequent divergence of the RMS error for the specific Zernike reconstructions without aberrations that introduce cross-talk. The subfigures show the trends of convergence and divergence of the RMS error ε on a bigger scale, while the inset graphs show the RMS error around its minimum value. From the inset graphs, it can be seen that the RMS error is higher at 9 and 10 Zernike powers fit than at 8 Zernike powers, except for Janssen's method in the experiments `5_1` and `3_zerns_1`, where the fit with 9 Zernike powers resulted in a lower RMS value than at 8 Zernike powers. This is in accordance with the hypothesis that the RMS value increases when increasing the Zernike powers for fitting without any aberration of higher power being present.

What also can be seen from the same graph is the fact that Janssen's method tends to diverge earlier and faster the least-squares method. The RMS error at 11 Zernike powers fitted is significantly higher for Janssen's method than for the least-squares method, with the exception of the experiment `3_zerns_3`.

In Figure 5.27, the convergence and divergence behavior of the RMS of all experiments which *do* introduce cross-talk are shown. In these graphs, Janssen's method shows the same trend as in the experiments where there was no cross-talk present, namely that the RMS value increases with increased Zernike powers fit. Also, the Zernike fitting power at which Janssen's method diverges is again lower than when the least-squares method diverges.

However, the least-squares method shows a different characteristic. Even though in the experiment `sub_zerns_1`, Zernike aberrations up to the 6$^{\text{th}}$ power were present, the RMS value declines when increasing the fitting powers from 6 to 10. This is in accordance with the conversion of the coefficients themselves, seen in Figure 5.20. There it can be seen that when increasing the fitting powers, the least-squares method more accurately estimates the coefficients present. Also, the lowest RMS error of the least-squares method at any fitting power is not lower than the lowest RMS error of Janssen's method.

Figure 5.28 shows the RMS errors for the lens aberrations. In these aberrations, aberrations are present up to the tenth Zernike power, and combinations of aberrations are present that produce cross-talk. It can be seen from the inset graphs that in most cases, the minimum RMS error is seen in the least-squares case when fitting 10 Zernike powers. The exceptions for this are `366_03` and `544_04`. For Janssen's method, the minimum value of the RMS error is seen when fitting 9 Zernike powers, with the exceptions of `366_03` and `544_33`. Only in the last case is the minimum RMS error found with more fitting powers than 9. At either 8 or 9 fitting powers (dependent on the experiment) the RMS error of Janssen's method and of the least-squares method is comparable. These graphs show again that Janssen's method diverges with less fitting powers than the least-squares method, as Janssen's method diverges either at 11 or 12 fits, while the least-squares method diverges at 12 or 13 fits.

Figure 5.29 shows the RMS errors for different Zernike fitting powers for the random phase measurements. These random phases also contain up to 10 powers of Zernike aberrations (with the exception of `low`) and cross-talk is possible. For the least-squares method it can be seen that the lowest RMS value is found when fitting up to 11 Zernike powers (again with the exception of `low`). Janssen's method also shows a steady decline in RMS error fitting up to 11 Zernike powers for `medium` and `high`, while the minimum RMS

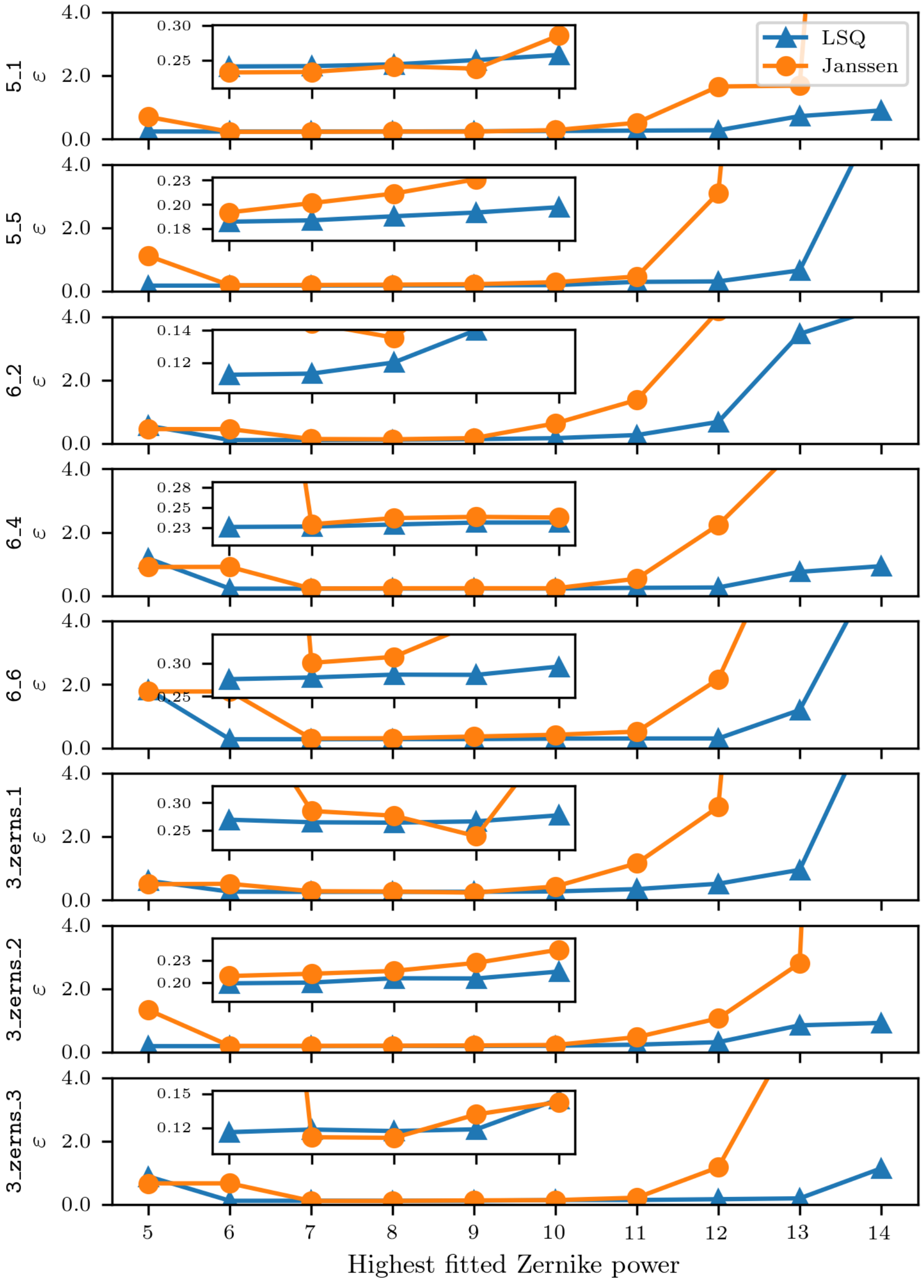

Figure 5.26: The RMS error of the reconstructions of the first eight specific Zernike cases for different amount of fitted Zernike powers

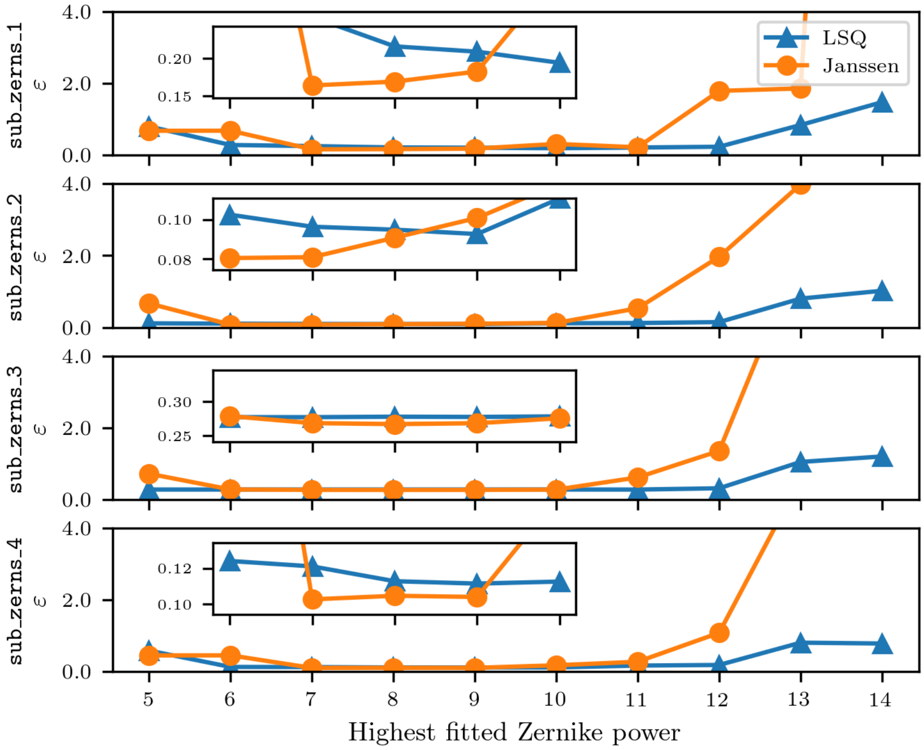

Figure 5.27: The RMS error of the reconstructions of the four specific Zernike cases for which cross-talk is present, shown for different amount of fitted Zernike powers

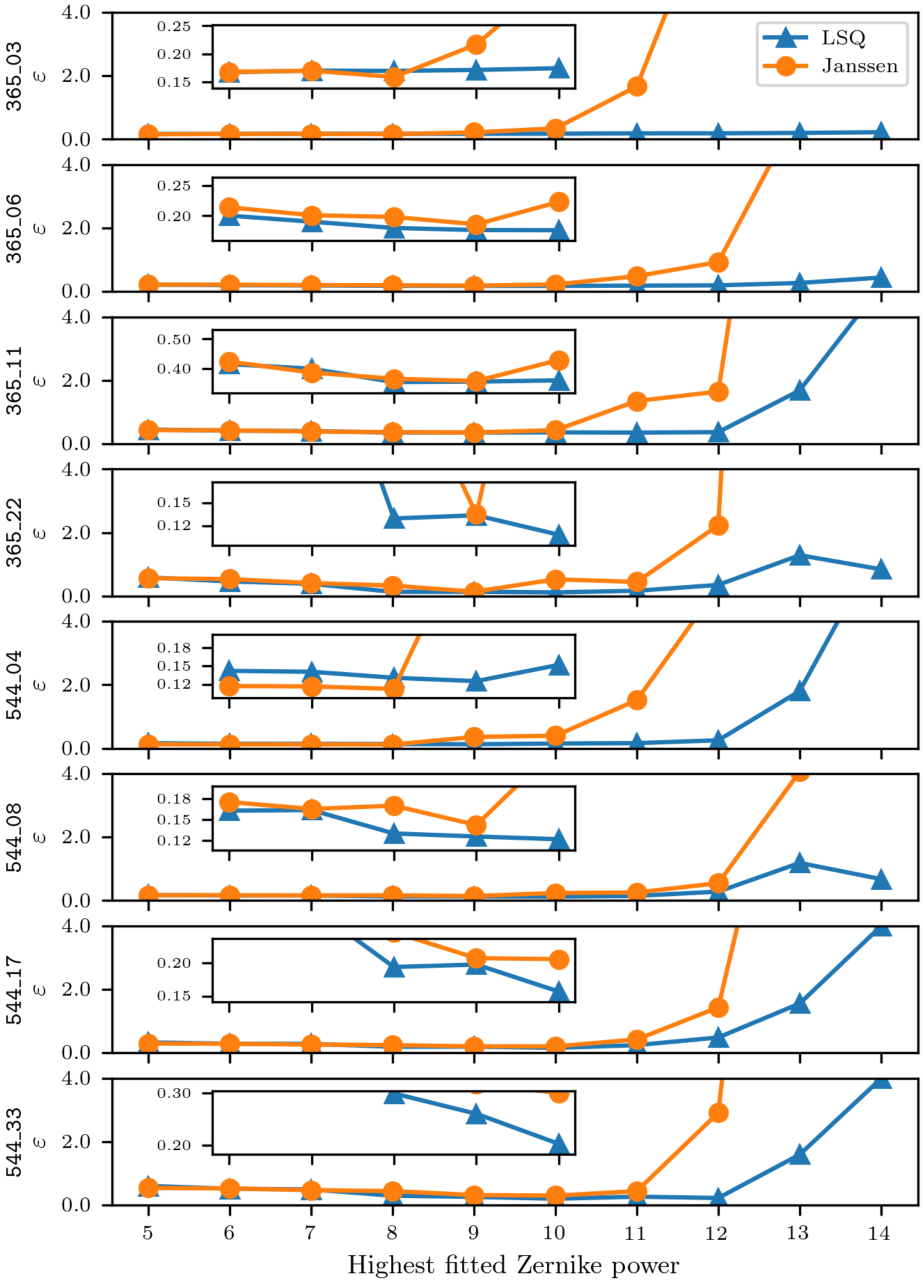

Figure 5.28: The RMS error of the reconstructions of the lens aberrations for different amount of fitted Zernike powers

error is reached with 9 fitting powers for `low` and at 10 fitting powers for `extreme`. In these experiments, only in the `high` experiment does Janssen's method estimate with similar accuracy as the leas-squares method. As is the case with the other experiments, at 12 Zernike powers fit Janssen's method has a significantly higher RMS error than the least-squares method.

What can be seen from all these experiments is that Janssen's method diverges with fewer fitted Zernike powers than the least-squares method. For the lens aberrations and the random phase aberrations, with up to 10 Zernike powers of aberrations present, this means that the least-squares method performs better than Janssen's method.

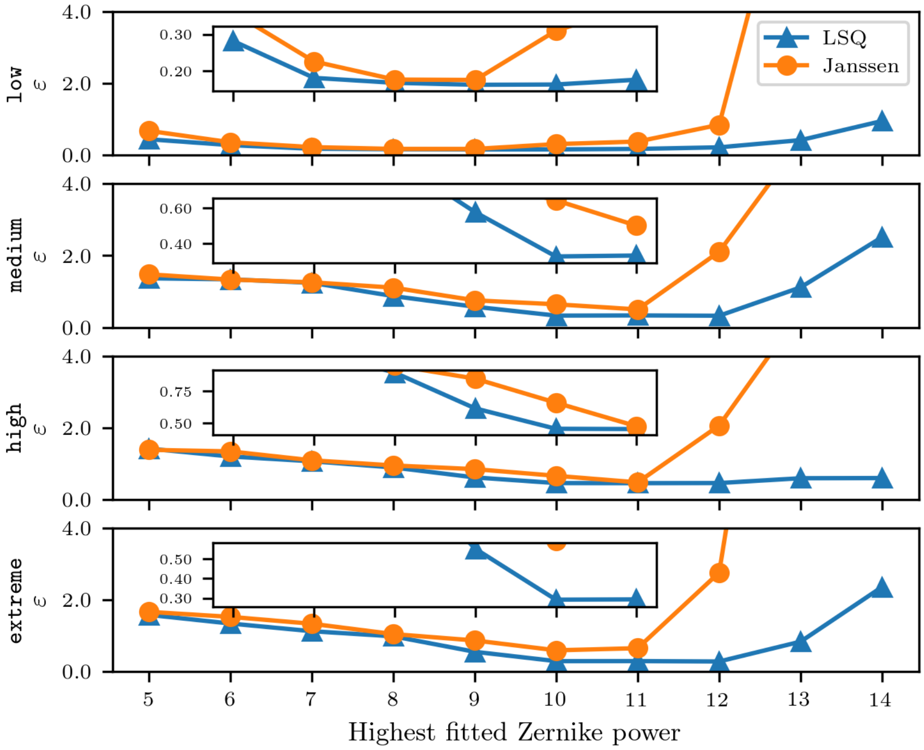

Figure 5.29: The RMS error of the reconstructions of the four random phase aberrations for different amount of fitted Zernike powers

5.4 Error landscape with respect to center position and radius is equally sharp

As was stated in Section 4.3, finding the optimal center position and radius takes a long time compared to calculating the coefficients with a known geometry matrix. Due to physical misalignment, this center position can change over time. In order to compare the two methods on the influence of mis-estimating the center position or radius, the RMS error landscape is calculated. The method for calculation has been described in Section 4.3.

A selection from each of the three experiments has been shown in Figures 5.30 to 5.35. The other results are shown in appendix D.

Figure 5.30 shows the RMS error landscape of the first four single Zernike experiments. It can be seen that for all cases, the general shape of the surface through the medians and the whisker height for all datapoints are comparable. The scale difference between for instance `5_5` and `6_2` is significant, but within the same measurement, the RMS landscapes seem the same.

This is, however, not exactly the case for Figure 5.31. For `365_03` and `365_06` it can be seen that reducing the radius change Δr drastically changes the RMS error for the least-squares case. Janssen's method shows the same effect but less drastically for the `365_03` case. This abnormality in the error landscape indicates that something has gone wrong during the optimization of the center and radius. In fact, when looking at the Shack-Hartmann pattern, center position and radius are shown in Figure 5.32, it can be seen that for `365_03` and `365_06`, the center and radius are mis-estimated grossly. With such a small radius and presented for the least-squares case with `365_03`, information from the spots outside of the radius are lost. When Δr becomes negative, even more spots will be lost, hence the sharp increase in RMS error. A possible reason for this error in parameter estimation is the fact that the aberration is very small, with small coefficients and a small peak-to-valley value. A possible solution to this problem is proposed in Section 7. It can be seen that for the second four experiments of the lens aberrations, the RMS landscape (presented in Figure 5.33) and the center and radius position (Figure 5.34) seem to be found well.

Also the error landscape of the random phase experiments, shown in 5.35, seems to behave like the specific Zernike experiment and the second four experiments of the lens aberration experiments. From these well behaved RMS landscapes, it can be seen that for all experiments, there are no major differences between the least-squares method and Janssen's method. Therefore, they will both be equally sensitive to errors caused by the mis-estimation of the center and radius parameters. All other experiments and all center and radius positions can be found in appendix.

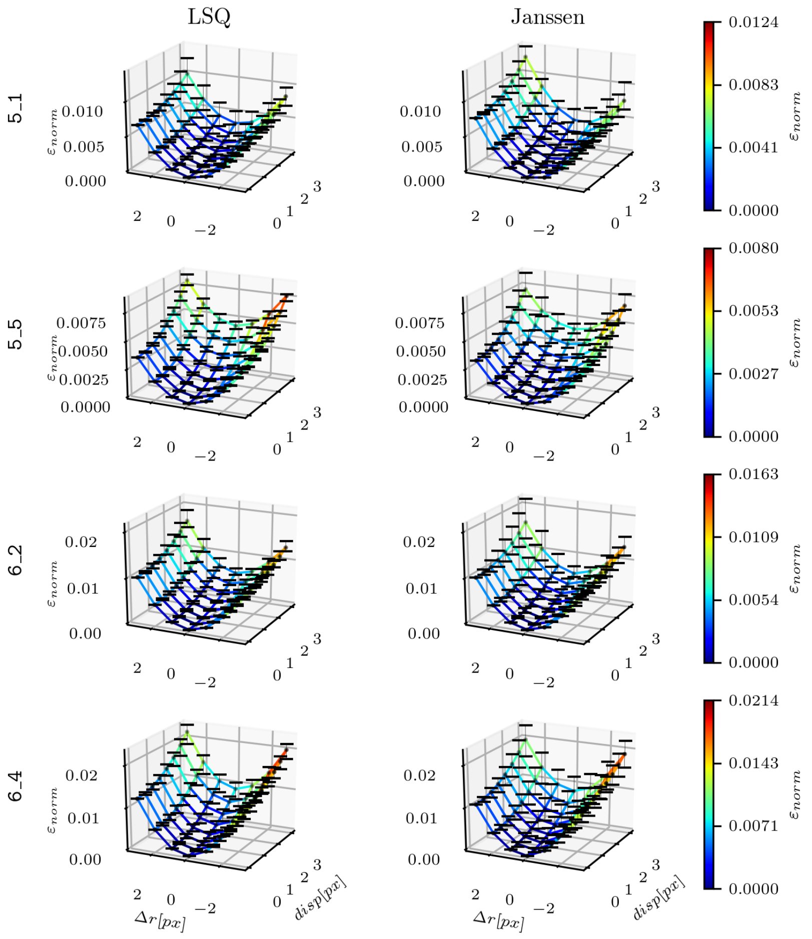

Figure 5.30: The RMS error landscape for the first four specific Zernike experiments. The surface is plot through the median of the values at each points of $(disp, \Delta r)$. The whiskers denote the maximum and minimum value of the values at those points.

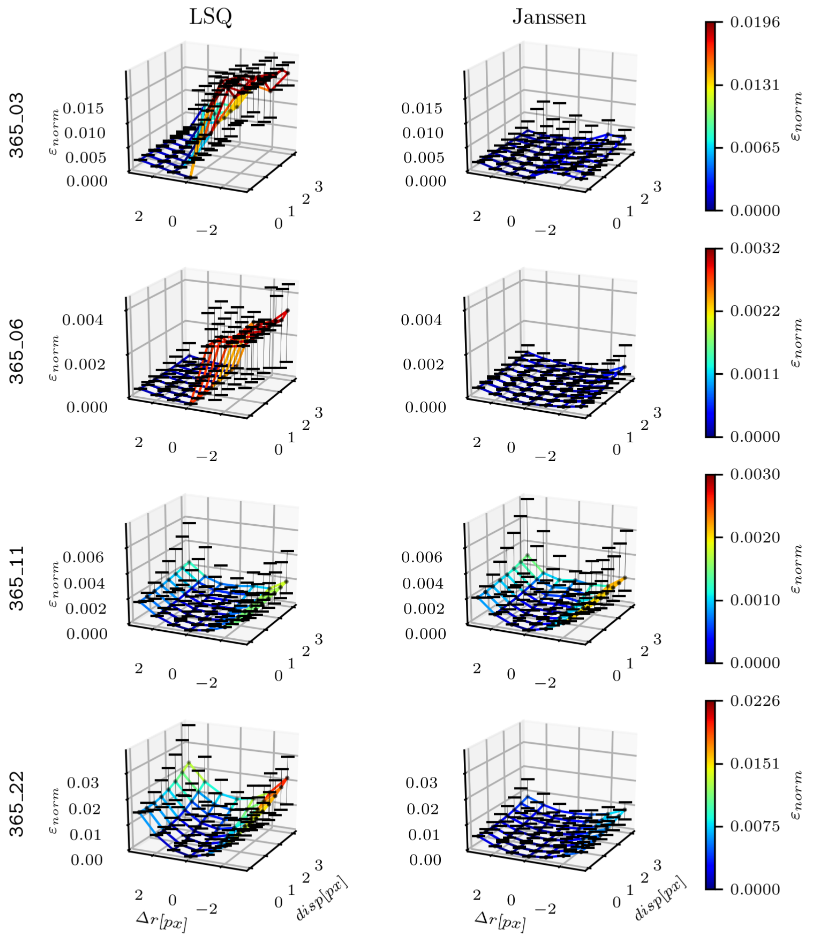

Figure 5.31: The RMS error landscape for the first four lens aberration experiments. The surface is plot through the median of the values at each points of $(disp, \Delta r)$. The whiskers denote the maximum and minimum value of the values at those points.

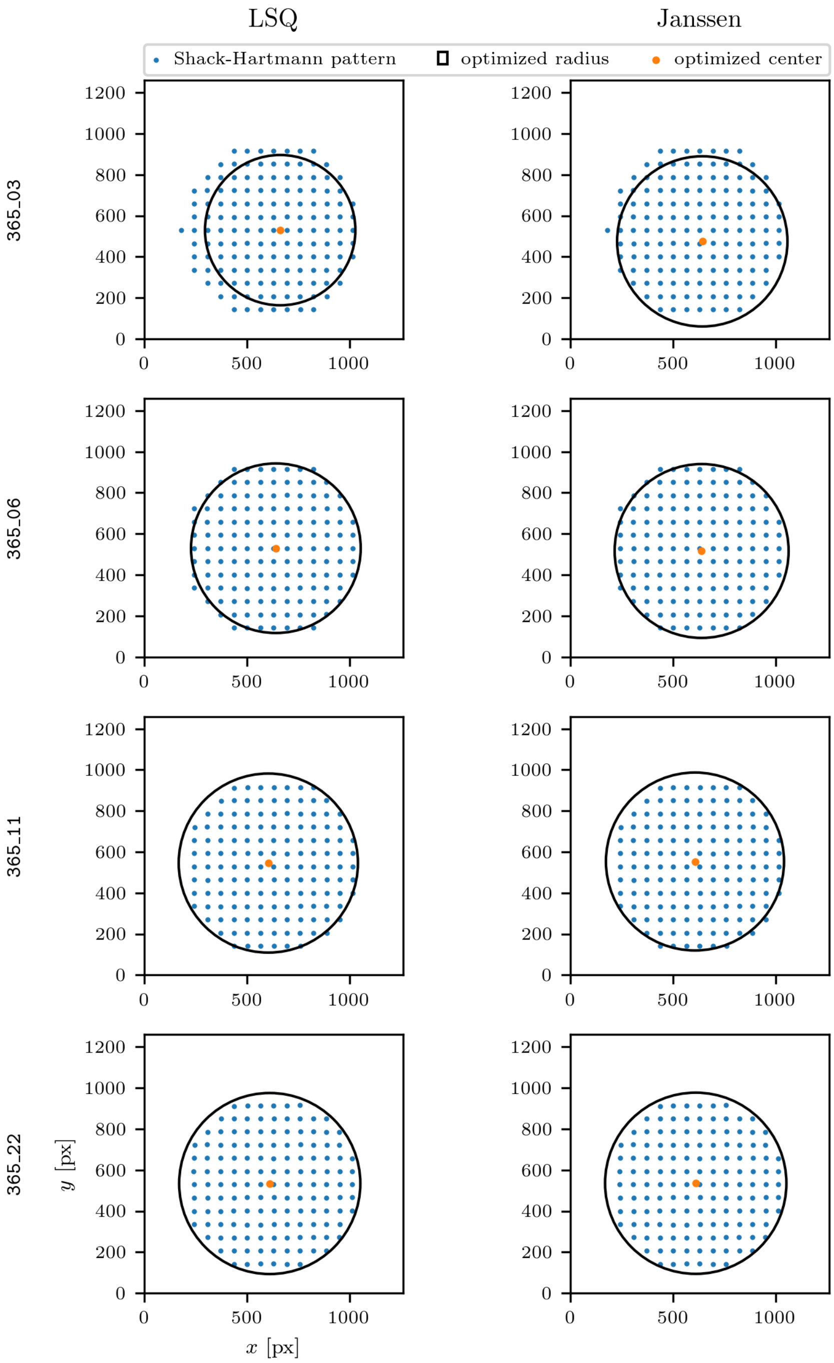

Figure 5.32: The Shack-Hartmann pattern and estimated centers and radii for the first four Lens aberration experiments.

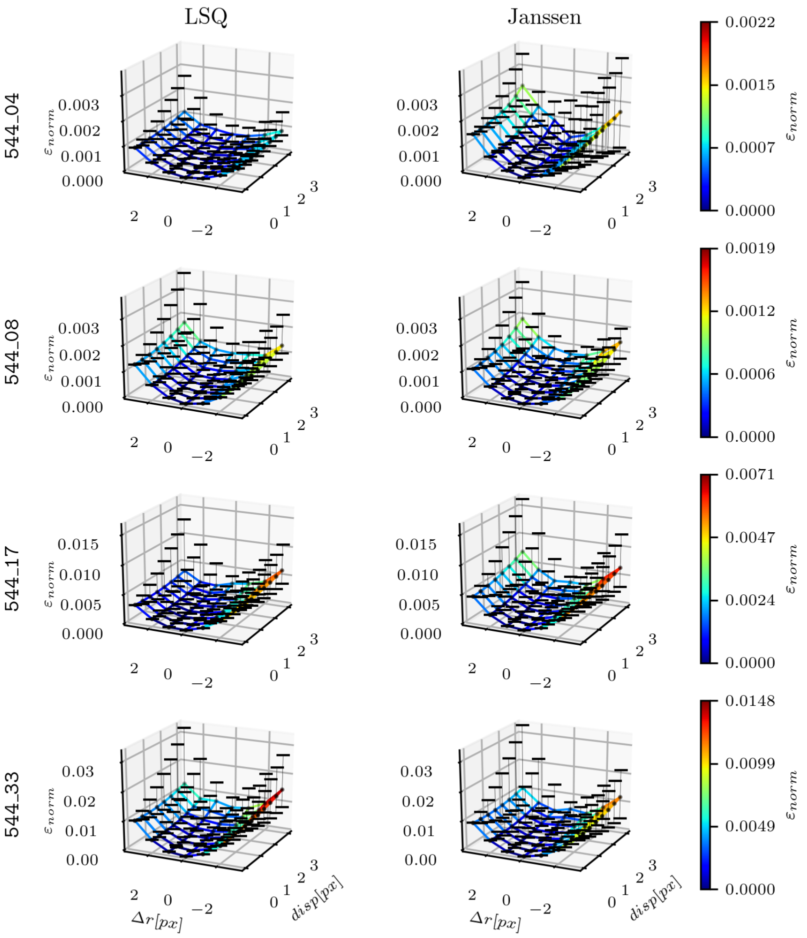

Figure 5.33: The RMS error landscape for the second four lens aberration experiments. The surface is plot through the median of the values at each points of $(disp, \Delta r)$. The whiskers denote the maximum and minimum value of the values at those points.

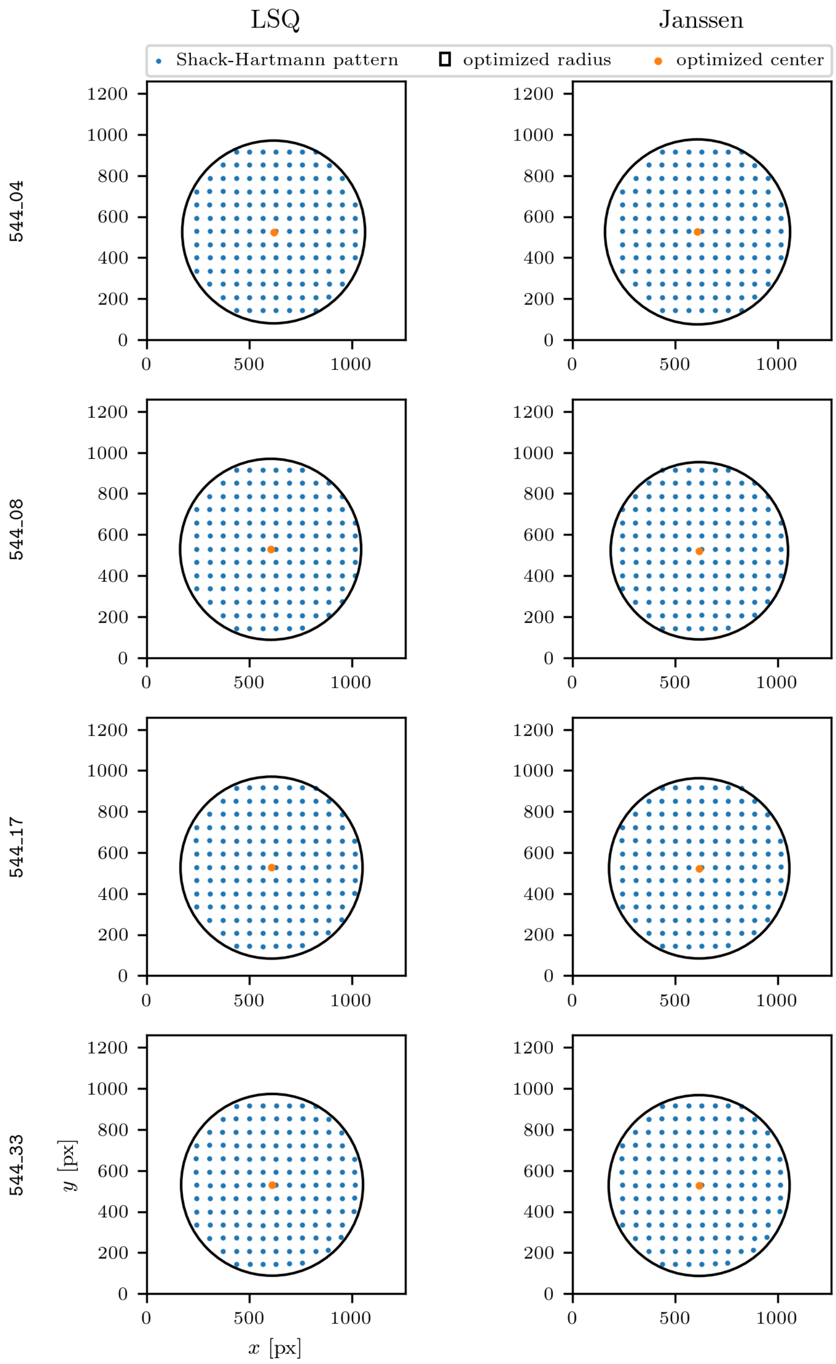

Figure 5.34: The Shack-Hartmann pattern and estimated centers and radii for the second four Lens aberration experiments.

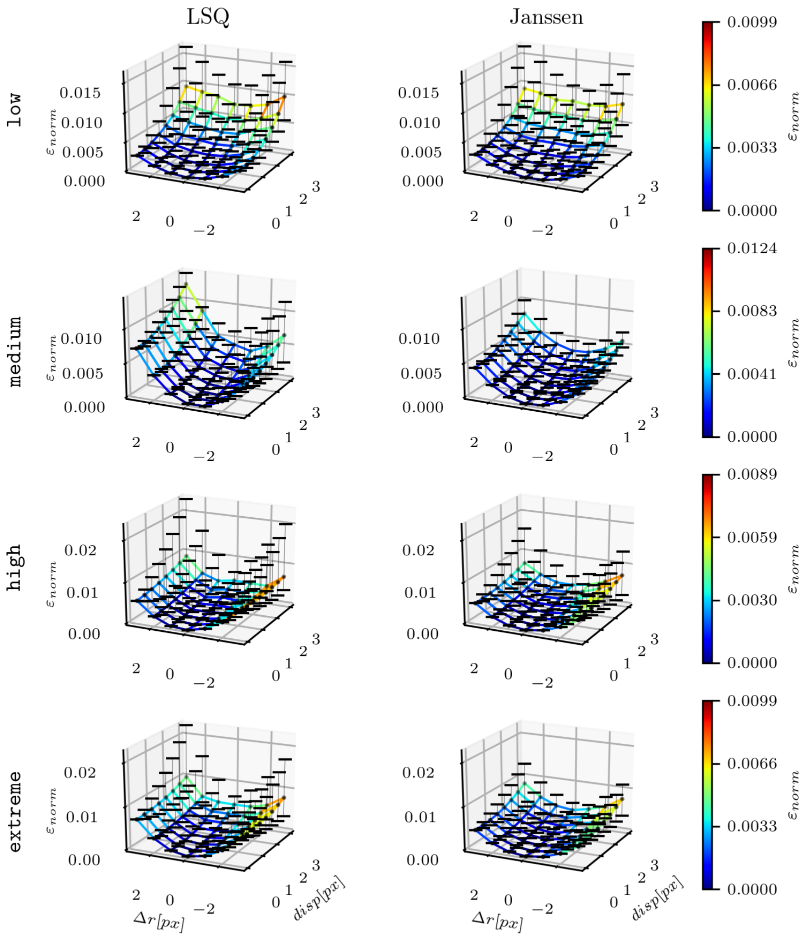

Figure 5.35: The RMS error landscape for the random phase aberration experiments. The surface is plot through the median of the values at each points of $(disp, \Delta r)$. The whiskers denote the maximum and minimum value of the values at those points.

5.5 Janssen's method is at least 3.5 times slower due to using complex numbers

Due to using complex numbers, Janssen's method will be at least 3.5 times slower than the least-squares method at calculating their respective coefficients. In this section the computational complexity of calculating either the complex or real Zernike coefficients using Janssen's method and the LSQ method is determined. This is done comparing the complexity of the algorithm using N Zernike fitting powers and using Y spots on the Shack-Hartmann camera. Also assumed is that the geometry matrix and vector containing the slopes are pre-computed, and that the cost of addition, subtraction, multiplication and division are all equal. The computational cost of the least-squares method is shown in the paragraph below, and the cost Janssen's method is detailed in Table 5.2.

If the geometry matrix and slopes vector are pre-computed, the least-squares method only requires a matrix-vector product to gather the coefficients. This geometry matrix, as described in Equation 2.34 has a size of $J(N) \times 2Y$. Here, $J(N)$ is the total amount of Zernike modes in the first N powers, and is expressed as

$$J(N) = \frac{(N+1)(N+2)}{2}. \tag{5.2}$$

From linear algebra, one can see that to compute a matrix-vector multiplication of a $p \times n$ matrix with a vector of length n, one needs pn multiplications and $p(n-1)$ additions. The total computational cost would therefore be $2pn - p$, which can be simplified to $2pn$ when $p, n \gg 1$. The total computational cost of the least-squares matrix vector multiplication would therefore be $\mathcal{O}(4J(N)Y) = \mathcal{O}(2Y(N+1)(N+2))$.

In order for Janssen's method to find the first $N-1$ powers, one needs to find β_+ and $\beta_- \in \mathbb{C}^{J(N)}$ (i.e. using the first N Zernike modes for fitting). The slopes vector for Janssen's method is only Y long, as opposed to $2Y$ of the least-squares method. Therefore the geometry matrix for Janssen's method will be in $\mathbb{C}^{(J(N)\times Y)}$. However, the matrix-vector product has to be done twice.

Also, due to the complex nature of the geometry matrix and the vector containing the slopes, one has to account for the added complexity of the matrix vector product. When adding two complex numbers, $z = x + iy$ and $z' = x' + iy'$ for instance, one can see that the addition can be done using 2 real additions, $x + x'$ and $y + y'$. Therefore, complex addition is twice as computationally expensive as real addition.

A similar derivation can be made for complex multiplication. Multiplying z and z' can be written as

$$zz' = (xx' - yy') + i(xy' + x'y). \tag{5.3}$$

To compute the complex multiplication, one has to do 4 real multiplications and 2 additions. Assuming multiplication and addition are equally computationally expensive, the cost of complex multiplication is 6 times higher than real multiplication or addition.

Extending this multiplication to a matrix-vector product, it was shown above that a matrix vector product costs pn multiplications and $p(n-1)$ additions. If both the matrix and vector contain complex values (which in the case of Janssen's method it does), the computational cost of this matrix-vector product can be done in $4pn$ real multiplications and $4pn - 2p$ real additions. If p and n are both much bigger than one, the approximate cost of this matrix-vector product is $\mathcal{O}(8pn)$. If one implements a smarter algorithm than direct computation, one can lower this to a computational cost of $\mathcal{O}(7pn)$ (Fam, 1988).

The evaluation of $\delta_{n|m|}$ is taken to be the same cost as 2 real multiplications, because n and m are real numbers.

Table 5.2: Computational steps and their complexity in calculating complex Zernike coefficients using Janssen's method.

Action	Operations	Complexity
Gather β_+ and β_-	2 mat-vec	$\mathcal{O}(14J(N)Y)$
calculate φ_n^m	2 multiplications	$\mathcal{O}(12J(N))$
	1 addition	$\mathcal{O}(2J(N))$
calculate c_n^m	evaluate $\delta_{n\|m\|}$	$\mathcal{O}(2J(N))$
	1 addition	$\mathcal{O}(2J(N))$
	1 division	$\mathcal{O}(6J(N))$
calculate α_n^m	2 multiplications	$\mathcal{O}(12J(N))$
	1 subtraction	$\mathcal{O}(2J(N))$
Total		$\mathcal{O}(14J(N)Y + 38J(N))$

All steps of Janssen's method and their complexity are shown in Table 5.2.

Substituting $J(N)$ gives us the the computational cost of Janssen's method in terms of N and Y, which is $\mathcal{O}((7Y + 19)(N + 1)(N + 2))$. If Y is big enough, this can be simplified to $\mathcal{O}(7Y(N + 1)(N + 2))$.

Comparing this result to the cost of the least-squares method ($\mathcal{O}(2Y(N+1)(N + 2))$), one sees that in the scenario of high Zernike power fitting and high amount of spots, Janssen's method is 3.5 times slower than the least-squares method. If a lower spot count or lower Zernike power fitting is used, Janssen's method will be more than 3.5 times slower than the least-squares counterpart. At 6 spots it is approximately 5 times slower, and at 19 spots it is exactly 4 times slower.

6 Conclusion

In conclusion, in order to compare Janssen's method to the least-squares method for reconstructing the wavefront using a Shack-Hartmann sensor, three sets of aberrations have been reconstructed. For both methods and all aberrations, four tests were done to compare the methods. In the first test, the quality of the reconstruction has been determined by fitting the optimal amount of Zernike aberrations. Afterwards, less than optimal Zernikes powers have been fitted to evaluate the effects of cross-talk for both methods. Furthermore, too many Zernike aberrations were fitted in order to see the effects of aliasing. Lastly, the error landscape was determined for all aberrations and both methods. Apart from this, the theoretical computational cost was has been determined.

The first test to see the quality of the reconstruction with optimal amount of Zernike fits shows that the quality of the fit is in general similar for the least-squares method and Janssen's method. It is shown that for the cases with the specific Zernike aberrations and the lens aberrations, the RMS error between the reconstruction and the reference phase is similar. The RMS error was significantly higher for Janssen's method in the case of random aberrations, but that was due to the fact that less coefficients were estimated.

When less than the optimal Zernike powers were fit, it was shown that Janssen's method estimates the coefficients more accurately. For the single Zernike aberration case it was shown that only the least-squares method shows cross-coupling of higher order aberrations, while Janssen's method does not. For all three sets of aberrations it was shown that using $n+1$ fits, the coefficients a_n^m were more accurately estimated by Janssen's method than by the least-squares method. This difference in accuracy disappeared once $n+2$ fits were made.

When more than the optimal Zernike powers were fit, it was shown that both methods suffer from aliasing. It was shown that even though the general shape of the convergence and divergence of the error with increasing amount of aberration fits were the same, Janssen's method tends to diverge more rapidly. The divergence of Janssen's method started at fewer fitting powers, 11 fitting powers as opposed to the least-squares 12 or 13.

The error landscape was shown the be very similar for both methods. Janssens's method and the least-squares method showed both a similar behavior when varying either the center position or radius of the beam on the Shack-Hartmann sensor. This makes them equally sensitive to errors caused by the mis-estimation of these parameters.

Theoretically, it was assessed what the computational intensity of both reconstruction algorithms was. It was shown that due to the fact that the calculations in Janssen's method are done in the complex plane, the method is at least 3.5 times slower than the least-squares method. Janssen's method will be even slower in cases when there are relatively little spots. At 6 spots, the method is approximately 5 times slower and at 19 spots the method is 4 times slower.

All in all, it is shown that the initial hypothesis of the lack of cross-talk in Janssen's method holds up also in experiments. Further research shows the pros and cons of both methods. Depending on the needs of the system in which the algorithm is used, both methods are good candidates for recovering the wavefront using a Shack-Hartmann sensor.

7 Recommendations

In order to even better understand the performance difference between the Janssen's method and the least-squares method when doing wavefront reconstruction, three additional experiments can be done. A solution for the mis-estimation of the center and radius parameters is first proposed.

First of all, it is recommended that the optimization algorithm for finding the center and radius is revisited. For the `365_03` and `365_06` experiment, this algorithm seems to have found local minima, rather than the global minimum. It is expected this local minimum was found because of the small aberration that was introduced in these experiments. It can be seen that in the experiments that did behave well, the center position and radius do not differ that much. A good check to see if a global minimum is reached is the fact that both methods find a similar minimum, and that the center position and radius are close to the initial estimates. For this, the bounds for the center position and radius can be set smaller in the initial L-BFGS-B optimization.

Second of all, an improvement can be made by using a different SLM. In the current research, a Holoeye PLUTO SLM is used to add aberrations to the wavefront. From (Bondareva et al., 2014) it can be seen that there is a significant temporal fluctuation of the phase retardation. A fluctuation of up to 0.13π has been measured when addressing a high phase-retardation to the SLM. Because of this flickering in the phase, the error had to be redefined during the research. The initial error was defined as the difference between the wavefront recovered with interferometry and the wavefront recovered with the Shack-Hartmann sensor. This is because interferometry in general is more accurate at reconstructing the wavefront than reconstruction with the Shack-Hartmann sensor. However, due to the flickering of the SLM, the reconstruction quality was worse and could not be used as a reference. Therefore, re-doing the experiments with a more stable SLM could make wavefront reconstruction with interferometry possible and can provide a better reference phase for better error estimation for both Shack-Hartmann methods.

Also, it would be interesting to repeat the experiments verifying the absence of cross-talk with fewer spots. The absence of cross-talk between certain Zernike aberrations has been proven only in the limit of infinite spots. In Janssen's case, the columns of the geometry matrix will in general not be orthogonal due to the fact that there are a finite amount of spots, and the non-orthogonality will be stronger for fewer spots. It would be interesting to see the effect of this non-orthogonality on the reconstruction quality for Janssen's method.

Furthermore, an interesting experiment can be done using annular pupils. In, for instance, the new European Extremely Large Telescope, the primary mirror collecting all the light is not perfectly round. The mirror consists of

798 hexagonal mirror segments, arranged in an annulus. The aperture will therefore be annular, rather than circular. An interesting research question would be whether or not the same pros and cons of Janssen's method and the least-squares method holds when reconstructing the full wavefront from annular wavefront data. A great benefit for Janssen's method is that there is a mathematical relationship between the measured scaled coefficients $\alpha_n^m(\varepsilon)$, where $\varepsilon \in [0, 1]$ denotes the radius of the central obstruction, and the actual present aberrations α_n^m, as shown in Appendix 2 of Janssen et al. (2008). A relationship between $a_n^m(\varepsilon)$ and a_n^m can be made in a similar fashion from the results presented in Dai (2006).

Acknowledgement

First and foremost I'd like to thank my thesis supervisors Silvania Pereira and Paolo Pozzi. The doors of your offices were always open if I had run in any trouble at the optical table or when I was writing my thesis. Our weekly meetings helped me stay focussed and practical during the whole duration of the research. Your help has made me a better physicist as a result.

Furthermore, I'd like to thank Oleg Soloviev for maintaining the same open door policy even though he was not a supervisor. Sadly, the interferometric measurements did not make the final report, but your help and expertise on this area were greatly appreciated.

Next to that, I want to thank Dmytro and Priya for the unending supply of coffee and conversation between experiments and during writing. My time at the optics department would have been a lot less caffeinated without you.

Finally, I must give the greatest thanks to my parents and to Laura Marino. Without your words of encouragement, wisdom and support, my university career and accomplishments would not have been possible. I am indebted to you for all your love.

References

A. Bondareva, P. Cheremkhin, N. Evtikhiev, V. Krasnov, R. Starikov, and S. Starikov. Measurement of characteristics and phase modulation accuracy increase of lc slm" holoeye pluto vis". In *Journal of Physics: Conference Series*, volume 536, page 012011. IOP Publishing, 2014.

J. Chambers. *Graphical methods for data analysis.* Chapman & Hall statistics series. Wadsworth International Group, 1983. ISBN 9780534980528. URL `https://books.google.nl/books?id=I-tQAAAAMAAJ`.

N. J. Cox et al. Speaking stata: Creating and varying box plots: Correction. *Stata Journal*, 13(2):398–400, 2013.

G.-M. Dai. Scaling zernike expansion coefficients to smaller pupil sizes: a simpler formula. *JOSA A*, 23(3):539–543, 2006.

G.-m. Dai. *Wavefront optics for vision correction*, volume 179. SPIE press Washington, 2008.

David Doyle. Notched box plots, 2013. URL `https://sites.google.com/site/davidsstatistics/home/notched-box-plots`. [Online; accessed October 17, 2017].

European Southern Observatory. E-elt optics, 2011. URL `https://www.eso.org/sci/facilities/eelt/telescope/mirrors/`. [Online; accessed October 20, 2017].

A. T. Fam. Efficient complex matrix multiplication. *IEEE Transactions on Computers*, 37(7):877–879, 1988.

J. W. Goodman. *Introduction to Fourier optics.* Roberts and Company Publishers, 2005.

E. P. Goodwin and J. C. Wyant. Field guide to interferometric optical testing. SPIE, 2006.

J. Herrmann. Cross coupling and aliasing in modal wave-front estimation. *JOSA*, 71(8):989–992, 1981.

A. J. Janssen, S. van Haver, P. Dirksen, and J. J. Braat. Zernike representation and strehl ratio of optical systems with variable numerical aperture. *Journal of Modern Optics*, 55(7):1127–1157, 2008.

A. J. E. M. Janssen. Zernike circle polynomials and infinite integrals involving the product of bessel functions. *arXiv preprint arXiv:1007.0667*, 2010.

A. J. E. M. Janssen. Zernike expansion of derivatives and laplacians of the zernike circle polynomials. *JOSA A*, 31(7):1604–1613, 2014.

D. Malacara. *Optical shop testing*, volume 59. John Wiley & Sons, 2007.

N. Matsumoto, T. Ando, T. Inoue, Y. Ohtake, N. Fukuchi, and T. Hara. Generation of high-quality higher-order laguerre-gaussian beams using liquid-crystal-on-silicon spatial light modulators. *JOSA A*, 25(7):1642–1651, 2008.

R. Navarro, R. Rivera, and J. Aporta. Representation of wavefronts in free-form transmission pupils with complex zernike polynomials. *Journal of optometry*, 4(2):41–48, 2011.

W. H. Press, S. A. Teukolsky, W. T. Vetterling, and B. P. Flannery. *Numerical recipes in FORTRAN 77, vol. 1.* University of Cambridge, 1992.

O. Soloviev and G. Vdovin. Estimation of the total error of modal wavefront reconstruction with zernike polynomials and hartmann-shack test. In *5th International Workshop on Adaptive Optics for Industry and Medicine*, volume 6018, page 60181D. International Society for Optics and Photonics, 2006.

P. C. Stephenson. Recurrence relations for the cartesian derivatives of the zernike polynomials. *JOSA A*, 31(4):708–715, 2014.

L. N. Thibos, R. A. Applegate, J. T. Schwiegerling, and R. Webb. Standards for reporting the optical aberrations of eyes. *Journal of refractive surgery*, 18(5):S652–S660, 2002.

Trioptics. Wavefront and surface measurement with interferometers and shack hartmann sensors, 2017. URL `https://www.trioptics.com/knowledge-base/wavefront-and-surface-measurement/`. [Online; accessed October 20, 2017].

H. H. van Brug. Efficient cartesian representation of zernike polynomials in computer memory. In *Fifth International Topical Meeting on Education and Training in Optics*, pages 382–392. International Society for Optics and Photonics, 1997.

J. C. Wyant and K. Creath. Basic wavefront aberration theory for optical metrology. *Applied optics and optical engineering*, 11(s 29):2, 1992.

H. Zhang, J. Xie, J. Liu, and Y. Wang. Elimination of a zero-order beam induced by a pixelated spatial light modulator for holographic projection. *Applied optics*, 48(30):5834–5841, 2009.

Z. Zhang, Z. You, and D. Chu. Fundamentals of phase-only liquid crystal on silicon (lcos) devices. *Light: Science & Applications*, 3(10):e213, 2014.

A Derivation of the conversion relations between real and complex polynomial coefficients

Zernike polynomials form a complete set of polynomials that are orthogonal in a continous fashion of the interior of a unit circle (Wyant and Creath, 1992). Therefore, if we restrict ourselves to the unit disc, the following equation must hold when describing an sufficiently smooth complex wavefront

$$\sum_{m=-\infty}^{\infty} \sum_{n\in\eta_m} a_n^m Z_n^m(\rho,\theta) = \sum_{m=-\infty}^{\infty} \sum_{n\in\eta_m} \alpha_n^m C_n^m(\rho,\theta), \tag{A.1}$$

where η_m is the set of allowed values of n such that Equations 2.5, 2.6 and 2.7 all hold.

The left hand side of this equation can be expanded in terms of sines and cosines, where for ease of writing the radial terms will be omitted

$$\begin{aligned}
&\sum_{n\in\eta_m} \left\{ \sum_{m=0}^{\infty} a_n^m N_n^m \cos(m\theta) + \sum_{m'=1}^{\infty} a_n^{-m'} N_n^{-m'} \sin\left(m'\theta\right) \right\} \\
&= \sum_{n\in\eta_m} \Bigg\{ \sum_{m=1}^{\infty} N_n^m \left(a_{n,r}^m \cos(m\theta) + a_{n,r}^{-m} \sin(m\theta)\right) + \\
&N_n^m \left(a_{n,i}^m i\cos(m\theta) + a_{n,i}^{-m} i\sin(m\theta)\right) \Bigg\} + N_n^0 \left(a_{n,r}^0 + i a_{n,i}^0\right).
\end{aligned} \tag{A.2}$$

where subscript r and i denote the real and imaginary part of the coefficient respectively.

The right hand side can equally be expanded in sines and cosines. If we don't write the radial terms, it can be expressed as

$$\begin{aligned}
&\sum_{n\in\eta_m} \left\{ \sum_{m=0}^{\infty} \alpha_n^m \left(\cos(m\theta) + i\sin(m\theta)\right) + \sum_{m'=1}^{\infty} \alpha_n^{-m'} \left(\cos(m'\theta) - i\sin(m'\theta)\right) \right\} \\
&= \sum_{n\in\eta_m} \Bigg\{ \sum_{m=1}^{\infty} \left(\alpha_{n,r}^m + \alpha_{n,r}^{-m}\right)\cos(m\theta) + \left(-\alpha_{n,i}^m + \alpha_{n,i}^{-m}\right)\sin(m\theta) + \\
&\left(\alpha_{n,i}^m + \alpha_{n,i}^{-m}\right) i\cos(m\theta) + \left(\alpha_{n,r}^m - \alpha_{n,r}^{-m}\right) i\sin(m\theta) \Bigg\} + \left(\alpha_{n,r}^0 + \alpha_{n,i}^0\right).
\end{aligned} \tag{A.3}$$

Substituting Equations A.2 and A.3 back in Equation A.1, it becomes apparent that the following relations must hold between the coefficients

$$\mathrm{Re}\left(a_n^m\right) = \begin{cases} \dfrac{1}{N_n^m}\,\mathrm{Re}\left(\alpha_n^{|m|} + \alpha_n^{-|m|}\right), & \text{if } m > 0 \\ \dfrac{-1}{N_n^m}\,\mathrm{Im}\left(\alpha_n^{|m|} - \alpha_n^{-|m|}\right), & \text{if } m < 0 \\ \dfrac{1}{N_n^m}\,\mathrm{Re}\left(\alpha_n^m\right), & \text{if } m = 0, \end{cases} \tag{A.4}$$

$$\mathrm{Im}\left(a_n^m\right) = \begin{cases} \dfrac{1}{N_n^m}\,\mathrm{Im}\left(\alpha_n^{|m|} + \alpha_n^{-|m|}\right), & \text{if } m > 0 \\ \dfrac{1}{N_n^m}\,\mathrm{Re}\left(\alpha_n^{|m|} - \alpha_n^{-|m|}\right), & \text{if } m < 0 \\ \dfrac{1}{N_n^m}\,\mathrm{Im}\left(\alpha_n^m\right), & \text{if } m = 0. \end{cases} \tag{A.5}$$

These relationships hold for an imaginary wavefront. When describing a real wavefront (which is the case in a physical experiment), the right-hand side of Equation A.5 becomes 0, and $\mathrm{Re}\left(a_n^m\right) = a_n^m$.

These relations can also be reversed, expressing α_n^m in terms of a_n^m

$$\alpha_n^m = \begin{cases} N_n^m \dfrac{a_n^{|m|} - i a_n^{-|m|}}{2}, & \text{if } m > 0 \\ N_n^m \dfrac{a_n^{|m|} + i a_n^{-|m|}}{2}, & \text{if } m < 0 \\ N_n^m a_n^m, & \text{if } m = 0, \end{cases} \tag{A.6}$$

B Additional coefficient convergence graphs

The graphs of the specific Zernike experiment, showing the convergence of the coefficients fit different fitting powers. These are the graphs not shown in Section 5.2.1

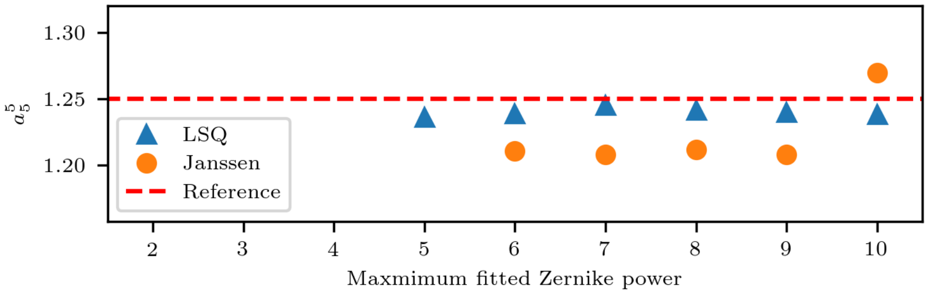

Figure B.1: Convergence of coefficients for the `5_5` experiment.

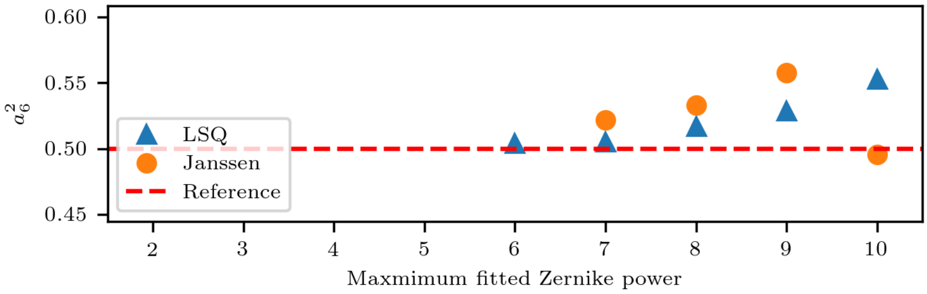

Figure B.2: Convergence of coefficients for the `6_2` experiment.

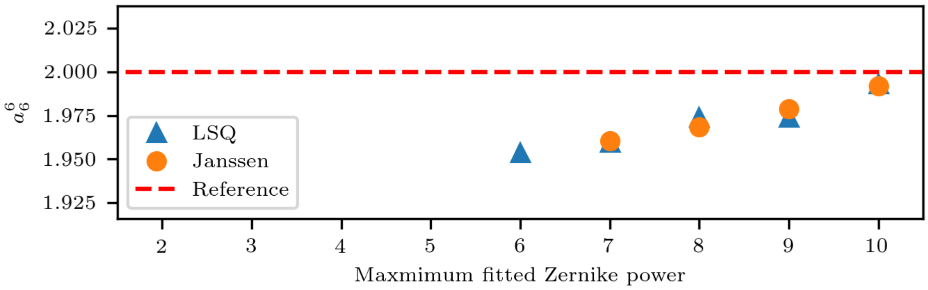

Figure B.3: Convergence of coefficients for the `6_6` experiment.

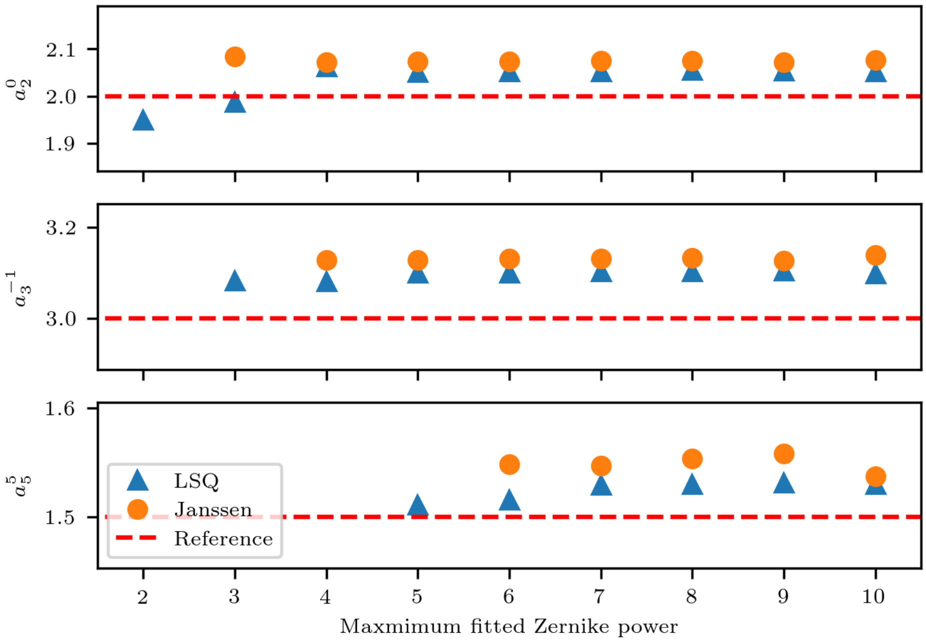

Figure B.4: Convergence of coefficients for the `3_zerns_2` experiment.

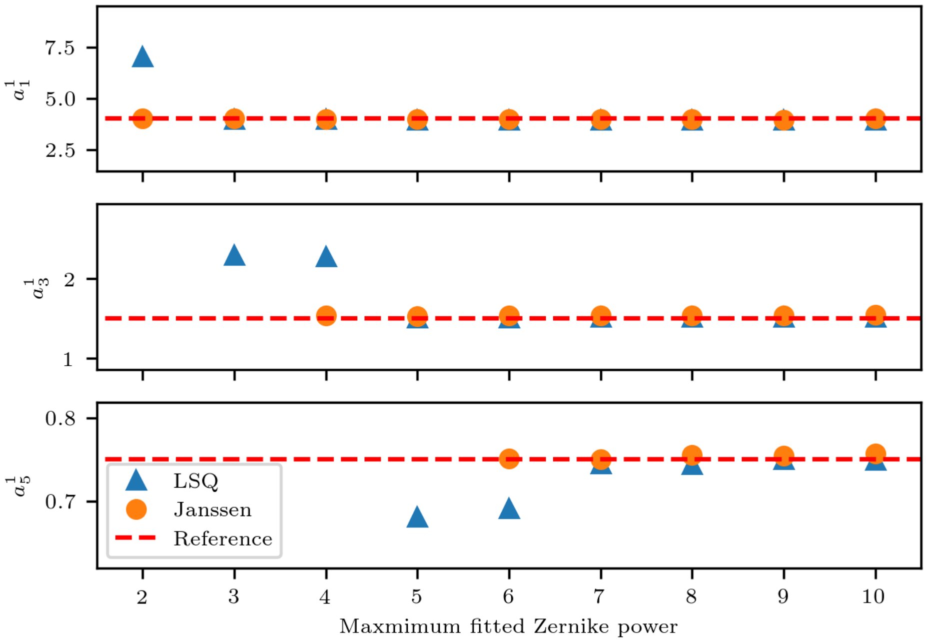

Figure B.5: Convergence of coefficients for the `sub_zerns_2` experiment.

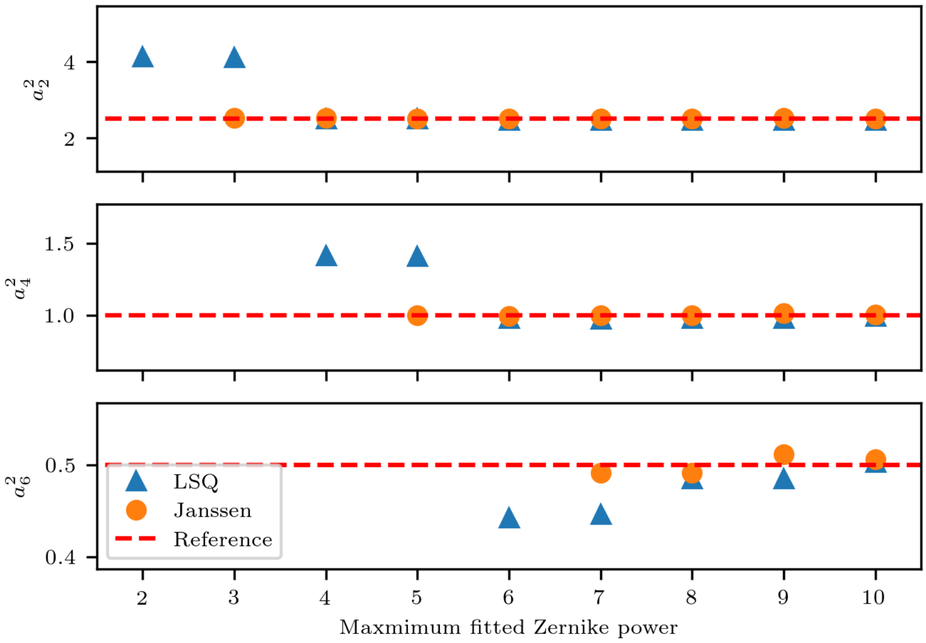

Figure B.6: Convergence of coefficients for the `sub_zerns_4` experiment.

C RMS landscapes and optimized center and radius positions

This appendix shows all RMS landscapes and the corresponding center and radius positions. Discussion of the results is found in Section 5.4.

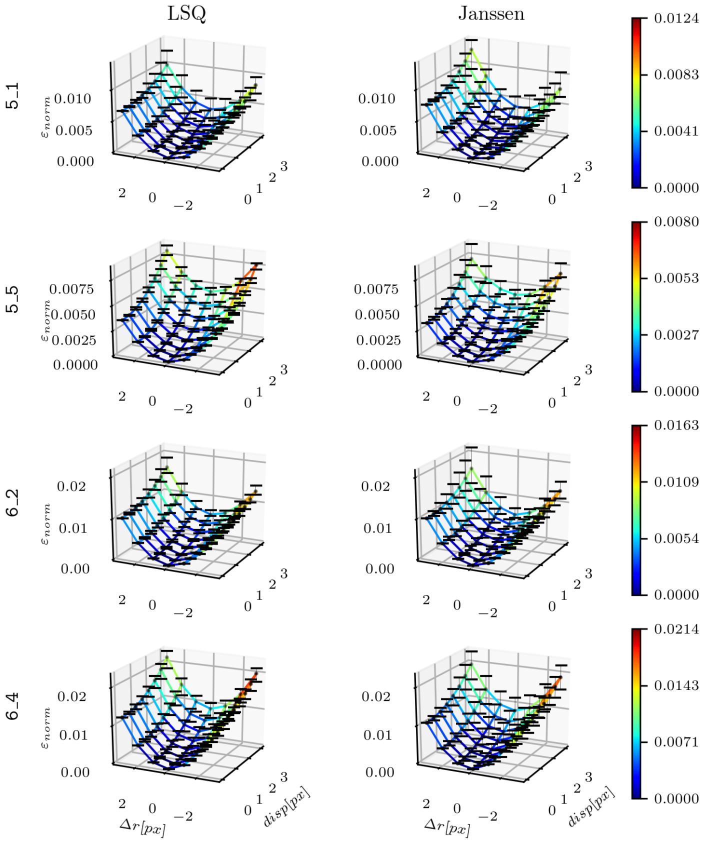

Figure C.1: The RMS error landscape for the first four single Zernike experiments. The surface is plot through the median of the values at each points of $(disp, \Delta r)$. The whiskers denote the maximum and minimum value of the values at those points.

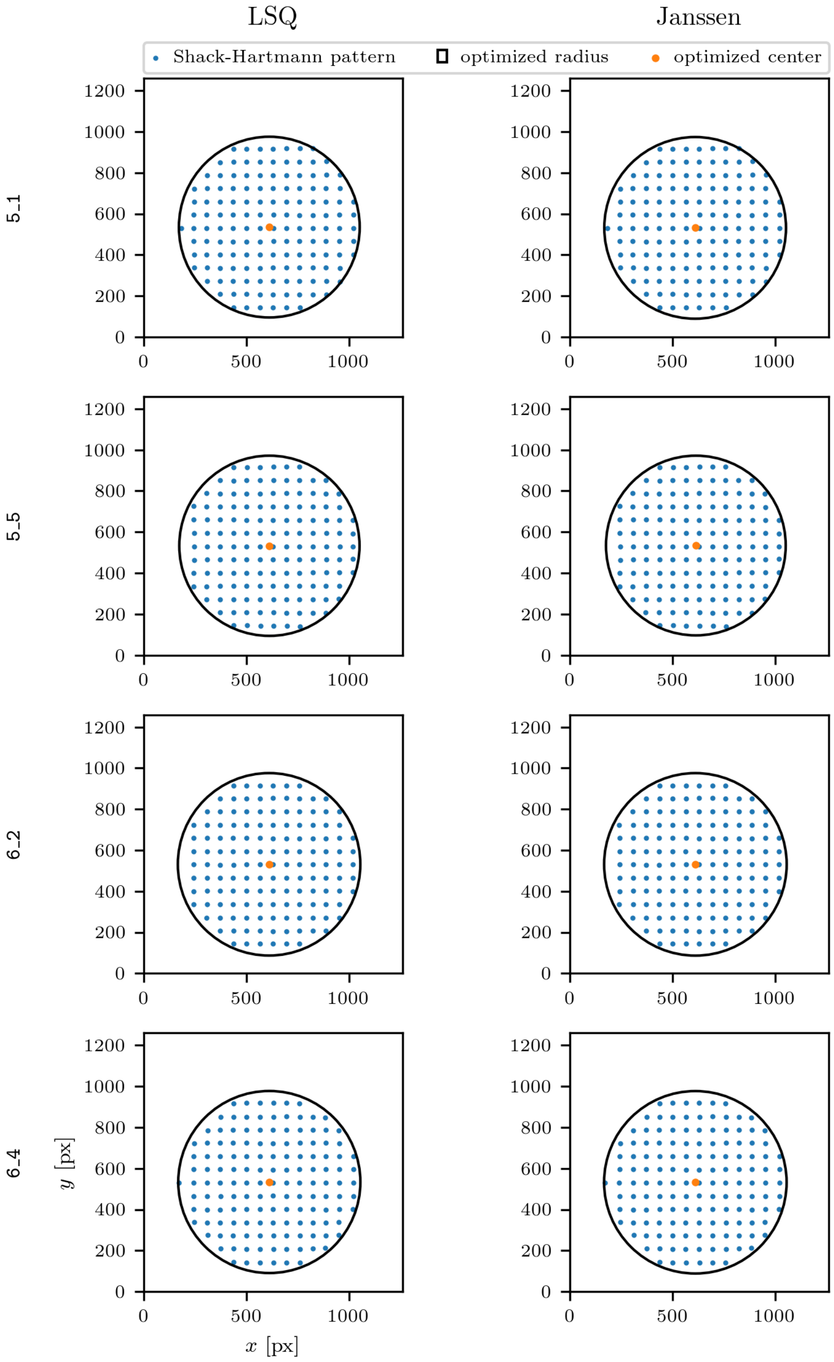

Figure C.2: The Shack-Hartmann pattern and estimated centers and radii for the first four single Zernike experiments.

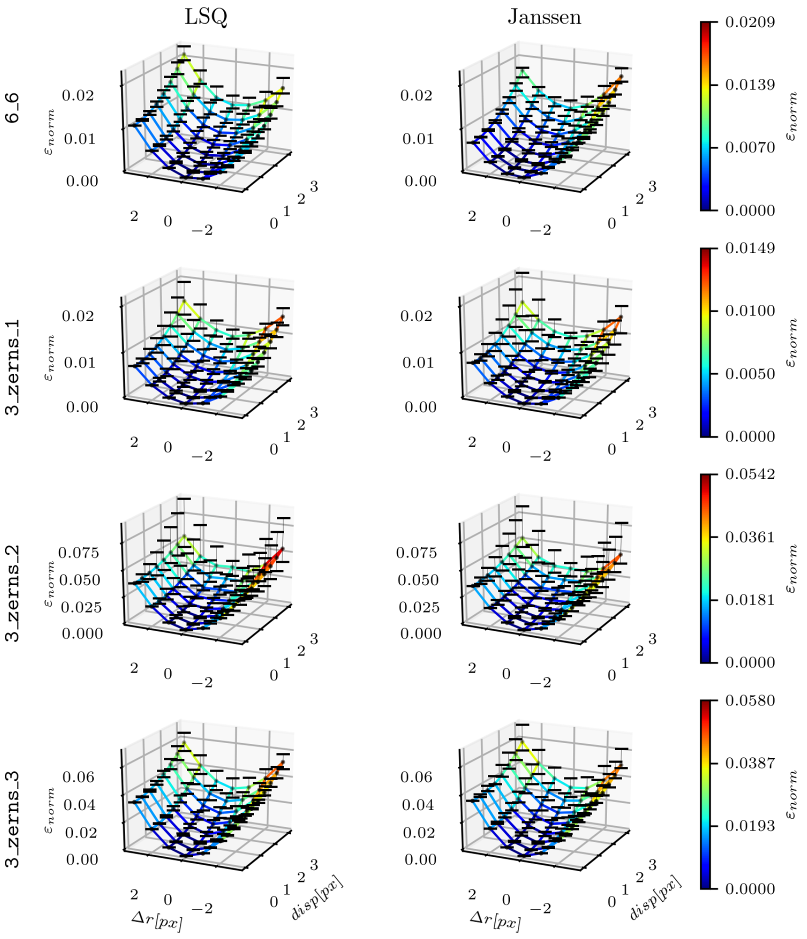

Figure C.3: The RMS error landscape for the second four single Zernike experiments. The surface is plot through the median of the values at each points of $(disp, \Delta r)$. The whiskers denote the maximum and minimum value of the values at those points.

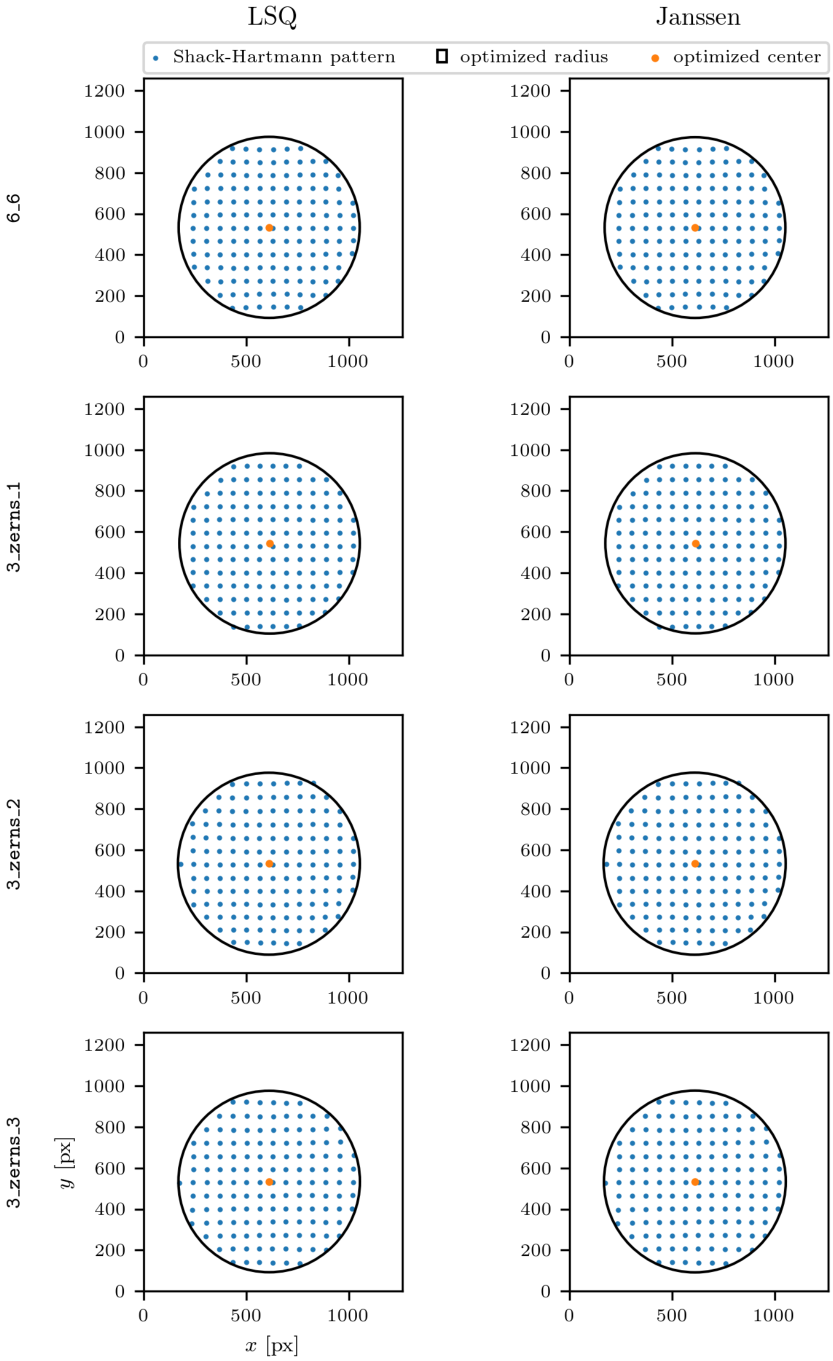

Figure C.4: The Shack-Hartmann pattern and estimated centers and radii for the second four Single Zernike experiments.

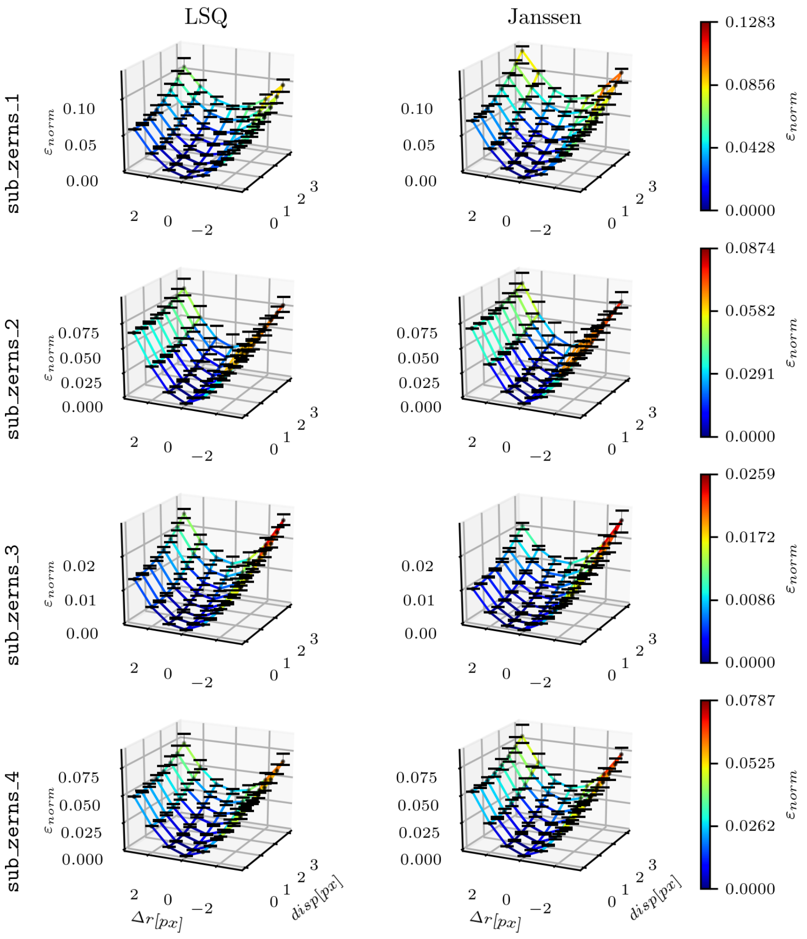

Figure C.5: The RMS error landscape for the last four single Zernike experiments. The surface is plot through the median of the values at each points of $(disp, \Delta r)$. The whiskers denote the maximum and minimum value of the values at those points.

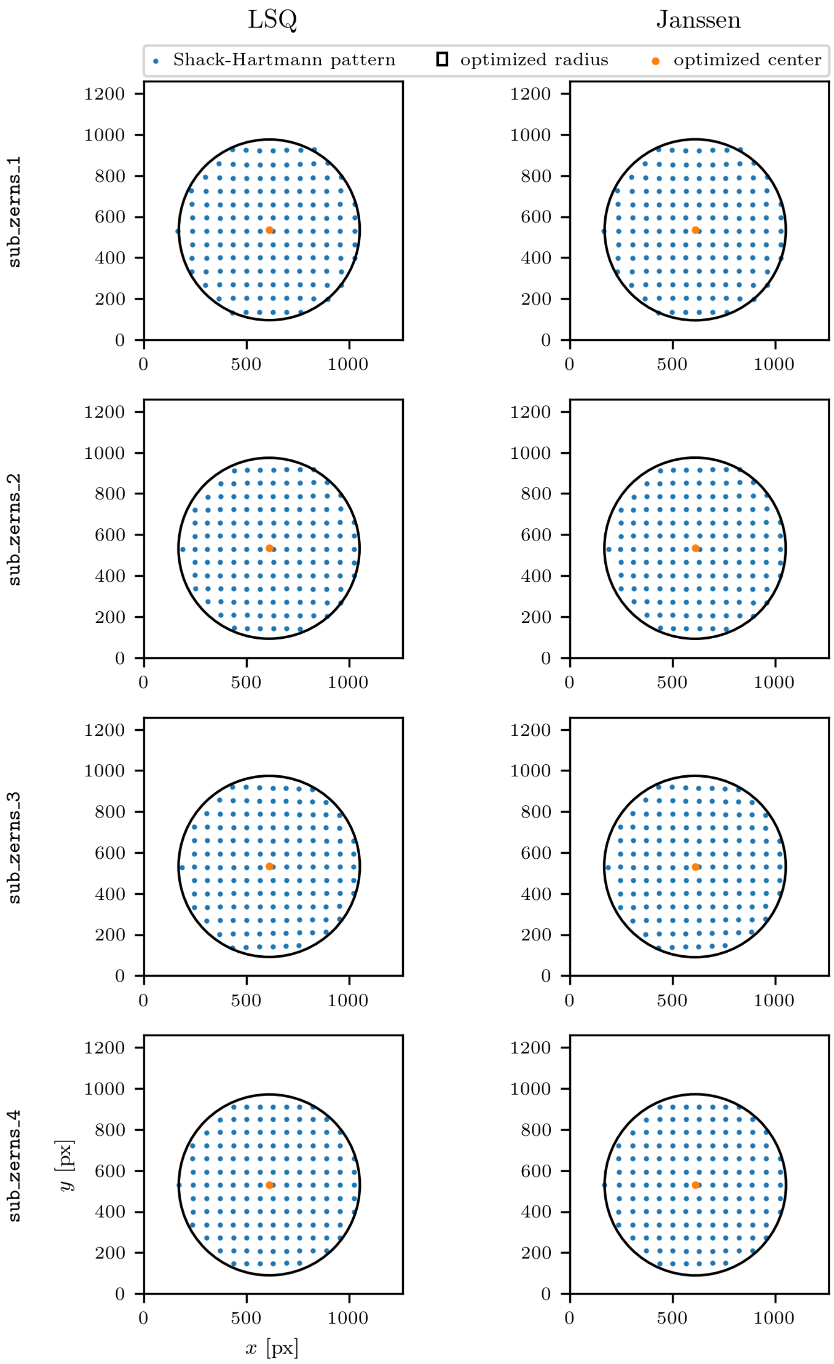

Figure C.6: The Shack-Hartmann pattern and estimated centers and radii for the last four single Zernike experiments.

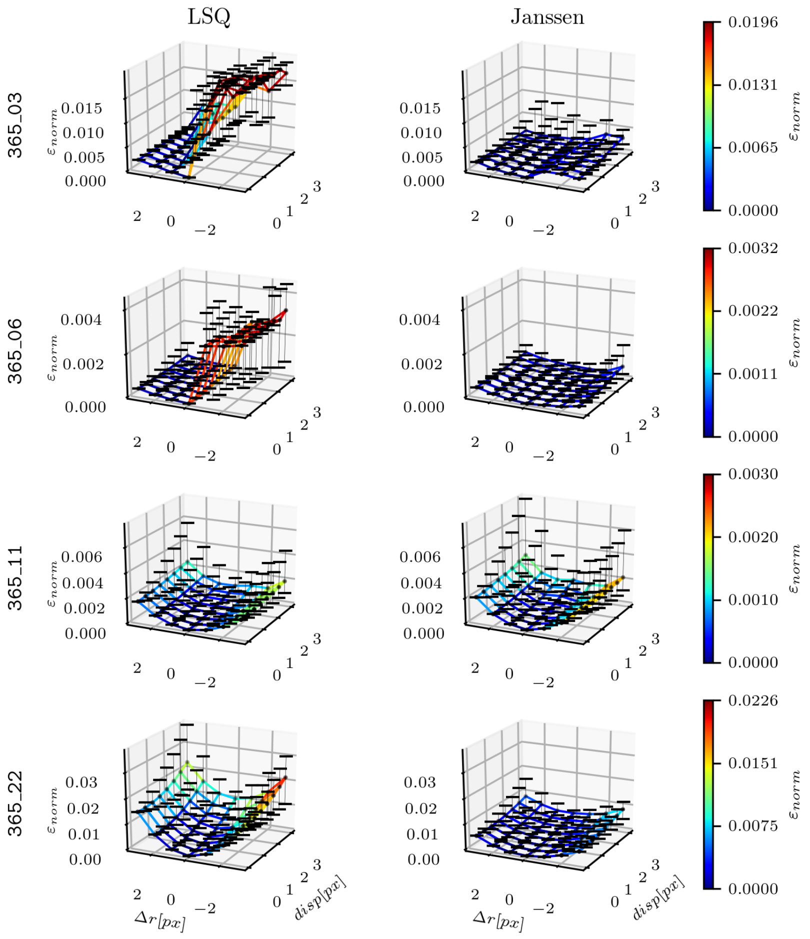

Figure C.7: The RMS error landscape for the first four lens experiments. The surface is plot through the median of the values at each points of $(disp, \Delta r)$. The whiskers denote the maximum and minimum value of the values at those points.

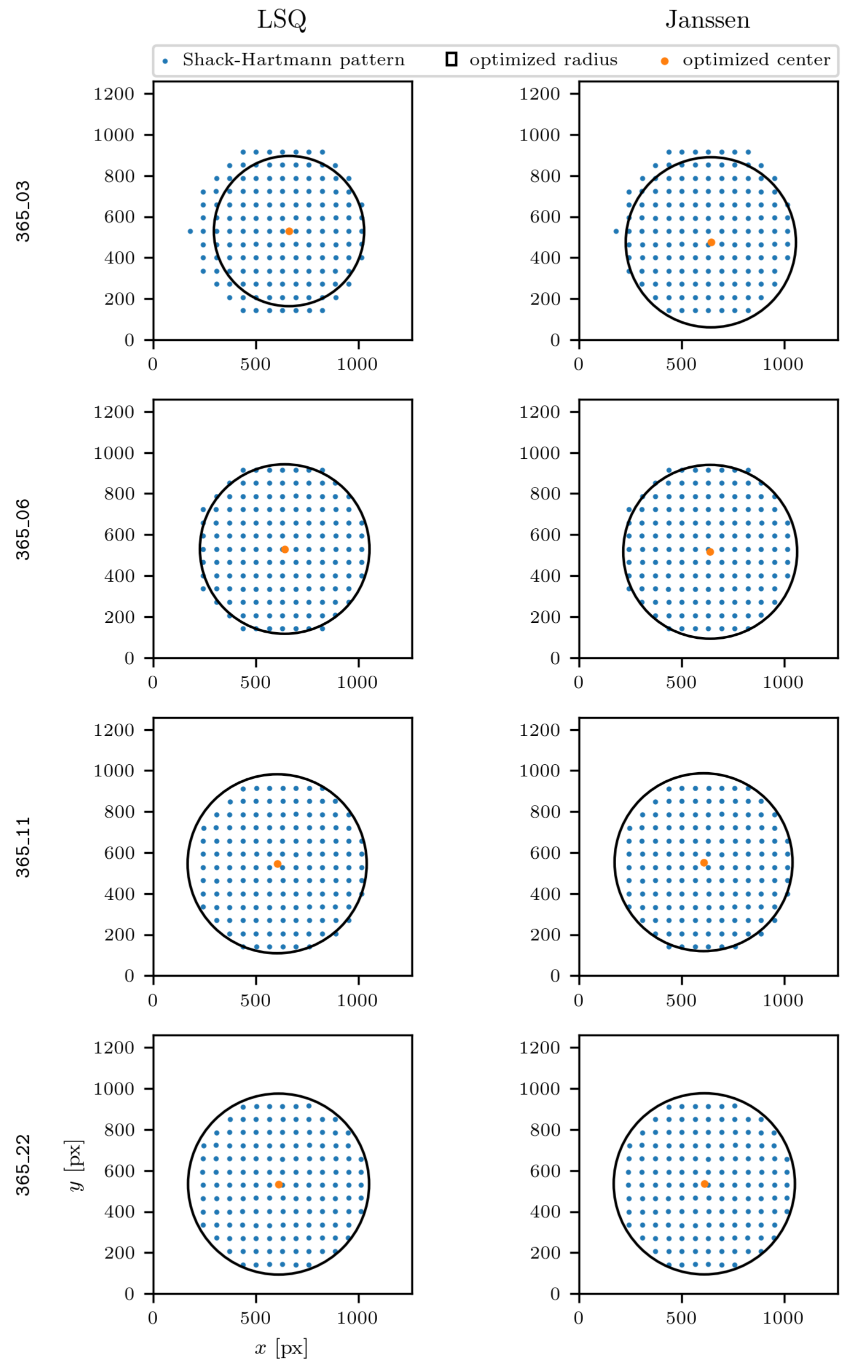

Figure C.8: The Shack-Hartmann pattern and estimated centers and radii for the first four lens experiments.

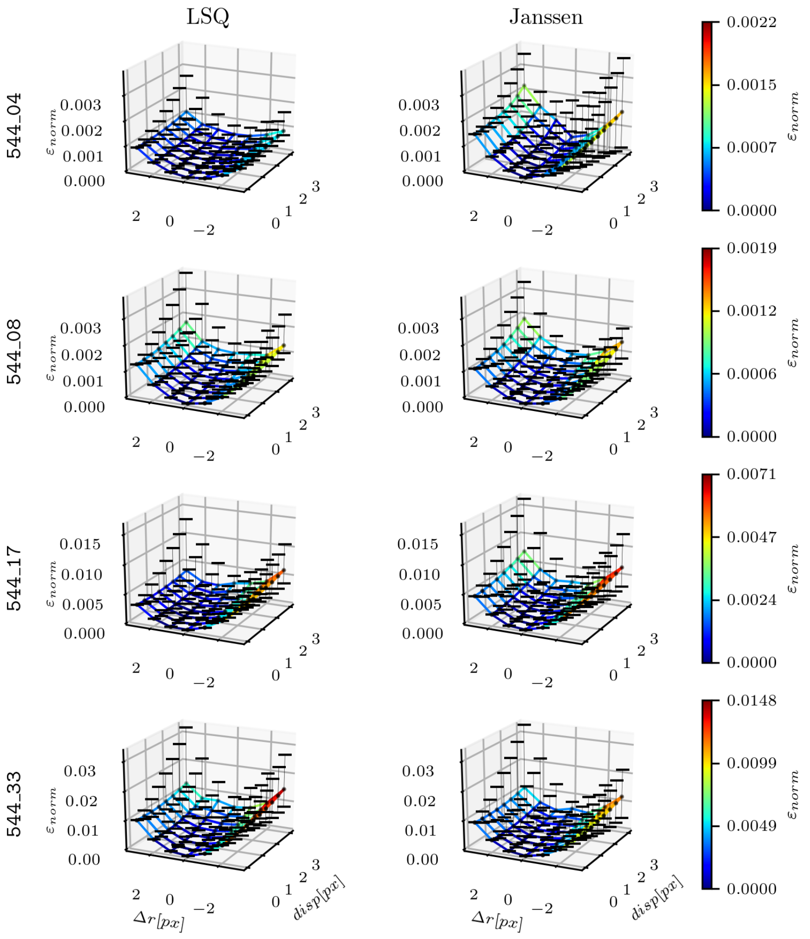

Figure C.9: The RMS error landscape for the last four lens experiments. The surface is plot through the median of the values at each points of $(disp, \Delta r)$. The whiskers denote the maximum and minimum value of the values at those points.

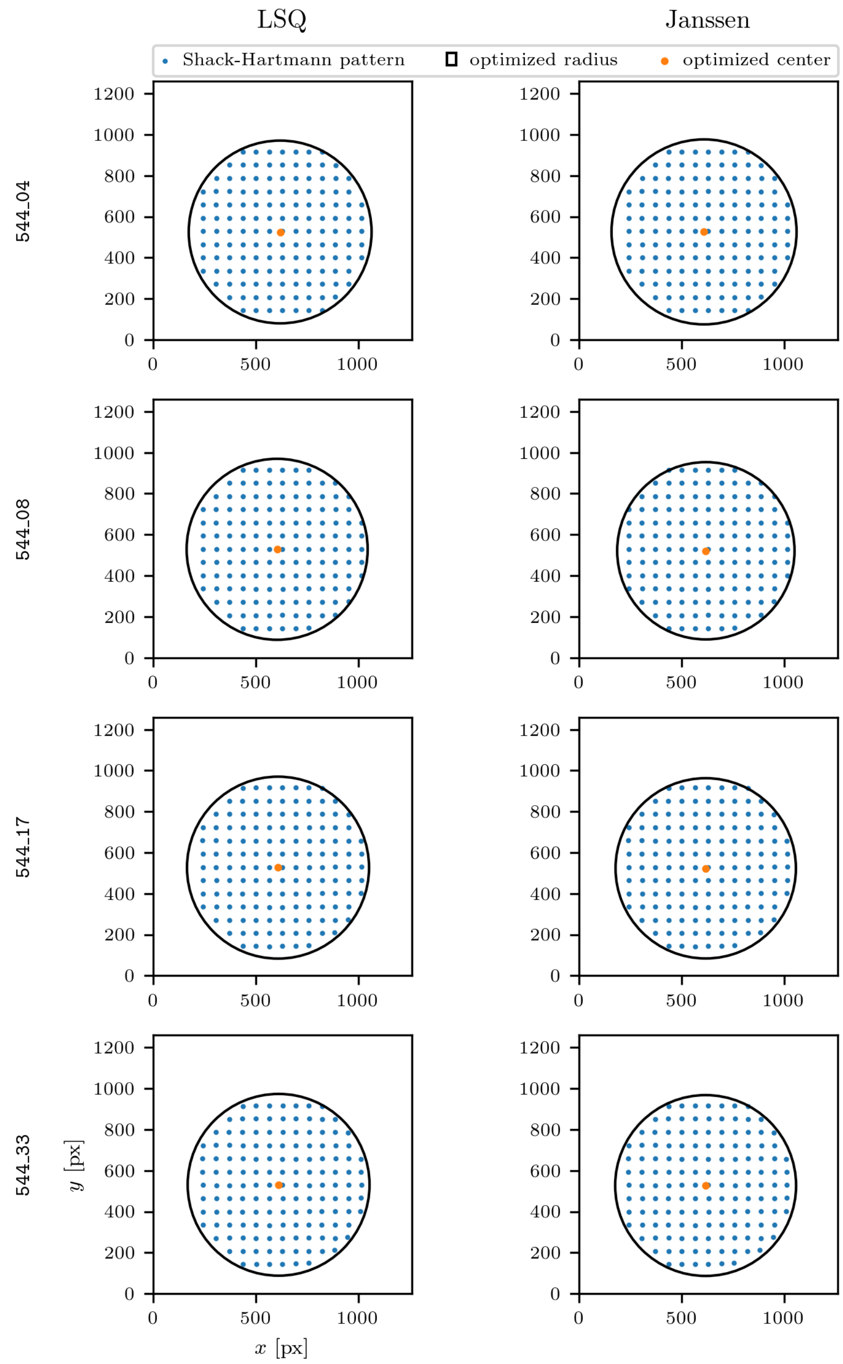

Figure C.10: The Shack-Hartmann pattern and estimated centers and radii for the last four lens experiments.

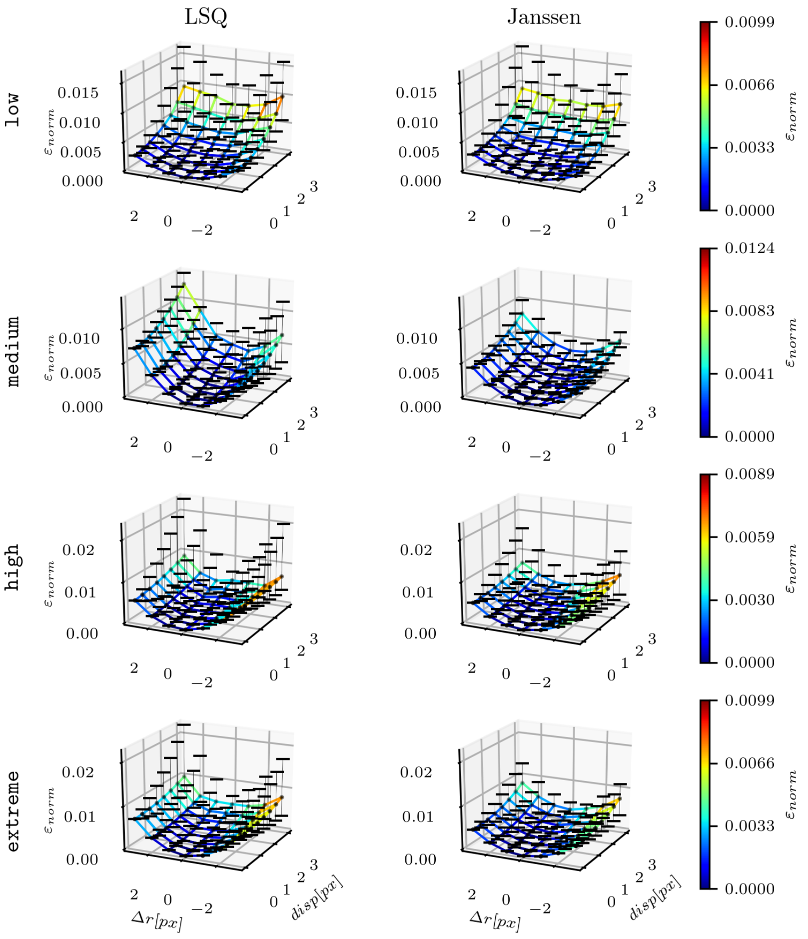

Figure C.11: The RMS error landscape for the four random phase experiments. The surface is plot through the median of the values at each points of $(disp, \Delta r)$. The whiskers denote the maximum and minimum value of the values at those points.

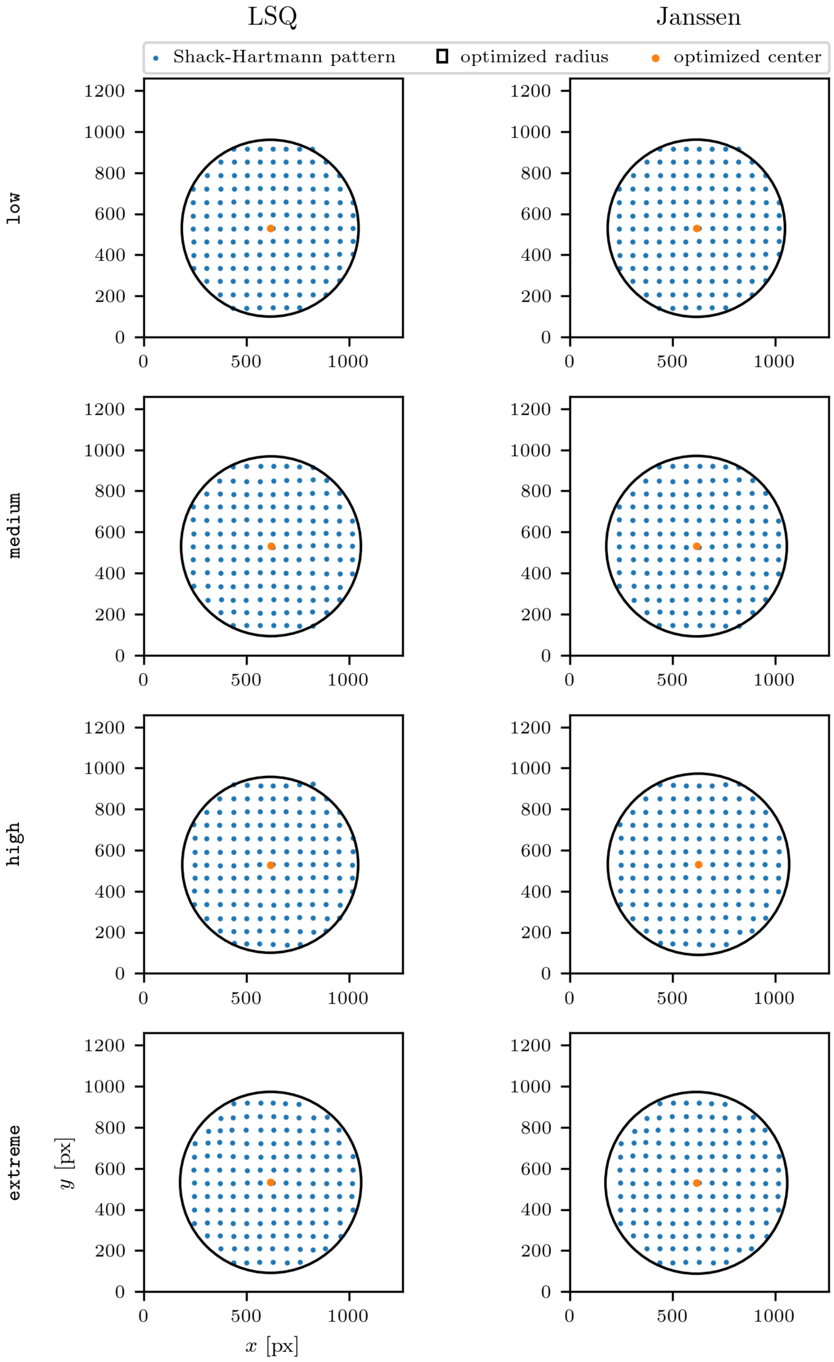

Figure C.12: The Shack-Hartmann pattern and estimated centers and radii for the four random phase experiments.

D Derivation of the non-orthogonality of the least-squares geometry matrix

This section will prove that in the limit of infinite spots on the Shack-Hartmann sensor, the geometry matrix constructed does not have orthogonal columns. It is also derived which columns are not orthogonal. This is in turn used to predict which Zernike coefficients will experience cross-talk.

Recall that the geometry matrix is constructed by averaging the partial derivative of the Zernike polynomial over a certain sub-aperture, and put in a matrix as follows

$$G = \begin{bmatrix} \left.\overline{\frac{\partial Z_1}{\partial x}}\right|_1 & \left.\overline{\frac{\partial Z_1}{\partial x}}\right|_2 & \cdots & \left.\overline{\frac{\partial Z_1}{\partial x}}\right|_{n_{\text{spot}}} & \left.\overline{\frac{\partial Z_1}{\partial y}}\right|_1 & \left.\overline{\frac{\partial Z_1}{\partial y}}\right|_2 & \cdots & \left.\overline{\frac{\partial Z_1}{\partial y}}\right|_{n_{\text{spot}}} \\ \left.\overline{\frac{\partial Z_2}{\partial x}}\right|_1 & \left.\overline{\frac{\partial Z_2}{\partial x}}\right|_2 & \cdots & \left.\overline{\frac{\partial Z_2}{\partial x}}\right|_{n_{\text{spot}}} & \left.\overline{\frac{\partial Z_2}{\partial y}}\right|_1 & \left.\overline{\frac{\partial Z_2}{\partial y}}\right|_2 & \cdots & \left.\overline{\frac{\partial Z_2}{\partial y}}\right|_{n_{\text{spot}}} \\ \vdots & \vdots & \ddots & \vdots & \vdots & \vdots & \ddots & \vdots \\ \left.\overline{\frac{\partial Z_J}{\partial x}}\right|_1 & \left.\overline{\frac{\partial Z_J}{\partial x}}\right|_2 & \cdots & \left.\overline{\frac{\partial Z_J}{\partial x}}\right|_{n_{\text{spot}}} & \left.\overline{\frac{\partial Z_J}{\partial y}}\right|_1 & \left.\overline{\frac{\partial Z_J}{\partial y}}\right|_2 & \cdots & \left.\overline{\frac{\partial Z_J}{\partial y}}\right|_{n_{\text{spot}}} \end{bmatrix}^T . \tag{D.1}$$

n_{spot} is taken to be very large, such that the average over the sub-aperture is equal to evaluating the function in the center of the sub-aperture. If this is the case, then an inner product between column i and column j can be written as

$$\langle G_i, G_j \rangle = \sum_{n=1}^{n_{\text{spot}}} \left[\left.\frac{\partial Z_i}{\partial x}\frac{\partial Z_j}{\partial x}\right|_n + \left.\frac{\partial Z_i}{\partial y}\frac{\partial Z_j}{\partial y}\right|_n \right], \tag{D.2}$$

where G_i and G_j denote the columns i and j of matrix G. From Monte Carlo integration methods, it is known that (Press et al., 1992)

$$\int f dV \approx \frac{V}{N} \sum_{i=1}^{N} f(x_i), \tag{D.3}$$

where V is the volume in which the points x_i are taken from randomly. If this principle is applied to internal product, we can approximate it as an integral

$$\sum_{n=1}^{n_{\text{spot}}} \left[\left.\frac{\partial Z_i}{\partial x}\frac{\partial Z_j}{\partial x}\right|_n + \left.\frac{\partial Z_i}{\partial y}\frac{\partial Z_j}{\partial y}\right|_n \right] \approx \frac{\pi}{N} \int_\Omega \left(\frac{\partial Z_i(\mathbf{x})}{\partial x}\frac{\partial Z_j(\mathbf{x})}{\partial x} + \frac{\partial Z_i(\mathbf{x})}{\partial y}\frac{\partial Z_j(\mathbf{x})}{\partial y} \right) \mathrm{d}\mathbf{x}, \tag{D.4}$$

where $\mathbf{x} \in \Omega$, which denotes the unit disc. The orthogonality of the columns of the geometry matrix G can therefore be approximated by the right hand side integral. To aid us in evaluating, the derivatives of the Zernikes can be expressed as a finite sum of Zernike polynomials, which are orthogonal on the unit disc. The x- and y-derivates can be expressed as (Stephenson, 2014)

$$\frac{\partial Z_n^m}{\partial x} = \sum_{n'=0}^{n-1} \left[a^{nm}_{n',m-1} Z_{n'}^{\alpha_m |m-1|} + \alpha_m \mathrm{sng}(m+1) a^{nm}_{n',m+1} Z_{n'}^{\alpha_m |m+1|} \right] \tag{D.5}$$

$$\frac{\partial Z_n^m}{\partial y} = \sum_{n'=0}^{n-1} \left[-\alpha_m \mathrm{sgn}(m-1) a^{nm}_{n',m-1} Z_{n'}^{-\alpha_m |m-1|} + a^{nm}_{n',m+1} Z_{n'}^{-\alpha_m |m+1|} \right], \tag{D.6}$$

where

$$a^{nm}_{n',m'} = \begin{cases} \sqrt{\dfrac{2-\delta_{m0}}{2-\delta_{m'0}}(n+1)(n'+1)} & \text{if } n \geq |m|, (n-|m|) \text{ is even,} \\ & n' \geq |m'|, \text{and } (n'-|m'|) \text{ is even} \\ 0 & \text{otherwise,} \end{cases} \tag{D.7}$$

and

$$\alpha_m = \begin{cases} +1 & \text{if } m \geq 0, \\ -1 & \text{if } m < 0. \end{cases} \tag{D.8}$$

Using these explicit expressions for the cartesian derivatives of Zernike polynomials, one can see that the product of two different derivatives of Zernike polynomials can be expressed as a double sum. For instance, the x-derivative product can be expressed as

$$\begin{aligned} \frac{\partial Z_n^m}{\partial x}\frac{\partial Z_{n'}^{m'}}{\partial x} = \sum_{\eta=0}^{n-1}\sum_{\eta'=0}^{n'-1} & \left[a^{nm}_{\eta,m-1} Z_{\eta}^{\alpha_m |m-1|} + \alpha_m \mathrm{sng}(m+1) a^{nm}_{\eta,m+1} Z_{\eta}^{\alpha_m |m+1|} \right] \times \\ & \left[a^{n'm'}_{\eta',m'-1} Z_{\eta'}^{\alpha'_m |m'-1|} + \alpha'_m \mathrm{sng}(m'+1) a^{n'm'}_{\eta',m'+1} Z_{\eta'}^{\alpha'_m |m'+1|} \right]. \end{aligned} \tag{D.9}$$

Due to the orthogonality of the Zernike polynomials, the integral over the unit disc of these products only is nonzero in 2 distinct cases. The first case, where $m' \neq 0$, the integral in nonzero if

$$\begin{aligned} \{(n,m,n',m') \in \mathbb{Z} \mid n \in \eta_m,\ & m = m' \text{ or } m = m' \pm 2, \\ & n' > n,\ n \geq m' + 2,\ n' \in \eta_{m'},\ m' \neq 0\}, \end{aligned}$$

In the case that $m' = 0$, the integral in nonzero if

$$\begin{aligned} \{(n,m,n',m') \in \mathbb{Z} \mid n \in \eta_m,\ & m = m' \text{ or } m = m' + 2, \\ & n' > n,\ n \geq 2,\ n' \in \eta_{m'},\ m' = 0\}, \end{aligned}$$

where in both cases η_m and $\eta_{m'}$ are the sets of allowed values for n and n' dependent on m and m' such that Equations 2.5, 2.6 and 2.7 are all met.

E Tables of used coefficient values

Table E.1: Coefficients used in specific Zernike experiments, rounded off to 3 significant numbers

Code	Coefficients		
`5_1`	a_5^1 0.750		
`5_5`	a_5^5 1.250		
`6_2`	a_6^2 0.500		
`6_4`	a_6^4 1.000		
`6_6`	a_6^6 2.000		
`3_zerns_1`	a_2^0 2.000	a_4^4 1.500	a_6^{-2} 0.500
`3_zerns_2`	a_2^0 2.000	a_3^{-1} 3.000	a_5^5 1.500
`3_zerns_3`	a_2^{-2} 2.000	a_4^0 1.500	a_6^{-4} 0.750
`sub_zerns_1`	a_2^0 4.000	a_4^0 1.500	a_6^0 0.750
`sub_zerns_2`	a_1^1 4.000	a_3^1 1.500	a_5^1 0.750
`sub_zerns_3`	a_3^3 2.500	a_5^3 0.750	
`sub_zerns_4`	a_2^2 2.500	a_4^2 1.000	a_6^2 0.500

Table E.2: Coefficients used in LEICA experiments, rounded off to 3 significant digits

Code	Coefficients								
544_04	a_1^{-1}	a_1^{1}	a_2^{-2}	a_2^{0}	a_2^{2}	a_3^{-3}	a_3^{-1}	a_3^{1}	a_3^{3}
	0.016	-0.016	0.042	-0.000	-0.029	0.027	0.096	-0.095	-0.003
	a_4^{-4}	a_4^{-2}	a_4^{0}	a_4^{2}	a_4^{4}	a_5^{-5}	a_5^{-3}	a_5^{-1}	a_5^{1}
	-0.007	-0.003	-0.032	0.001	-0.006	0.000	-0.005	0.011	-0.006
	a_5^{3}	a_5^{5}	a_6^{-4}	a_6^{-2}	a_6^{0}	a_6^{2}	a_6^{4}	a_7^{-3}	a_7^{-1}
	-0.002	0.010	-0.013	-0.018	-0.019	0.019	-0.005	-0.018	-0.014
	a_7^{1}	a_7^{3}	a_8^{-2}	a_8^{0}	a_8^{2}	a_9^{-1}	a_9^{1}	a_{10}^{0}	
	-0.007	-0.000	0.038	-0.027	-0.004	0.022	-0.018	-0.018	
544_08	a_1^{-1}	a_1^{1}	a_2^{-2}	a_2^{0}	a_2^{2}	a_3^{-3}	a_3^{-1}	a_3^{1}	a_3^{3}
	0.032	-0.032	0.084	-0.001	-0.057	0.054	0.191	-0.190	-0.006
	a_4^{-4}	a_4^{-2}	a_4^{0}	a_4^{2}	a_4^{4}	a_5^{-5}	a_5^{-3}	a_5^{-1}	a_5^{1}
	-0.014	-0.007	-0.064	0.001	-0.013	0.001	-0.009	0.021	-0.012
	a_5^{3}	a_5^{5}	a_6^{-4}	a_6^{-2}	a_6^{0}	a_6^{2}	a_6^{4}	a_7^{-3}	a_7^{-1}
	-0.004	0.021	-0.026	-0.036	-0.037	0.038	-0.011	-0.035	-0.028
	a_7^{1}	a_7^{3}	a_8^{-2}	a_8^{0}	a_8^{2}	a_9^{-1}	a_9^{1}	a_{10}^{0}	
	-0.013	-0.001	0.076	-0.054	-0.008	0.044	-0.036	-0.036	
544_17	a_1^{-1}	a_1^{1}	a_2^{-2}	a_2^{0}	a_2^{2}	a_3^{-3}	a_3^{-1}	a_3^{1}	a_3^{3}
	0.064	-0.065	0.169	-0.002	-0.114	0.109	0.382	-0.379	-0.011
	a_4^{-4}	a_4^{-2}	a_4^{0}	a_4^{2}	a_4^{4}	a_5^{-5}	a_5^{-3}	a_5^{-1}	a_5^{1}
	-0.028	-0.014	-0.127	0.002	-0.026	0.002	-0.018	0.042	-0.023
	a_5^{3}	a_5^{5}	a_6^{-4}	a_6^{-2}	a_6^{0}	a_6^{2}	a_6^{4}	a_7^{-3}	a_7^{-1}
	-0.009	0.042	-0.052	-0.071	-0.074	0.077	-0.022	-0.070	-0.055
	a_7^{1}	a_7^{3}	a_8^{-2}	a_8^{0}	a_8^{2}	a_9^{-1}	a_9^{1}	a_{10}^{0}	
	-0.026	-0.002	0.151	-0.108	-0.016	0.087	-0.072	-0.072	
544_33	a_1^{-1}	a_1^{1}	a_2^{-2}	a_2^{0}	a_2^{2}	a_3^{-3}	a_3^{-1}	a_3^{1}	a_3^{3}
	0.128	-0.130	0.338	-0.003	-0.229	0.218	0.765	-0.758	-0.022
	a_4^{-4}	a_4^{-2}	a_4^{0}	a_4^{2}	a_4^{4}	a_5^{-5}	a_5^{-3}	a_5^{-1}	a_5^{1}
	-0.056	-0.027	-0.254	0.005	-0.051	0.003	-0.037	0.085	-0.046
	a_5^{3}	a_5^{5}	a_6^{-4}	a_6^{-2}	a_6^{0}	a_6^{2}	a_6^{4}	a_7^{-3}	a_7^{-1}
	-0.018	0.083	-0.104	-0.142	-0.149	0.154	-0.043	-0.141	-0.110
	a_7^{1}	a_7^{3}	a_8^{-2}	a_8^{0}	a_8^{2}	a_9^{-1}	a_9^{1}	a_{10}^{0}	
	-0.053	-0.003	0.302	-0.216	-0.032	0.174	-0.144	-0.144	

Table E.3: Coefficients used in LEICA experiments, rounded off to 3 significant digits - cont'd

Code	Coefficients								
365_03	a_1^{-1}	a_1^1	a_2^{-2}	a_2^0	a_2^2	a_3^{-3}	a_3^{-1}	a_3^1	a_3^3
	-0.005	-0.005	0.055	-0.002	-0.020	0.045	-0.024	-0.066	-0.005
	a_4^{-4}	a_4^{-2}	a_4^0	a_4^2	a_4^4	a_5^{-5}	a_5^{-3}	a_5^1	a_5^3
	0.004	0.009	-0.036	-0.014	0.010	0.010	-0.001	-0.007	-0.020
	a_5^5	a_6^{-4}	a_6^{-2}	a_6^0	a_6^2	a_6^4	a_7^{-3}	a_7^{-1}	a_7^1
	0.012	-0.005	-0.031	-0.030	0.020	0.004	-0.014	-0.027	0.013
	a_7^3	a_8^{-2}	a_8^0	a_8^2	a_9^{-1}	a_9^1	a_{10}^0		
	-0.012	0.035	0.003	-0.023	-0.003	0.003	-0.009		
365_06	a_1^{-1}	a_1^1	a_2^{-2}	a_2^0	a_2^2	a_3^{-3}	a_3^{-1}	a_3^1	a_3^3
	-0.010	-0.010	0.110	-0.004	-0.040	0.090	-0.048	-0.132	-0.010
	a_4^{-4}	a_4^{-2}	a_4^0	a_4^2	a_4^4	a_5^{-5}	a_5^{-3}	a_5^1	a_5^3
	0.008	0.018	-0.072	-0.027	0.020	0.019	-0.002	-0.014	-0.041
	a_5^5	a_6^{-4}	a_6^{-2}	a_6^0	a_6^2	a_6^4	a_7^{-3}	a_7^{-1}	a_7^1
	0.024	-0.010	-0.063	-0.060	0.039	0.008	-0.027	-0.054	0.027
	a_7^3	a_8^{-2}	a_8^0	a_8^2	a_9^{-1}	a_9^1	a_{10}^0		
	-0.023	0.071	0.005	-0.046	-0.005	0.006	-0.018		
365_11	a_1^{-1}	a_1^1	a_2^{-2}	a_2^0	a_2^2	a_3^{-3}	a_3^{-1}	a_3^1	a_3^3
	-0.021	-0.020	0.219	-0.008	-0.080	0.180	-0.097	-0.265	-0.019
	a_4^{-4}	a_4^{-2}	a_4^0	a_4^2	a_4^4	a_5^{-5}	a_5^{-3}	a_5^1	a_5^3
	0.015	0.036	-0.143	-0.054	0.040	0.038	-0.003	-0.028	-0.082
	a_5^5	a_6^{-4}	a_6^{-2}	a_6^0	a_6^2	a_6^4	a_7^{-3}	a_7^{-1}	a_7^1
	0.048	-0.021	-0.126	-0.121	0.078	0.017	-0.054	-0.107	0.054
	a_7^3	a_8^{-2}	a_8^0	a_8^2	a_9^{-1}	a_9^1	a_{10}^0		
	-0.046	0.142	0.010	-0.093	-0.010	0.012	-0.035		
365_22	a_1^{-1}	a_1^1	a_2^{-2}	a_2^0	a_2^2	a_3^{-3}	a_3^{-1}	a_3^1	a_3^3
	-0.042	-0.040	0.438	-0.016	-0.160	0.360	-0.194	-0.530	-0.038
	a_4^{-4}	a_4^{-2}	a_4^0	a_4^2	a_4^4	a_5^{-5}	a_5^{-3}	a_5^1	a_5^3
	0.030	0.072	-0.286	-0.109	0.080	0.077	-0.006	-0.056	-0.163
	a_5^5	a_6^{-4}	a_6^{-2}	a_6^0	a_6^2	a_6^4	a_7^{-3}	a_7^{-1}	a_7^1
	0.096	-0.042	-0.251	-0.242	0.157	0.034	-0.109	-0.214	0.107
	a_7^3	a_8^{-2}	a_8^0	a_8^2	a_9^{-1}	a_9^1	a_{10}^0		
	-0.093	0.283	0.021	-0.186	-0.021	0.024	-0.070		

Table E.4: Coefficients used in the random surface experiments, rounded off to 3 significant digits

Code	Coefficients							
`low`	a_1^{-1}	a_1^{1}	a_2^{-2}	a_2^{0}	a_2^{2}	a_3^{-3}	a_3^{-1}	a_3^{1}	a_3^{3}
	0.152	-0.243	1.759	0.234	0.677	-1.400	-0.473	-0.160	0.623
	a_4^{-4}	a_4^{-2}	a_4^{0}	a_4^{2}	a_4^{4}	a_5^{-5}	a_5^{-3}	a_5^{-1}	a_5^{1}
	0.083	-0.275	0.111	0.274	1.008	0.114	0.554	0.269	0.010
	a_5^{3}	a_5^{5}	a_6^{-6}	a_6^{-4}	a_6^{-2}	a_6^{0}	a_6^{2}	a_6^{4}	a_6^{6}
	-0.163	0.032	-0.060	-0.028	0.018	-0.091	-0.166	-0.232	0.095
	a_7^{-7}	a_7^{-5}	a_7^{-3}	a_7^{-1}	a_7^{1}	a_7^{3}	a_7^{5}	a_7^{7}	a_8^{-8}
	0.046	-0.035	-0.113	-0.067	0.033	0.040	-0.015	-0.050	-0.004
	a_8^{-6}	a_8^{-4}	a_8^{-2}	a_8^{0}	a_8^{2}	a_8^{4}	a_8^{6}	a_8^{8}	a_9^{-9}
	0.013	-0.004	0.002	0.020	0.038	0.023	-0.016	-0.009	0.013
	a_9^{-7}	a_9^{-5}	a_9^{-3}	a_9^{-1}	a_9^{1}	a_9^{3}	a_9^{5}	a_9^{7}	a_9^{9}
	-0.007	0.005	0.016	0.010	-0.012	-0.007	0.001	0.006	0.006
	a_{10}^{-10}	a_{10}^{-8}	a_{10}^{-6}	a_{10}^{-4}	a_{10}^{-2}	a_{10}^{0}	a_{10}^{2}	a_{10}^{4}	a_{10}^{6}
	0.000	0.001	-0.001	0.002	-0.001	-0.004	-0.006	-0.001	0.001
	a_{10}^{8}	a_{10}^{10}							
	-0.001	-0.001							
`medium`	a_1^{-1}	a_1^{1}	a_2^{-2}	a_2^{0}	a_2^{2}	a_3^{-3}	a_3^{-1}	a_3^{1}	a_3^{3}
	-1.043	-0.111	-0.286	-0.822	-0.032	0.042	0.133	0.290	-0.646
	a_4^{-4}	a_4^{-2}	a_4^{0}	a_4^{2}	a_4^{4}	a_5^{-5}	a_5^{-3}	a_5^{-1}	a_5^{1}
	-0.596	-0.426	0.594	0.386	-0.070	0.372	-0.380	0.435	-0.158
	a_5^{3}	a_5^{5}	a_6^{-6}	a_6^{-4}	a_6^{-2}	a_6^{0}	a_6^{2}	a_6^{4}	a_6^{6}
	-0.064	0.133	0.238	-0.318	0.237	-0.165	-0.134	-0.022	0.272
	a_7^{-7}	a_7^{-5}	a_7^{-3}	a_7^{-1}	a_7^{1}	a_7^{3}	a_7^{5}	a_7^{7}	a_8^{-8}
	-0.115	-0.306	0.145	0.288	-0.133	-0.043	-0.293	-0.346	0.423
	a_8^{-6}	a_8^{-4}	a_8^{-2}	a_8^{0}	a_8^{2}	a_8^{4}	a_8^{6}	a_8^{8}	a_9^{-9}
	-0.163	0.567	-0.022	0.086	0.017	0.120	-0.451	0.272	-0.036
	a_9^{-7}	a_9^{-5}	a_9^{-3}	a_9^{-1}	a_9^{1}	a_9^{3}	a_9^{5}	a_9^{7}	a_9^{9}
	0.048	0.211	-0.002	-0.521	0.054	0.069	0.190	0.152	0.105
	a_{10}^{-10}	a_{10}^{-8}	a_{10}^{-6}	a_{10}^{-4}	a_{10}^{-2}	a_{10}^{0}	a_{10}^{2}	a_{10}^{4}	a_{10}^{6}
	0.229	-0.146	0.013	-0.252	-0.000	-0.068	-0.019	-0.087	0.258
	a_{10}^{8}	a_{10}^{10}							
	-0.099	0.019							

Table E.5: Coefficients used in the random surface experiments, rounded off to 3 significant digits - cont'd

Code	Coefficients								
`high`	a_1^{-1}	a_1^1	a_2^{-2}	a_2^0	a_2^2	a_3^{-3}	a_3^{-1}	a_3^1	a_3^3
	0.048	-0.113	0.088	-0.423	-0.200	-0.263	-0.345	-0.176	0.006
	a_4^{-4}	a_4^{-2}	a_4^0	a_4^2	a_4^4	a_5^{-5}	a_5^{-3}	a_5^{-1}	a_5^1
	-0.099	-0.326	0.058	-0.495	0.231	0.273	0.229	0.075	0.249
	a_5^3	a_5^5	a_6^{-6}	a_6^{-4}	a_6^{-2}	a_6^0	a_6^2	a_6^4	a_6^6
	-0.014	0.095	0.292	-0.090	-0.030	0.114	0.365	-0.765	-0.158
	a_7^{-7}	a_7^{-5}	a_7^{-3}	a_7^{-1}	a_7^1	a_7^3	a_7^5	a_7^7	a_8^{-8}
	-0.218	-0.180	-0.220	0.014	0.410	0.070	0.280	0.018	0.117
	a_8^{-6}	a_8^{-4}	a_8^{-2}	a_8^0	a_8^2	a_8^4	a_8^6	a_8^8	a_9^{-9}
	-0.226	0.248	0.060	-0.067	-0.233	0.323	-0.119	0.019	-0.140
	a_9^{-7}	a_9^{-5}	a_9^{-3}	a_9^{-1}	a_9^1	a_9^3	a_9^5	a_9^7	a_9^9
	0.380	-0.065	0.319	0.173	-0.430	-0.049	-0.132	-0.008	-0.084
	a_{10}^{-10}	a_{10}^{-8}	a_{10}^{-6}	a_{10}^{-4}	a_{10}^{-2}	a_{10}^0	a_{10}^2	a_{10}^4	a_{10}^6
	0.022	-0.003	0.064	-0.198	0.075	0.008	0.252	0.115	0.107
	a_{10}^8	a_{10}^{10}							
	-0.005	0.121							
`extreme`	a_1^{-1}	a_1^1	a_2^{-2}	a_2^0	a_2^2	a_3^{-3}	a_3^{-1}	a_3^1	a_3^3
	-0.044	-0.362	-0.074	-0.057	-0.059	-0.066	0.605	-0.085	0.194
	a_4^{-4}	a_4^{-2}	a_4^0	a_4^2	a_4^4	a_5^{-5}	a_5^{-3}	a_5^{-1}	a_5^1
	-0.125	-0.174	-0.131	0.108	-0.507	0.254	-0.211	-0.218	0.668
	a_5^3	a_5^5	a_6^{-6}	a_6^{-4}	a_6^{-2}	a_6^0	a_6^2	a_6^4	a_6^6
	0.188	-0.089	-0.252	0.401	0.097	-0.388	-0.328	0.356	-0.326
	a_7^{-7}	a_7^{-5}	a_7^{-3}	a_7^{-1}	a_7^1	a_7^3	a_7^5	a_7^7	a_8^{-8}
	-0.590	0.042	-0.088	-0.246	-0.148	-0.533	-0.244	0.081	-0.362
	a_8^{-6}	a_8^{-4}	a_8^{-2}	a_8^0	a_8^2	a_8^4	a_8^6	a_8^8	a_9^{-9}
	-0.186	-0.315	0.084	0.361	0.088	0.074	-0.100	0.205	0.447
	a_9^{-7}	a_9^{-5}	a_9^{-3}	a_9^{-1}	a_9^1	a_9^3	a_9^5	a_9^7	a_9^9
	0.417	-0.143	0.106	0.223	-0.104	0.397	-0.056	0.008	-0.075
	a_{10}^{-10}	a_{10}^{-8}	a_{10}^{-6}	a_{10}^{-4}	a_{10}^{-2}	a_{10}^0	a_{10}^2	a_{10}^4	a_{10}^6
	0.039	0.324	0.233	0.032	-0.074	-0.017	0.086	-0.090	0.051
	a_{10}^8	a_{10}^{10}							
	-0.110	0.148							